Radiolarian biostratigraphy of Late Cretaceous pelagic sediments in the Oman Ophiolite: Environmental change based on the radiolarian faunal transition across the Cenomanian/Turonian boundary

（オマーンオフィオライトにおける後期白亜紀遠洋性堆積物の放散虫生層序:
放散虫群集変遷に基づく Cenomanian/Turonian 境界の環境変化）

Kousuke Hara

Doctoral Program in Environmental Science and Technology
Graduate School of Science and Technology
Niigata University

CONTENTS

Abstract

Lithostratigraphy and radiolarian biostratigraphy of Late Cretaceous pelagic sediments on basaltic extrusive rocks within the Oman Ophiolite were investigated in order to understand the nature of pelagic sedimentation, history of volcanic activity of the ophiolite, and radiolarian faunal transition and environmental change in this time period.

Pelagic and metalliferous sediments commonly occur on lavas and at the boundaries between different volcanic units. The basaltic rocks have been subdivided into three volcanic units: the V1 lava with the N-MORB signature, the V2 lava formed by intra-oceanic volcanism, and the V3 lava generated by intra-plate seamount magmatism (Ernewein et al., 1998). The most thickly accumulated sediments, which rest directly on the V1 lava formed by ridge magmatism, were named the Suhaylah Formation (Fleet and Robertson, 1980). The metalliferous and pelagic sediments of this formation are subdivided into four lithologies in stratigraphic ascending order: metalliferous sediments, red mudstone with chert intercalations, micritic limestone, and red mudstone. The Suhaylah Formation is overlain by the Zabyat Formation (Robertson and Woodcock, 1983). This formation consists of ophiolite debris, redeposited sandstone- to siltstone-sized volcaniclastic rocks, and pelagic red mudstone.

From the biohorizons of radiolarians, four radiolarian zones were defined. The *Guttacapsa gutta* Zone, obtained from metalliferous sediments and chert intercalations within red mudstone, could be correlated with the middle to lateset Cenomanian. The *Rhopalosyringium scissum* Zone, recovered from red mudstone and chert, is assigned to the lateset Cenomanian to early Turonian. The *Foremanina schona* Zone, recognized in micritic limestone, is correlated with the middle Turonian. The *Eostichomitra perapedhia* Zone, recovered from red mudstone of the uppermost part of the Suhaylah Formation and the top of the Zabyat Formation, is assigned to the late Turonian to Coniacian. The radiolarian age of the sediments overlying the V1 lava (middle–late Cenomanian: 96.5–93.9 Ma) is consistent with the high-precision U–Pb zircon age of crustal rocks formed by ridge magmatism (96.12–95.50 Ma: Rioux et al., 2016). In addition, the sediments on the V2 lava can be also correlated with the middle–late Cenomanian. These findings

reveal that the change of the tectonic setting from mid-ocean ridge through subduction zone to oceanic thrusting occurred in a short period and the activities of the V1 to V2 lavas were terminated in late Cenomanian.

Based on the discrimination diagrams by Murray (1994), the rocks of the Suhaylah and Zabyat formations ranges from the ridge to pelagic environments. In particular, metalliferous sediments and chert intercalation plot within the ridge field, whereas the other sediments plots within the pelagic field. These findings suggest that the Suhaylah and Zabyat formations were deposited in the pelagic environment and were not influenced by inputs of terrigenous materials.

Examination of radiolarian faunal composition shows that spherical Nassellaria such as the genera *Hemicryptocapsa* and *Holocryptocanium* increased dramatically in the OAE2 interval below the C/T boundary of the Suhaylah Formation. These features are also recognized in the European OAE2 horizons in which black shale was deposited (Bak, 2011). Therefore, the causes of extinction of the European Tethys and the Tethys of Oman are considered to be same, as follows: (1) the formation of LIPs (such as the Caribbean LIP) released CO_2, CH_4, and other greenhouse gases into the atmosphere, and then the temperature rose, (2) continental weathering was promoted, and a large amount of nutrient flowed into the ocean, (3) excessively supplied CO_2 was absorbed by the ocean, and subsequent ocean acidification drastically damaged the primary producer, especially in calcareous nannoplankton (Du Vivier et al., 2015), (4) after that, cyanobacteria and dinoflagellates increased explosively on the ocean surface where nutrients were abundantly present (Ohkouchi, 2003; Ando et al., 2017), and (5) extinction of radiolarians occurred by gradually enlarging of the oxygen minimum zone mainly in the ocean middle layer due to excess supply of organic matter without decomposition (such as cyanobacteria and dinoflagellate remains).

After the extinction of Cenomanian radiolarians, the *Rhopalosyringium* species occurs abundantly in the Suhaylah Formation, and their remarkable diversification can be recognized. On the other hand, this trend is not recognized in Europe. From this, it is considered that the radiolarian ecosystem was recovered quickly from environmental degradation in the Tethys of Oman that was open ocean, rather than closed European Tethys.

List of Tables

List of Figures

1. Introduction

Cretaceous is known as one of the most global warming era in Earth history (e.g. Jenkyns et al., 1994; Huber et al., 1995; Wilson et al., 2002). The reasons of global warming are considered to be that the super plume became active, the production rate of the plate increased, and large-scale magmatic activities represented by the formation of the large igneous province (s) (Larson, 1991; Coffn and Eldholm, 1994) released a large amount of greenhouse gases such as carbon dioxide (Larson and Erba, 1999; Svensen et al., 2004; Kuroda et al., 2007). In addition, the increase of the plate production rate made by a much larger volume of the mid-ocean ridge and oceanic plateau caused the sea level rise (Miller et al., 2005) along with the melting of the polar ice sheets (Moriya et al., 2007). Under such circumstances, the Oman Ophiolite was formed in the Tethys Sea.

The Oman Ophiolite (or Semail Ophiolite) is part of the long chain of Tethyan ophiolites that extends from the western Mediterranean to Southeast Asia. This ophiolite, observable along the east coast of Oman and the United Arab Emirates, forms a huge thrust sheet that crops out for a length of 500 km and a width of approximately 80 km in the Oman Mountains. Many studies have been conducted to understand the genesis and emplacement process of this ancient oceanic lithosphere using systematic mapping, detailed petrological and geochemical analyses, and structural geology (e.g., Reinhardt, 1969; Glennie et al., 1973, 1974; Pearce et al., 1981; Lippard et al., 1986; Nicolas, 1989). These studies demonstrated that the ophiolite is the most complete preserved section of upper mantle to oceanic crust worldwide. The sequence is more than 15 km thick and consists of mantle peridotites, layered gabbros, sheeted dikes, and extrusive lavas. Geochronological studies using U–Pb dating of zircons from gabbros, tonalites, and trondhjemites indicate that the ophiolitic crust formed during the late Cenomanian (ca. 96–95 Ma; Tilton et al., 1981; Warren et al., 2005;

Rioux et al., 2012, 2013, 2014, 2016).

The extrusive lavas in this ophiolite are geochemically diverse, including mid-ocean ridge basalt (MORB) or back-arc basin basalt (BABB), island-arc tholeiites, and calc-alkaline series lavas (e.g., Pearce et al., 1981; Alabaster et al., 1982; Ernewein et al., 1988; Umino et al., 1990; Ishikawa et al., 2002; Einaudi et al., 2003; Godard et al., 2003; A'Shaikh et al., 2005). Historically, these data have led to different interpretations of the tectonic setting of their formation. One hypothesis is that the ophiolite formed at a spreading axis above a subduction zone (e.g., Pearce et al., 1981; Alabaster et al., 1982); another is that it was generated at a mid-ocean ridge (e.g., Nicolas, 1989; Nicolas and Boudier, 2003). The presence of multiple generations of plutonism and volcanism within the mantle and crust has been also clearly demonstrated (e.g., Juteau et al., 1988; Adachi and Miyashita, 2003; Godard et al., 2006; Tamura and Arai, 2006; Goodenough et al., 2010). Although there is still no general agreement on the formation of ophiolites, an alternative proposal is the stepwise evolution of initial mid-ocean ridge magmatism and subsequent thrusting/subduction associated with primitive arc-like volcanism (e.g., Arai et al., 2006). This scenario is supported by recent volcano-stratigraphic and geochemical studies (e.g., Kusano et al., 2012, 2014). In addition, high-precision U–Pb dating of gabbros, tonalites, and trondhjemites reveal that ridge magmatism and arc-like magmatism occurred during ca. 96.0–95.5 Ma and 95.5–95.0 Ma, respectively (Rioux et al., 2012, 2013, 2014, 2016), indicating rapid development of thrusting/subduction following formation of the ophiolite crust.

For age determination of the eruption of basaltic rocks within ophiolites, the biostratigraphic age of metalliferous sediments (umbers) and pelagic sediments overlying extrusive lavas is important (e.g., Robertson and Hudson, 1974; Robertson, 1975; Blome and Irwin, 1985). Tippit et al. (1981) provided a preliminary report on radiolarians possibly ranging in age from the early Cenomanian to the Coniacian–Santonian from sediments exposed

around the Wadi Jizzi, northern Oman (Fig. 1). That study demonstrated the potential usefulness of radiolarians in constraining the timing of the termination of basaltic extrusive rocks; however, the work yielded limited information in terms of localities, sampling horizons, and the stratigraphic distribution and faunal composition of radiolarians, which are necessary for more accurate age determination. In addition, although the radiolarian chronology for the Late Cretaceous was greatly advanced in the 1980s and subsequently (e.g., O'Dogherty, 1994), there have been few applications of radiolarian dating to sediments overlying basaltic lavas.

In this study, we reexamined the stratigraphy, lithology, and radiolarian ages of metalliferous and pelagic sediments around the Wadi Jizzi, to clarify the nature of pelagic sedimentation and the history of volcanic activity of the ophiolite. We discovered abundant and diverse radiolarians from these sedimentary sequences across the middle to upper Cenomanian and Coniacian. The obtained faunal assemblages are suitable for comparison with concurrent assemblages of the west Tethys. We describe the lithostratigraphy and faunal characteristics, and discuss the age of the radiolarian-bearing rocks and the eruption age of the basaltic lava in the study area.

2. Geologic framework

2. 1. Geology and description of lithofacies

The extrusive lavas and overlying sedimentary sequence, consisting of metalliferous sediments, red mudstone with intercalated chert, and micritic limestone, are well exposed in the area about 40 km west of Sohar (Fig. 1), called the "Wadi Jizzi Zone" (Fleet and Robertson, 1980). Around this area, an almost complete oceanic crustal sequence is readily observable, which consists of harzburgites and dunites, layered gabbros, a sheeted-dike complex, and extrusive lavas (e.g., Lippard et al., 1986).

2. 2. Volcanic sequences

The extrusive lavas have been subdivided into five units: the Geotimes, Lasail, Ally, CPX-phyric, and Salahi units on the basis of geochemical composition (e.g., Alabaster et al., 1982; Lippard et al., 1986; Ernewein et al., 1988). Of these, the Geotimes Unit directly overlies the sheeted-dike complex with a gradational contact (Lippard et al., 1986). Ernewein et al. (1988) summarized the subdivision of volcanic rocks and recognized that V1 (Geotimes Unit), which has a normal MORB (N-MORB)-like signature, was erupted around a spreading ridge and that V2 (Alley and CPX-phyric units) formed by intra-oceanic arc volcanism. In addition, thick lava flows of V3 (Salahi Unit), ascribed to intra-plate volcanism (Lippard et al., 1986; Ernewein et al., 1988), were emplaced onto pelagic sediments (Umino, 2012). Recently, Kusano et al. (2012) reexamined the stratigraphy of the volcanic units at Wadi Fizh, about 25 km north of Wadi Jizzi, based on their geochemical composition and stratigraphic relationship. That study subdivided the V1 extrusive rocks into four units: the LV1a and LV1b (Lower V1 Sequence), MV1 (Middle V1 Sequence), and UV1 (Upper V1 Sequence). According to Kusano et al. (2012), the LV1a consists of lava flows that erupted on a ridge crest and filled an axial trough, whereas the LV1b is composed of pillow lavas and lobate sheet flows emplaced on a ridge flank. The MV1, which was emplaced off-axis, is composed of evolved flows transported from a ridge summit and less evolved flows that erupted in situ. The UV1 was erupted in situ from off-axial vents.

2. 3. Suhaylah Formation

Metalliferous and pelagic sediments commonly occur on lavas and at the boundaries between different volcanic units. The most thickly accumulated sediments (>15 m thick), which rest directly on the V1 lava (the 'lower' lava of the original description by Fleet and Robertson, 1980), were named the

Suhaylah Formation (Fleet and Robertson, 1980; Woodcock and Robertson, 1982). The type section is located northwest of a small village (Suhaylah) near the Wadi Jizzi River (Fig. 2). Typical metalliferous sediments are dark purple-colored ferromanganoan mudstone with amorphous Fe–Mn oxides. These metalliferous sediments change gradually to dark red-colored radiolarian mudstones with interbedded thin chert layers, which have higher silica and lower metal contents. The mudstone is conformably overlain by pelagic micritic limestone. Fleet and Robertson (1980) and Robertson and Fleet (1986) suggest that the metalliferous and pelagic sediments were accumulated on a horst-like topographic high by hydrothermal activity relatively far from a spreading center, and subsequent sedimentation of siliceous and calcareous ooze during gradual waning of the hydrothermal activity.

Glennie et al. (1974) reported a foraminifer (Rotalipora sp.) in lime-mudstone overlying pillow lava at Wadi Jizzi and assigned it to the Cenomanian. They also noted the occurrence of 'Globotruncana species', including 'Globotruncana sigali' and 'Globotruncana schneegansi', in radiolarian chert and silicified lime-mudstone interbedded with pillow lava at Wadi Ragmi (Rajimi), located ~50 km north of Wadi Jizzi, and indicated a Coniacian age for these rocks. Tippit et al. (1981) conducted radiolarian-based biostratigraphic dating of metalliferous and pelagic sediments overlying the Geotimes Unit (V1 lava) and the Alley Unit (V2 lava). Based on the radiolarian biostratigraphic scheme of the late 1970s, they concluded that the age of the lower metalliferous sediments covering the V1 lava is early Cenomanian, whereas that of the upper micritic limestone is Coniacian–Santonian. Schaaf and Thomas (1986) reported a radiolarian fauna from chert overlying the ophiolite at Wadi Ragmi and interpreted its age as early Campanian; however, there are many unclear points about the stratigraphic positions of sampling horizons and faunal details. Beurrier et al. (1987) reported occurrences of possible Albian to Campanian radiolarians

from sediments within the ophiolite over wide areas.

2. 4. Zabyat Formation

The Suhaylah Formation is overlain by the Zabyat Formation (Woodcock and Robertson, 1982; Robertson and Woodcock, 1983a) which consists of ophiolite debris, redeposited sandstone- to siltstone-sized volcaniclastic rocks, and pelagic mudstone. In the upper part of the ophiolite, the Batinah Complex (Woodcock and Robertson, 1982; Robertson and Woodcock, 1983b) widely overlies the extrusive lavas, the Suhaylah and Zabyat formations, and sometimes sheeted dikes with distinct erosional surfaces.

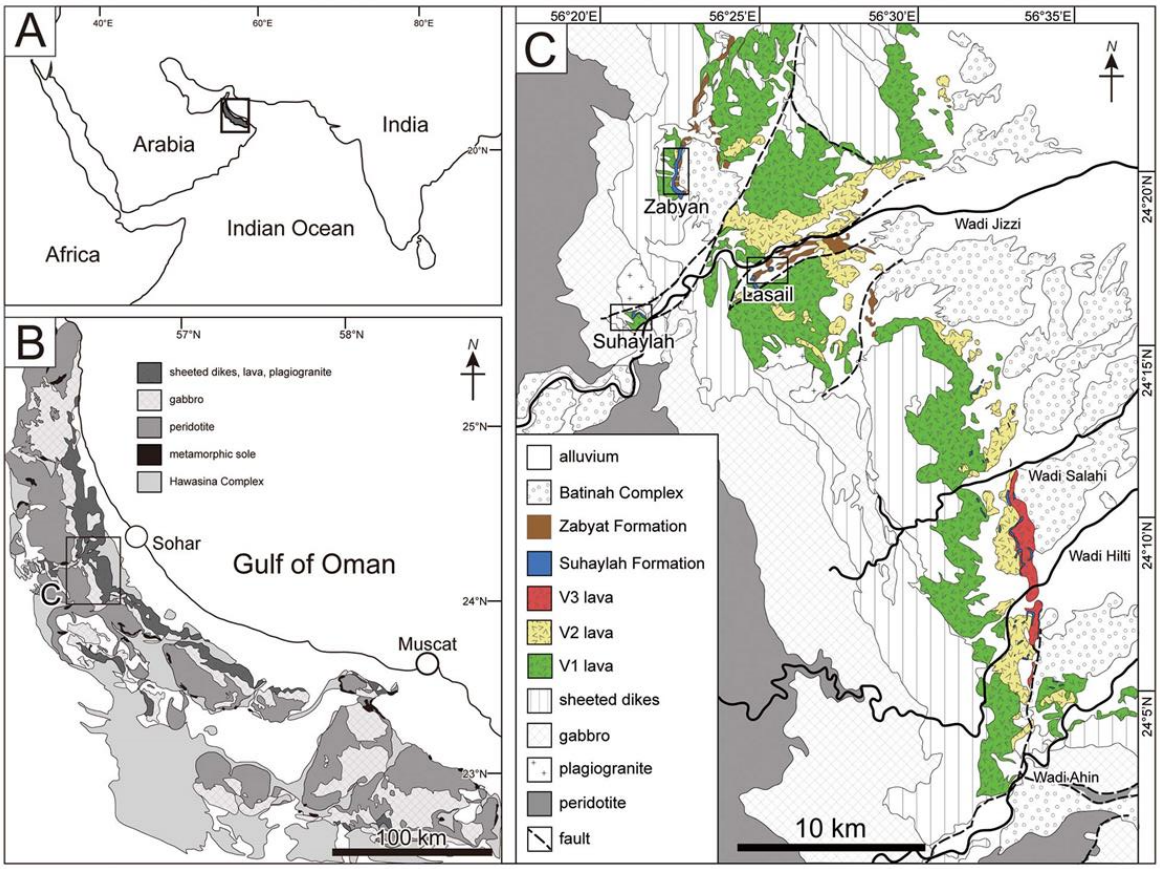

Fig. 1. Index map showing the location of the study area (Wadi Jizzi area) in northern Oman. (A) Location of the Oman Ophiolite. (B) Distribution of ophiolitic rocks in Oman (modified from Nicolas et al., 2009). (C) Simplified geological map of the area west of Sohar. The base map is modified from Bishimetal Exploration Co. Ltd. (1987).

3. Study sections and lithostratigraphy

3. 1. Study sections

We conducted radiolarian biostratigraphic studies of the metalliferous and pelagic sediments of the Suhaylah and Zabyat formations at three stratigraphic sections. Figures 2 to 4 show the detailed distribution of the rocks of these formations at study sections (Suhaylah, Zabyan, and Lasail exposures). We distinguished two types of lithostratigraphic successions; the one is deposited on the V1 lava (Suhaylah exposure), and another are accumulated on the V2 lava (Zabyan and Lasail exposures).

3. 2. Sediments on the V1 lava (Suhaylah exposure)

The Suhaylah exposure is the type locality of the Suhaylah Formation (Fleet and Robertson, 1980; Woodcock and Robertson, 1982). Figure 2 shows the locations of study sections (sections 846, 059-2, 057, and 849). Tippit et al. (1981) reported radiolarians from a locality in the mapped area; however, the precise location of the analyzed section was not stated in their article. In the uppermost part of the Suhaylah Formation in the study area, red mudstone is interbedded with thin redeposited volcanic sandstone layers and gradually changes upward into conglomerate of the Zabyat Formation, indicating a conformable relationship between the Suhaylah and Zabyat formations.

The basaltic lavas that directly underlie the sediments at the Suhaylah exposure are widely distributed in the study area. The lava is gray to greenish gray in color, and where altered is green in color. Sheet lava dominates overall, and pillow lava is also seen locally. The basaltic lava of this area directly overlies sheeted dikes. All previous studies divided the basaltic lava of this area into the 'lower' lava, the Geotimes Unit, and the V1 sequence (Fleet and Robertson, 1980; Tippit et al., 1981; Robertson and Fleet, 1986; Bishimetal Exploration Co. Ltd., 1987; Kusano et al., 2014). The

chemistry of the basaltic rocks that underlie the metalliferous sediments of the section analyzed herein allows classification of the rock as the Lower V1 Sequence of Kusano et al. (2012; Y. Kusano, pers. comm. in 2014).

The sediments of the Suhaylah Formation in the Suhaylah exposure, which have a maximum thickness of 22.5 m, are continuously exposed in four of the examined sections (sections 846, 059-2, 057, 849) and are subdivided into four lithologic units (units SS1, SS2, SS3, and SS4, in ascending stratigraphic order; Fig. 3). Unit SS1 is composed mainly of metalliferous sediments, Unit SS2 of red mudstone intercalated with chert, Unit SS3 of micritic limestone, and Unit SS4 of red mudstone. A similar stratigraphy is observable in sections 782, 845, 847, and 059-1, but the thickness of each unit in these sections varies markedly and the strata are partly covered by talus deposits.

The fine-grained pelagic sediments and coarse-grained ophiolite debris of the Zabyat Formation in the Suhaylah exposure are subdivided into units SZ1 and SZ2 (Fig. 3).

3. 2. 1. Unit SS1 (Suhaylah Formation)

Unit SS1 consists mainly of metalliferous sediments interbedded with thin chert layers (Fig. 4). The thickness of the unit ranges from 3 to 15 m. The basal portion that is in contact with the basaltic lava is characterized by a thin layer of reddish metalliferous sediment. According to Robertson and Fleet (1986), this sediment shows high SiO2 values and is enriched in Fe2O3 rather than MnO. Above the basal layer, the sediments are very fine-grained and are commonly dark purple to dark red in color with a metallic luster. The sediments are enriched in Fe2O3 and MnO (Robertson and Fleet, 1986). Thin laminations within weakly stratified beds are commonly observed. The metallic luster is distinctive in the lower part and becomes less pronounced toward the upper part. In the lower part of this unit, hydrothermal cherts occur as thin interbeds (~20 cm thick) or nodular-shaped lenses within the

metalliferous sediments. Although these cherts contain rare radiolarian shells, the chert layers yield moderately preserved radiolarians at section 846. The sediments in the upper part of this unit become more argillaceous and yield well-preserved radiolarians in section 846.

3. 2. 2. Unit SS2 (Suhaylah Formation)

Unit SS2 is composed mainly of radiolarian-bearing mudstone intercalated with radiolarian chert (Fig. 4). This unit ranges in thickness from 2 to 7 m. The mudstone has a gradational contact with the metalliferous sediments of the underlying Unit SS1. The mudstone is red in color and very fine-grained, without terrigenous crystalline particles such as quartz and feldspar. Well-preserved radiolarian tests occur sparsely in the matrix of clay minerals with hematite, although the originally spherical shells are sometimes preserved as ovoidal and compaction-flattened forms. In all exposures, several radiolarian chert layers (5–10 cm thick) are intercalated with red mudstone. The chert contains numerous well-preserved radiolarian tests. The rhythmic alternations of red mudstone and radiolarian chert are also observable in the upper part of this unit.

3. 2. 3. Unit SS3 (Suhaylah Formation)

This unit consists mainly of micritic limestone (Fig. 4). The limestone changes gradually from the underlying red mudstone of Unit SS2 through a thin transitional layer of muddy siliceous micrite. The limestone is thinly bedded (3–5 cm thick) and red-purple in color in the lower part and greenish-gray in the upper part. The matrix is fine-grained carbonate and clay minerals. Numerous well-preserved radiolarian shells without calcification can be observed within the matrix. Radiolarian tests, 80–350 μm in size, make up 50%–80% by volume of the micritic limestone. The limestone of this unit is devoid of terrigenous crystalline particles and contains rare silicified foraminiferal remains. Several green radiolarian chert layers (5–15 cm thick)

are intercalated with the upper parts of sections 059-2 and 057. These layers contain abundant poorly preserved radiolarian tests.

3. 2. 4. Unit SS4 (Suhaylah Formation)

Unit SS4, about 4.5 m thick, consists mainly of red mudstone (Fig. 9). The mudstone is very fine-grained without terrigenous crystalline particles. Well-preserved radiolarian tests (but sometimes flattened) occur sparsely in the matrix. Although these characteristics are similar to red mudstone of Unit SS2, chert layers are not interbedded within Unit SS4.

3. 2. 5. Unit SZ1 (Zabyat Formation)

This unit consists mainly of red mudstone with intercalations of middle- to coarse-grained sandstone layers that are considered to be redeposited debris of basaltic rocks (Fig. 9). The thickness of this unit is 17 m. In the lower part of this unit, the red mudstone are intercalated with thin layers of siliceous mudstone and redeposited basaltic clastics. In the upper part, thick beds of redeposited basaltic clastics are commonly observed.

3. 2. 6. Unit SZ2 (Zabyat Formation)

This unit is composed of redeposited beds of basaltic debris and matrix-supported conglomerate. The conglomerate contains breccia of basaltic lava, metalliferous sediments, and chert. The breccia varies in size, ranging from several cm to 1 meter width. The matrix of this conglomerate is dark purple to black in color and consists of fine-grained redeposited basaltic clastics.

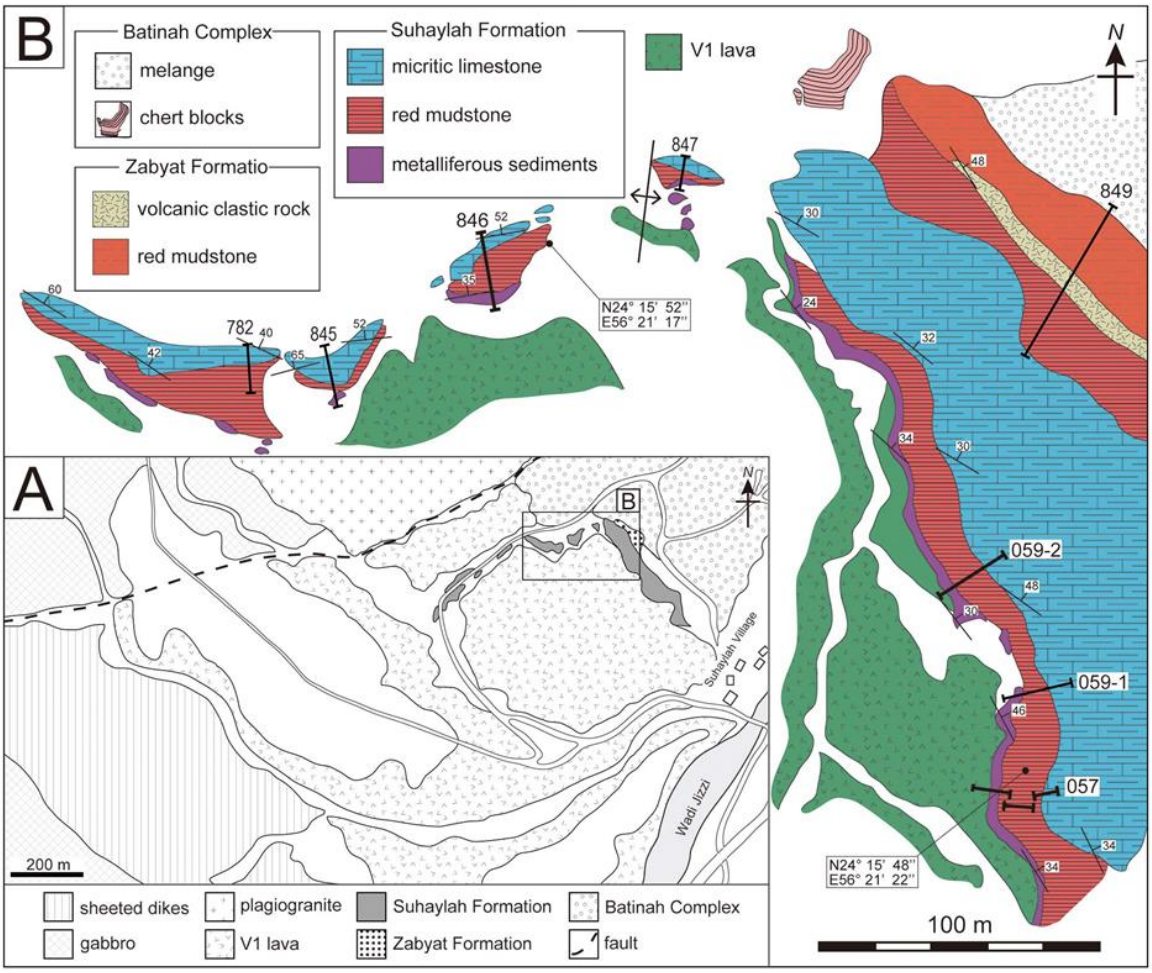

Fig. 2. Index map showing the locations of examined sections at the Suhaylah exposure. (A) Simplified geological map of the area northwest of Suhaylah Village. See Fig. 1 for the location of the mapped area. The base map is modified from Bishimetal Exploration Co. Ltd. (1987). (B) Geological map of the sampled area.

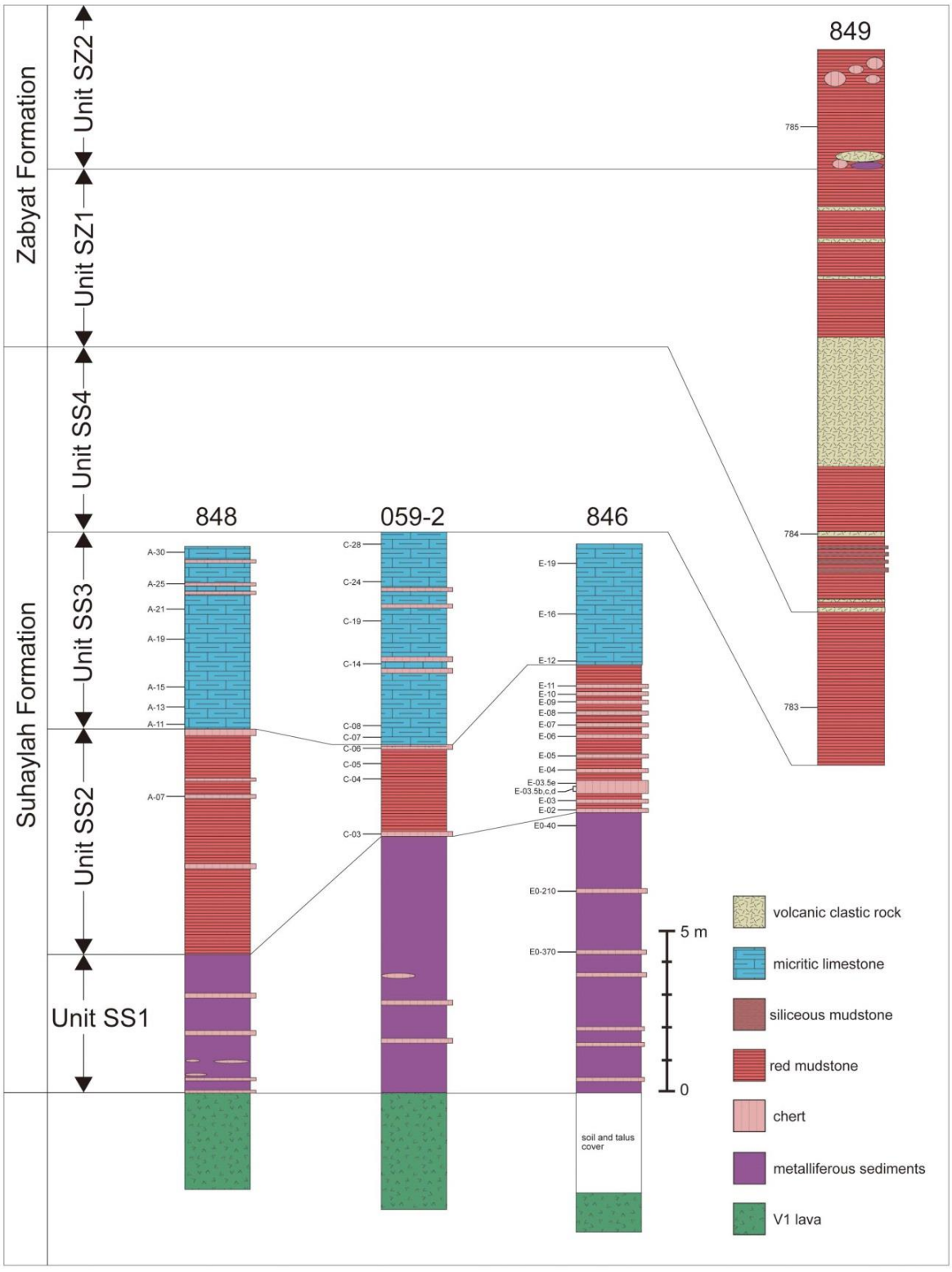

Fig. 3. Lithostratigraphic columns measured within the Suhaylah exposure and sampling layers. See Fig. 2 for the locations of sections details. Correlations indicated by solid lines are based on key lithostratigraphic boundaries.

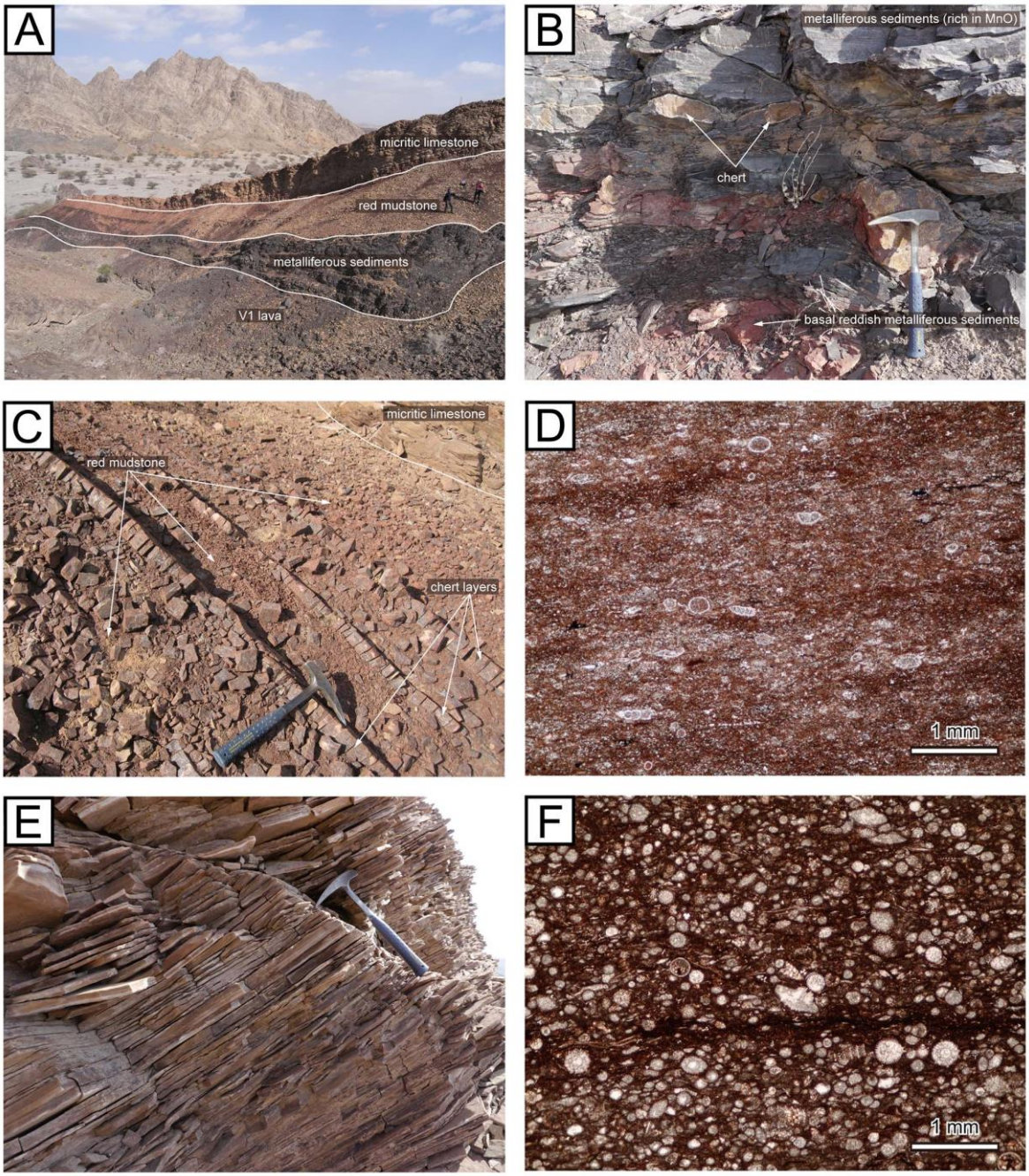

Fig. 4. Outcrop photographs and photomicrographs showing the lithologies of sediments in the Suhaylah exposure. (A) View of outcrops of the V1 lava and the Suhaylah Formation. (B) Metalliferous sediments and chert intercalations exposed at section 057. (C) Alternating beds of red mudstone and radiolarian chert exposed at section 846. (D) Photomicrograph of red mudstone exposed at section 059-2 (sample C-04) containing radiolarian skeletons. Plane-polarized light. (E) Micritic limestone exposed at section

057. (F) Photomicrograph of micritic limestone at section 059-2 (sample C-08) containing many radiolarian skeletons. Plane-polarized light.

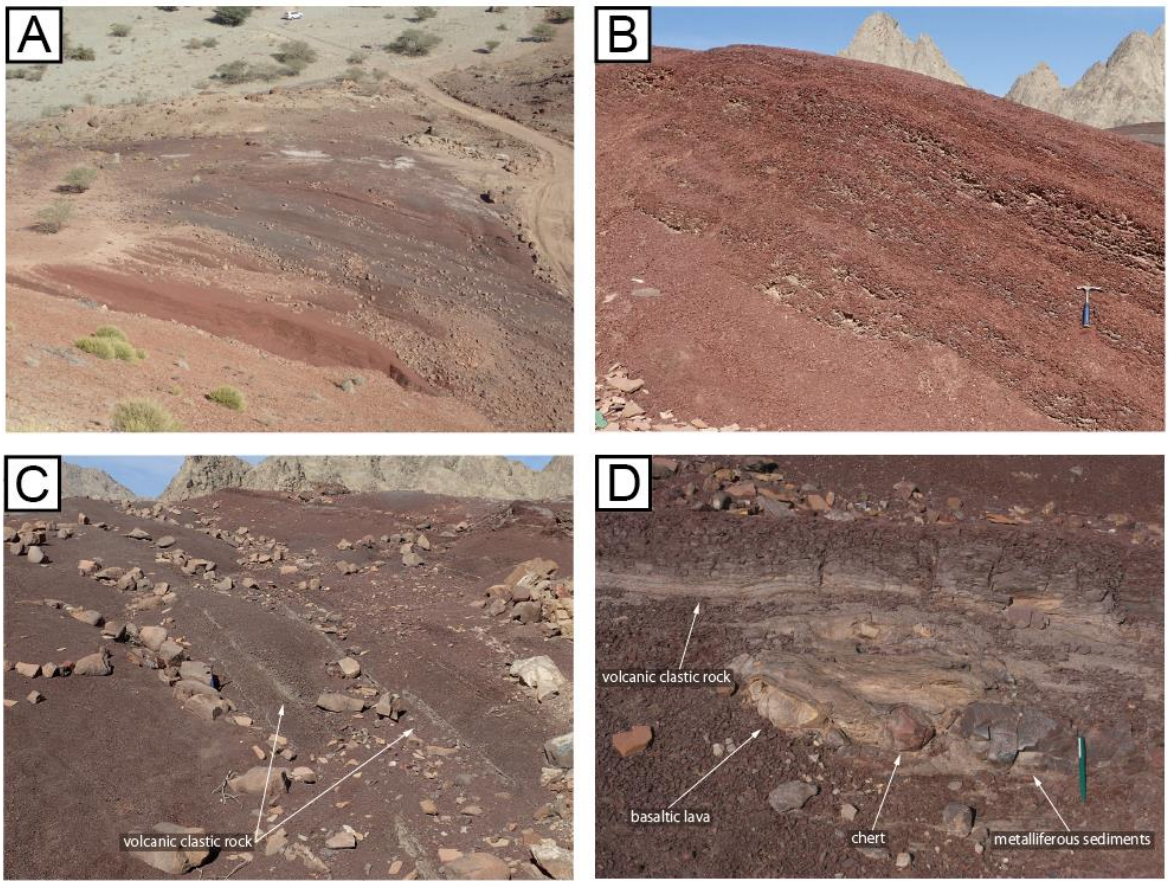

Fig. 5. Outcrop photographs showing the lithologies of sediments in the Suhaylah exposure. (A) View of outcrops of the Suhaylah and Zabyat formations. (B) Red mudstone (Unit SS4) exposed at section 849. (C) Red mudstone (Unit SZ1) and intercalations of redeposited clastics of volcanic rocks exposed at section 849. (D) Conglomerate containing basaltic lava and pelagic sediments (Unit LZ2) exposed at section 849.

3. 3. Sediments on the V2 lava (Zabyan and Lasail exposures)

Metalliferous and pelagic sediments overlying the V2 lava are observed in the Zabyan and Lasail exposures (Figs. 6, 10). The Zabyan exposure is located in northwest of a small village (Zabyan), which is near the type locality of the Zabyat Formation (Woodcock and Robertson, 1982). The basaltic lavas at this exposure have been classified into the 'upper' lava (Fleet and Robertson, 1980). Bishimetal Exploration Co. Ltd. (1987) subdivided the lavas in the southern part of this exposure into the 'lower' lava, and that in the northern part into the 'upper' lava. Based on the result of our geochemical analysis, the basaltic lavas that are directly covered by metalliferous and pelagic sediments can be classified into the V2 lava (Y. Kusano, pers. comm. in 2016).

In the Zabyan exposure, the Suhaylah Formation of the analyzed sections (sections 479, 480, and 482) consists of metalliferous and pelagic sediments (Fig. 7). The maximum thickness reaches 54 m. The sediments are subdivided into four lithologies (Fig. 7): metalliferous sediment interbedded with thin chert layers (Unit ZS1), red mudstone with chert intercalations (Unit ZS2), micritic limestone (Unit ZS3), and red mudstone (Unit ZS4). The Zabyat Formation, which can be observed in sections 482, consists of breccia of basaltic lava (Unit ZZ1).

The Lasail exposure is located in near the Lasail Mine, 30 km southwest of Sohar. The distribution of the Suhaylah and Zabyat Formations and the locations of study sections (sections 305 to 307, 465, 472) are shown in Fig. 6. The analyzed section (sections 305 to 307 and 472) consists of pelagic sediments of 34 m thick. Although basaltic lavas that directly underlie sediments are not exposed, the V2 lava occurs in the northern part of the area. In addition, the lithostratigraphy of metalliferous and pelagic sediments in the Lasail exposure (Fig. 11) is very similar to that in Zabyan exposure; namely, Unit ZS1 corresponds to Unit LS1, Unit ZS2 to LS2, and Unit ZS3 to LS3.

In the uppermost part of the Lasail exposure, the Suhaylah Formation is covered by the Zabyat Formation. The stratigraphy of the Zabyat Formation at the study area is subdivided into the following three lithologies (Fig. 11): conglomerate containing pebbles of peridotite (Unit LZ1), conglomerate containing pebbles of basaltic lava and pelagic sediments (Unit LZ2), and red mudstone intercalated with siliceous layers (Unit LZ3).

3. 3. 1. Units ZS1 and LS1 (Suhaylah Formation)

Units ZS1 and LS1 consists mainly of metalliferous sediments interbedded with thin chert layers and siliceous mudstone. The thicknesses of the units ZS1 and LS1 are 2–14 m and more than 6 m, respectively. Metalliferous sediments of these units are very fine-grained and are dark purple in color with a metallic luster, which are very similar to those of Unit SS1 in the Suhaylah exposure. Radiolarian chert and siliceous mudstone layers of 5–10 cm thick that contain well-preserved radiolarians are intercalated with the upper part of these units. In addition, orange-colored chert layers of ca. 10 cm thick that could be generated from hydrothermal activity are interbedded in metalliferous sediments. Highly altered mudstone being greenish grey, pale grey, white, and black in color are also observable.

3. 3. 2. Units ZS2 and LS2 (Suhaylah Formation)

Units ZS2 and LS2 are composed mainly of radiolarian-bearing mudstone intercalated with radiolarian chert. Units ZS2 and LS2 are 7–23 m and 13 m thick, respectively. The lithology of the mudstone is very similar to that of Unit SS1 in the Suhaylah exposure. However, there are more chert intercalations than those of Unit SS1, and the rhythmic alternations of red mudstone and radiolarian chert are thickly developed.

3. 3. 3. Units ZS3 and LS3 (Suhaylah Formation)

This unit consists of micritic limestone, which is gradually changed from

underlying red mudstone. The limestone is lithologically same as that of Unit SS3 in the Suhaylah exposure.

3. 3. 4. Unit ZS4 (Suhaylah Formation)

This unit, only recognized in the Zabyan exposure, is composed of red mudstone. The mudstone is very fine-grained without terrigenous crystalline particles and contains well-preserved radiolarians.

3. 3. 5. Unit LZ1 (Zabyat Formation)

This unit is characterized by conglomerate only containing pebbles to boulders of serpentinite (Fig. 9). We recognized this unit only in the Lasail exposure. The thickness of this unit is over 7 m. The serpentinite conglomerate is poorly sorted and partly brecciated.

3. 3. 6. Units ZZ1 and LZ2 (Zabyat Formation)

This unit consists of conglomerate containing pebbles to boulders of basaltic lava, chert, and micritic limestone (Fig. 9). This conglomerate is the most typical lithology of the Zabyat Formation. The conglomerate is matrix-supported and poorly sorted. The matrix is fine-grained redeposited basaltic clastics. The conglomerate of Unit ZZ1 in the Zabyan exposure dominates pebbles to boulders of basaltic lava. In contrast, Unit LZ1 in the Lasail exposure is characterized by the conglomerate that contains large amount of pebbles to boulders of micritic limestone and chert.

3. 3. 7. Unit LZ3 (Zabyat Formation)

This unit, recognized in the Lasail exposure, consists mainly of red mudstone associated with thin layers of siliceous red mudstone (Fig. 9). Red siliceous micrite occurs in the uppermost part of this unit. The red mudstone is well stratified in 3–15 cm thick and contains numerous radiolarian tests. The lithology of this mudstone is very similar to the red mudstone of units

SS4 and ZS4 that are the uppermost part of the Suhaylah Formation.

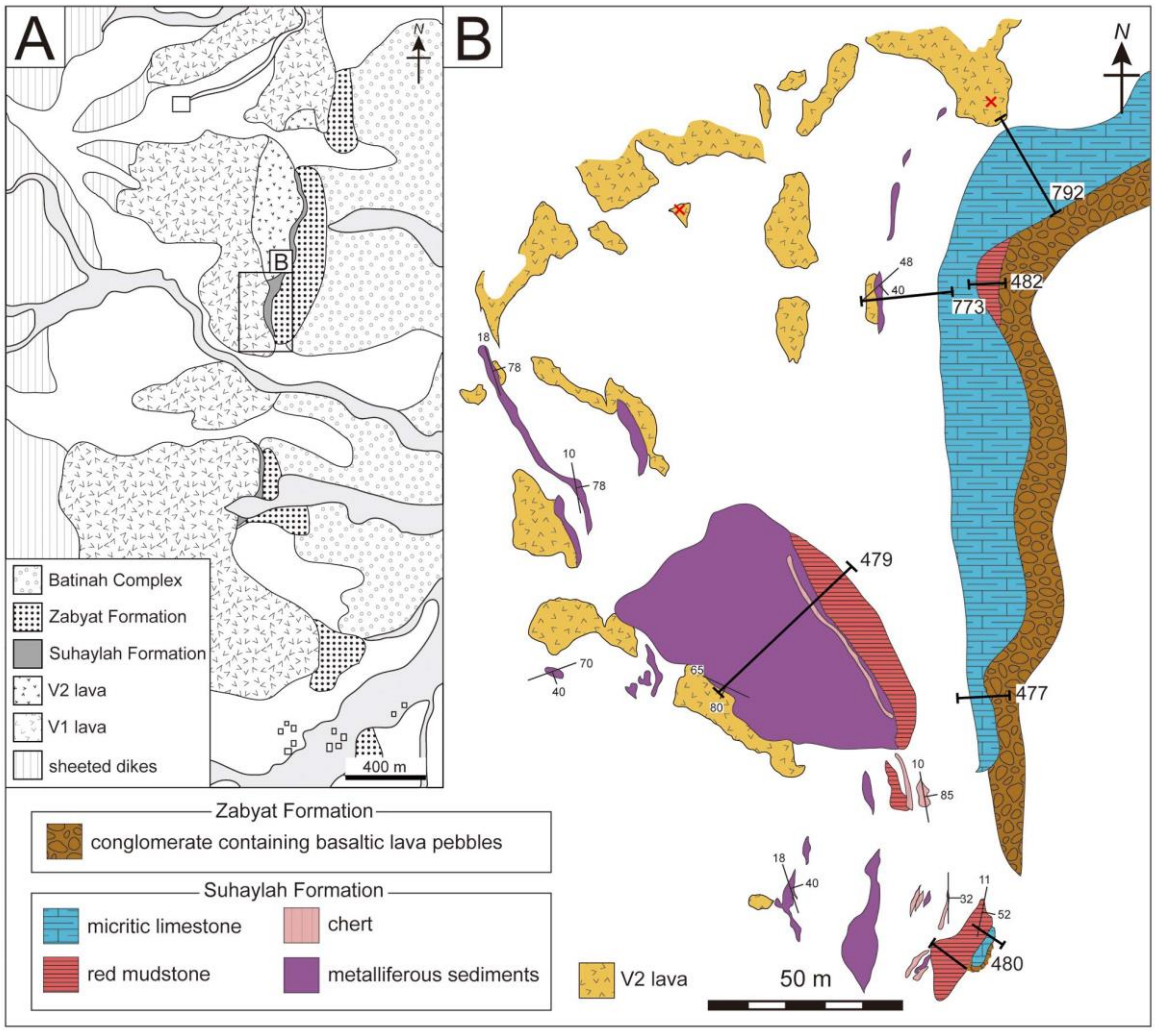

Fig. 6. Index map showing the locations of examined sections at the Zabyan exposure. (A) Simplified geological map of the area northwest of Zabyan Village. See Fig. 1 for the location of the mapped area. The base map is modified from Bishimetal Exploration Co. Ltd. (1987). (B) Geological map of the sampled area.

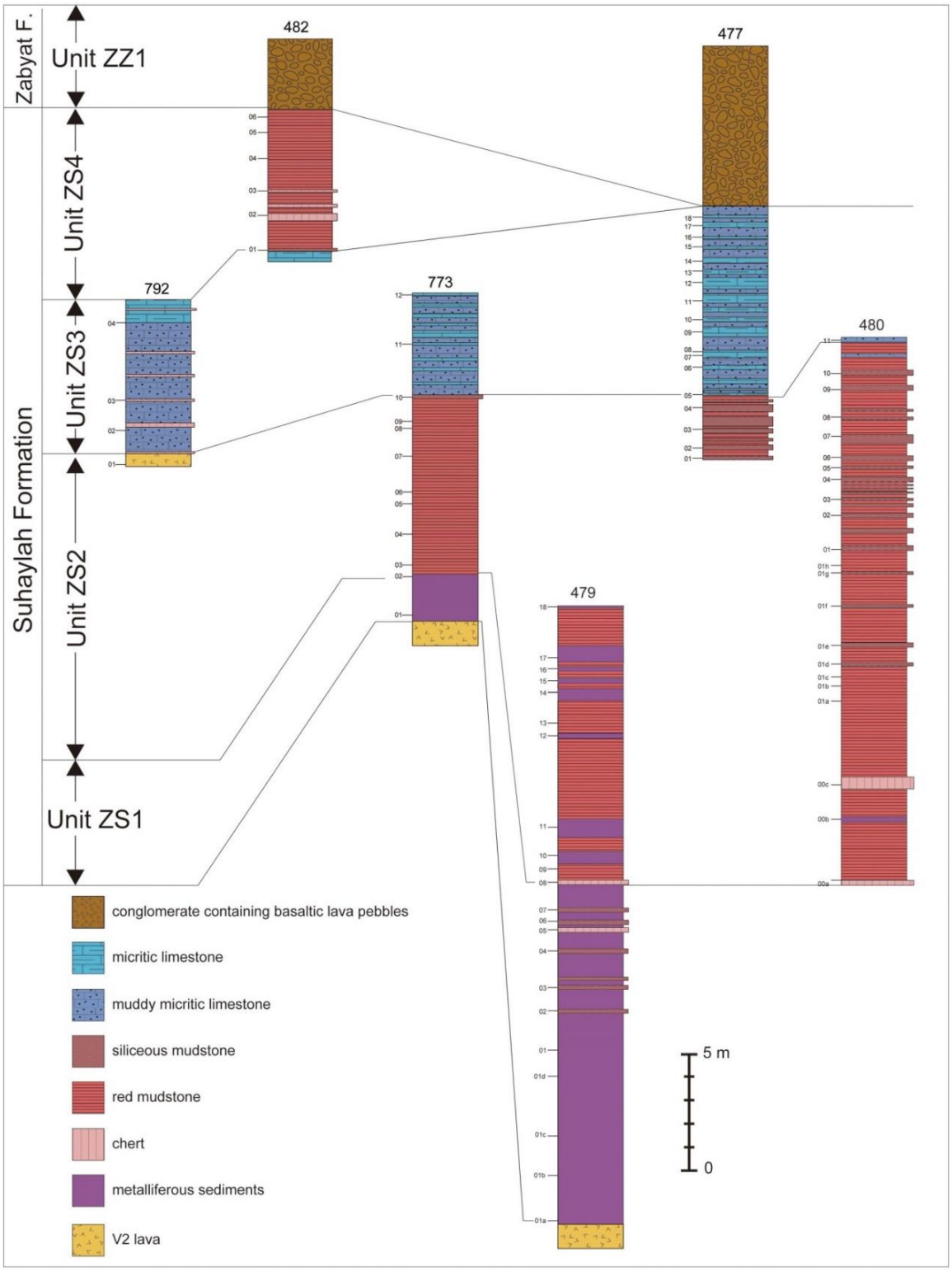

Fig. 7. Lithostratigraphic columns measured within the Zabyan exposure and sampling layers. See Fig. 3 for the locations of sections details. Correlations indicated by solid lines are based on key lithostratigraphic boundaries.

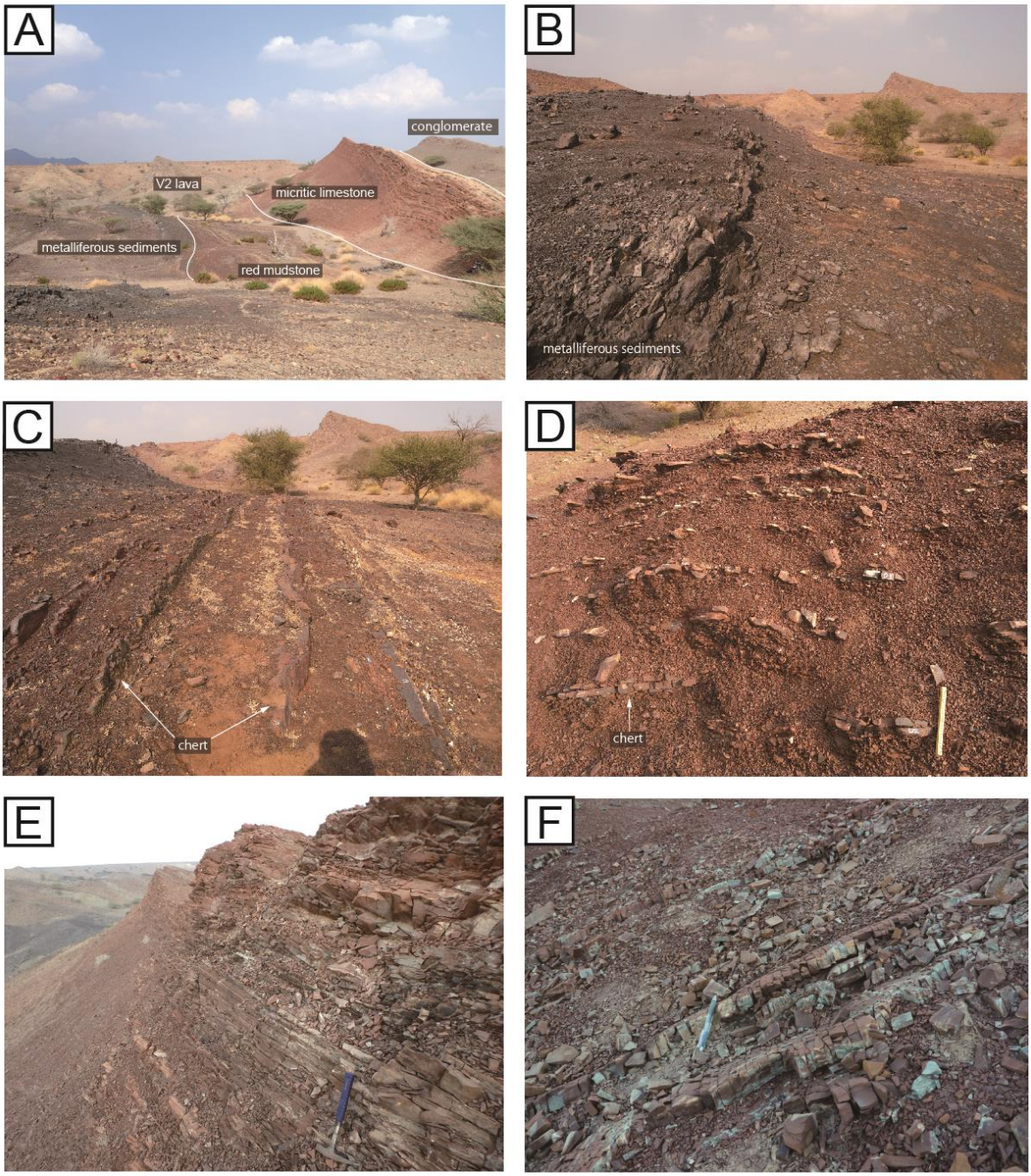

Fig. 8. Outcrop photographs showing the lithologies of sediments in the Zabyan exposure. (A) View of outcrops of the V2 lava, the Suhaylah Formation, and the Zabyat Formation. (B) Metalliferous sediments (Unit ZS1) exposed at section 479. (C) Metalliferous sediments (Unit ZS1) and intercalations of chert exposed at section 479. (D) Red mudstone (Unit ZS2) and intercalations of chert exposed at section 480. (E) Micritic limestone (Unit ZS3) exposed at section 773. (F) Red mudstone (Unit ZS4) exposed at section 482.

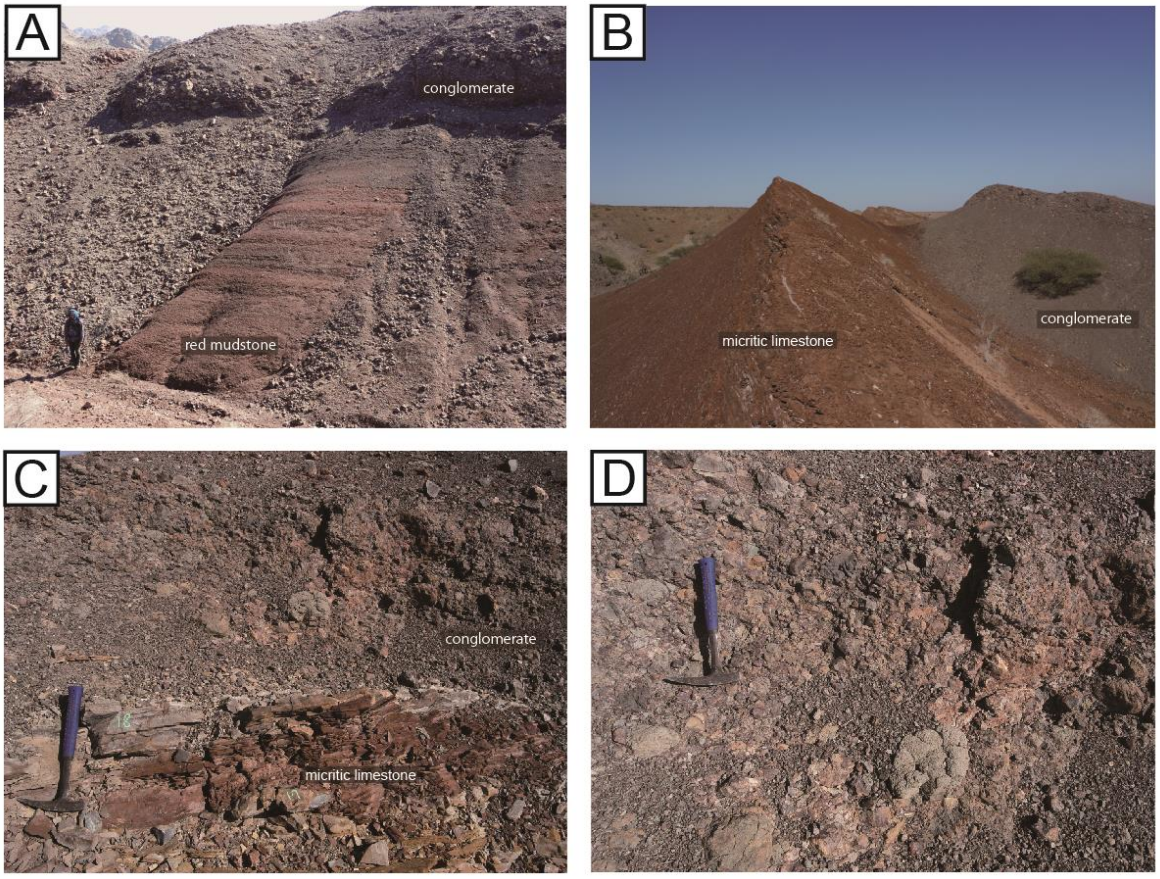

Fig. 9. Outcrop photographs showing the lithologies of sediments in the Zabyan exposure. (A) Red mudstone (Suhaylah Formation) and conglomerate (Zabyat Formation). (B) Micritic limestone (Suhaylah Formation) and conglomerate (Zabyat Formation). (C) Outcrop showing the contact relationship between micritic limestone and conglomerate exposed at section 477. (D) Conglomerate of basaltic lavas (Unit ZZ1) exposed at section 482.

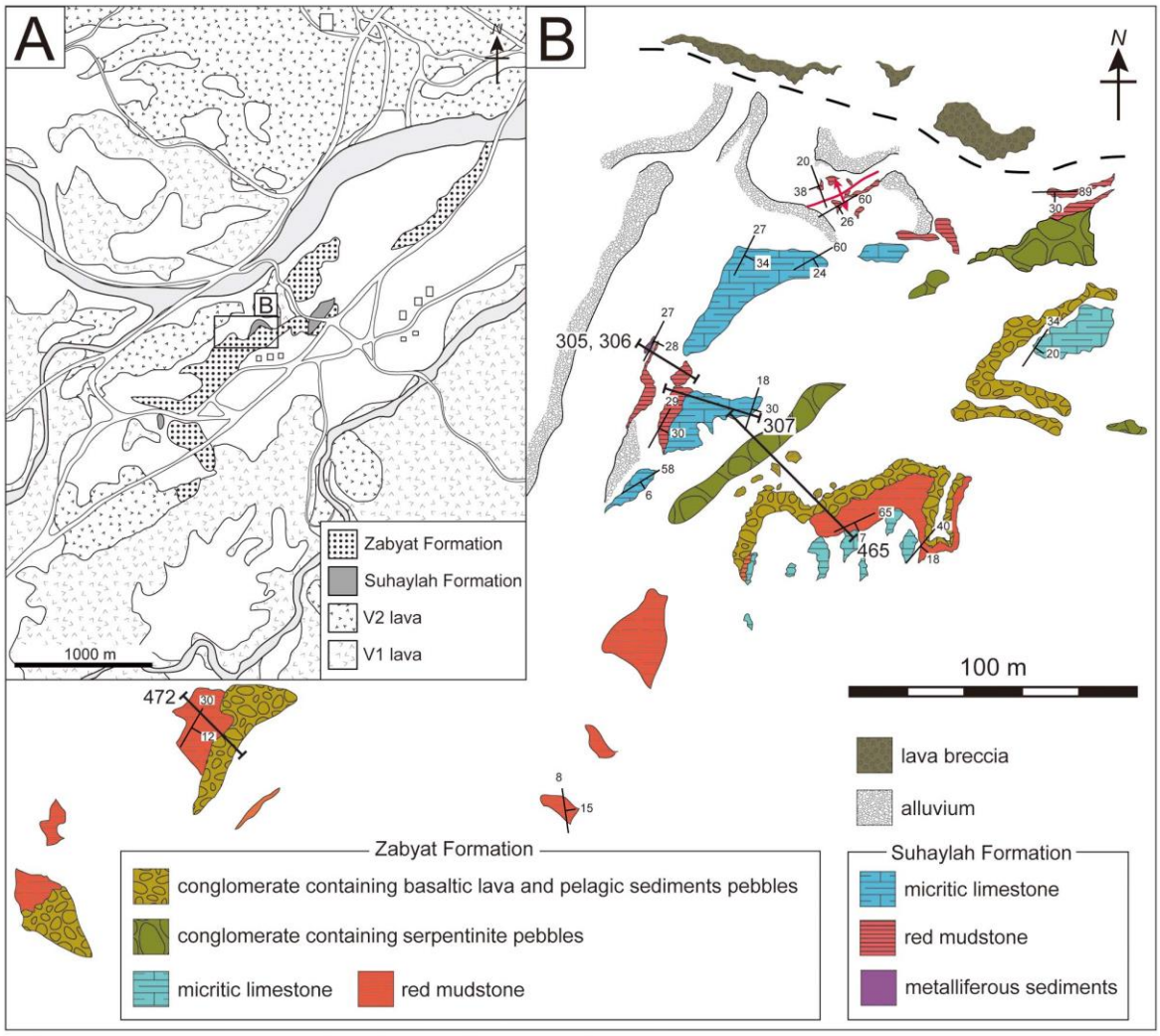

Fig. 10. Index map showing the locations of examined sections at the Lasail exposure. (A) Simplified geological map of the area near the Lasail Mine. See Fig. 1 for the location of the mapped area. The base map is modified from Bishimetal Exploration Co. Ltd. (1987). (B) Geological map of the sampled area.

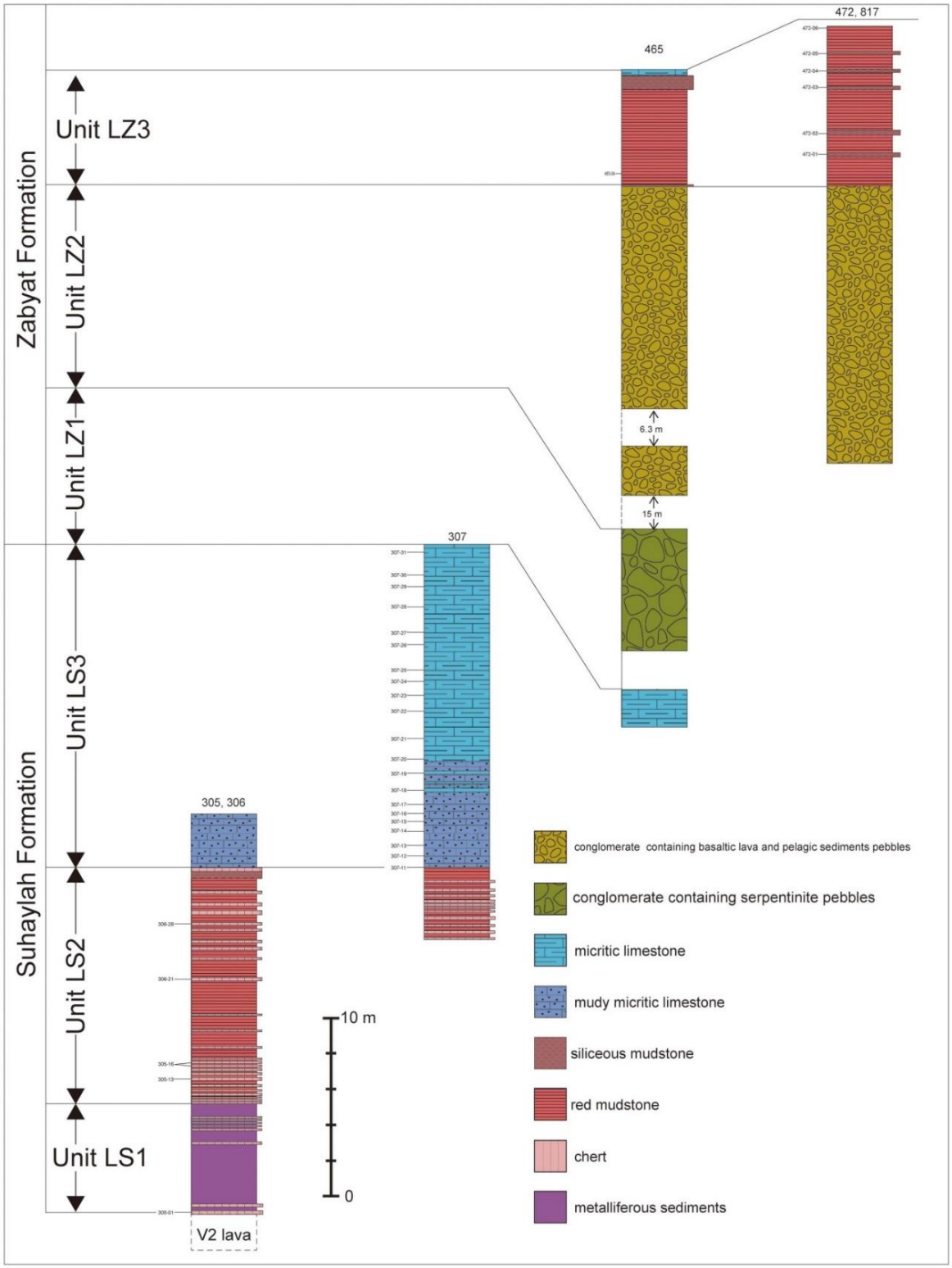

Fig. 11. Lithostratigraphic columns measured within the Lasail exposure and sampling layers. See Fig. 3 for the locations of sections details. Correlations indicated by solid lines are based on key lithostratigraphic boundaries.

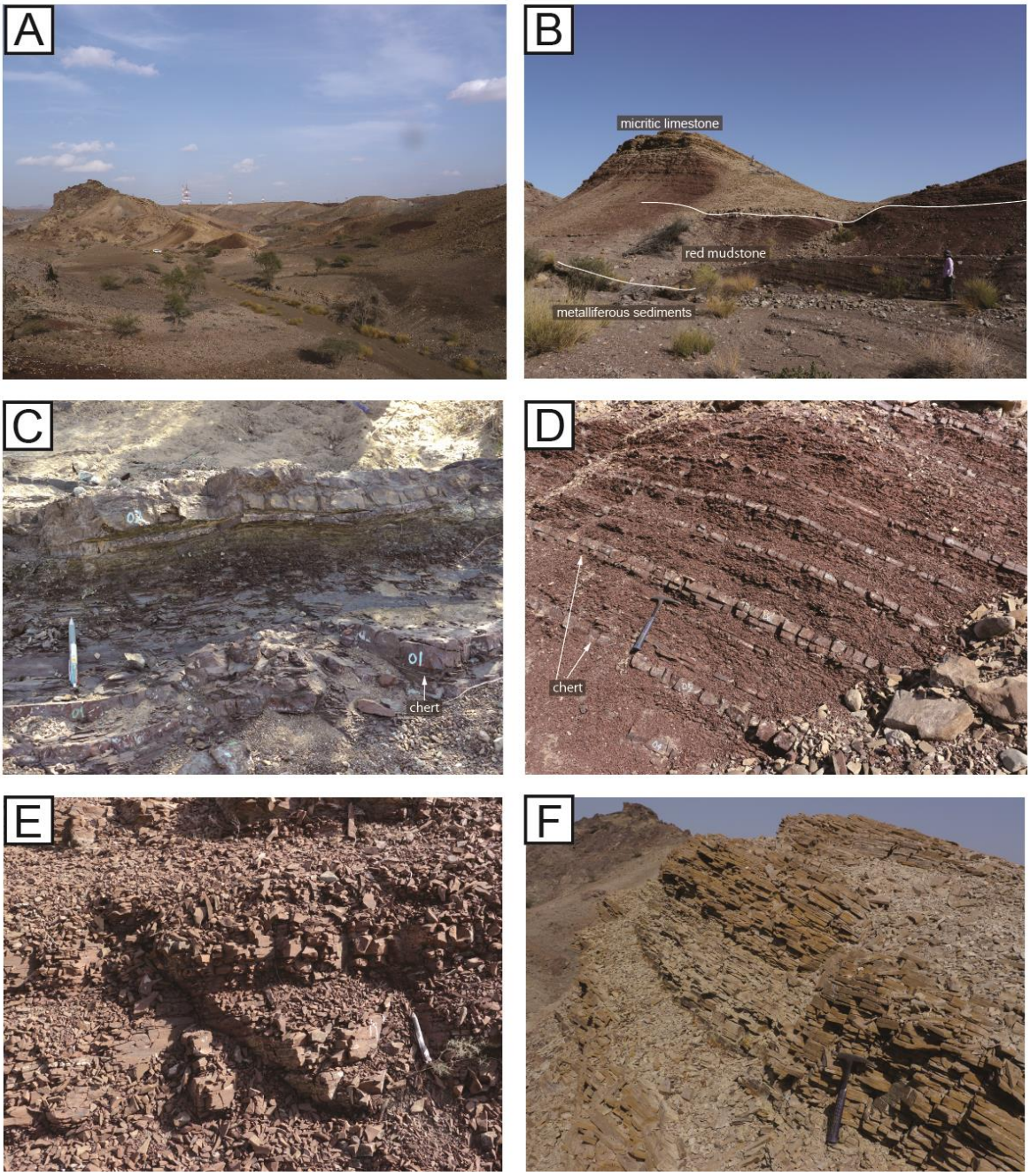

Fig. 12. Outcrop photographs showing the lithologies of sediments in the Lasail exposure. (A) Landscape of Lasail exposure (B) View of outcrops of the Suhaylah Formation. (C) Metalliferous sediments (Unit LS1) and intercalations of chert exposed at section 305. (D) Red mudstone (Unit LS2) and intercalations of chert exposed at section 480. (E) Muddy micritic limestone (Unit LS3) exposed at section 307. (F) Micritic limestone (Unit LS3) exposed at section 307.

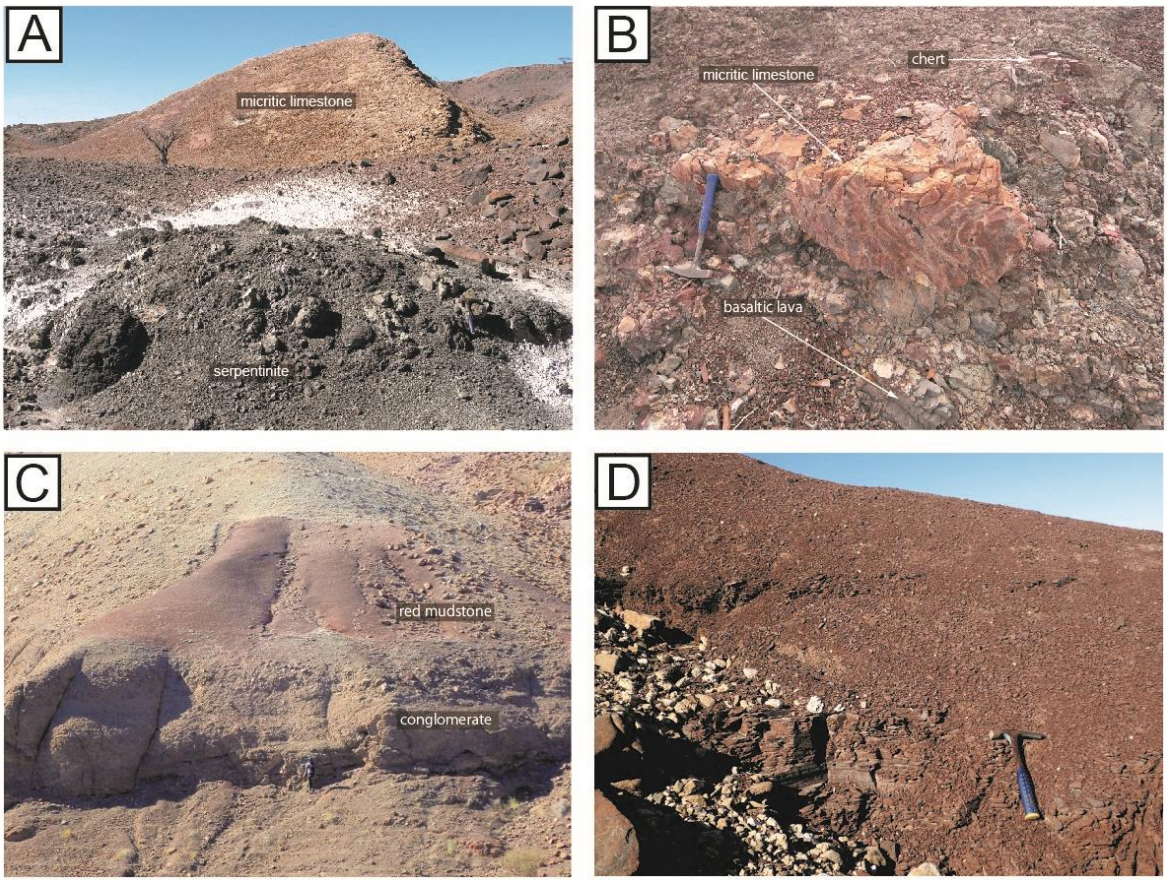

Fig. 13. Outcrop photographs showing the lithologies of sediments in the Lasail exposure. (A) Micritic limestone (Unit LS3) and conglomerate containing serpentinite pebbles (Unit LZ1) exposed at section 307. (B) Conglomerate containing basaltic lava and pelagic sediments (Unit LZ2) exposed at section 465. (C) Conglomerate (Unit LZ2) and red mudstone (Unit LZ3) (D) Red mudstone (Unit LZ3) exposed at section 472.

3. 4. Sediments on the V2 lava (Hilti exposure)

In the Hilti exposure, all the lava of V1, V2, and V3, metalliferous sediments, and pelagic sediments are distributed. In addition, in this area, the thick pelagic sediments are developed on the V2 lava (UV2 lava). Above the UV2 lava, metalliferous sediment (corresponding to Unit ZS1 and Unit LS1), red mudstone (corresponding to Unit ZS 2 and Unit LS2), micritic limestone (corresponding to Unit ZS3 and Unit LZ3), and red mudstone (corresponding to Unit ZS4) are exposed in stratigraphic ascending order. In some section, no red mudstone covering the micritic limestone can be observed and micritic limestone is directly covered by the V3 lava.

4. Geochemical analyses

4. 1. Materials and analytical method

Twenty four samples from the Suhaylah and Zabyat formations were crashed to powder for geochemical analyses. The concentrations of 10 major elements (SiO_2, TiO_2, Al2O_3, Fe_2O_3, MnO, MgO, CaO, Na_2O, K_2O, and P_2O_5) were determined by X-ray fluorescence (XRF) analysis of fused glass beads using a RIX3000 housed at Niigata University. Total Fe content is reported as Fe_2O_3. Loss on ignition (LOI) was measured by weighing the samples before and after 2 h of calcination at 850 °C.

Concentrations of seven trace elements (V, Cr, Ni, Rb, Sr, Zr, and Pb) were determined by analyses of fused glass beads by XRF (Rigaku RIX3000) at Niigata University, Japan. Concentrations of three trace elements (Co, Zn, and Nb) and rare earth elements (REEs) were analyzed by inductively coupled plasma mass spectrometry (ICP-MS) using an Agilent 7500a housed at Niigata University, calibrated using the reference values for BHVO-1 (U.S. Geological Survey; Eggins et al., 1997). Variations in sensitivity during the analytical run were corrected using an internal standard. Samples were prepared using a combined acid digestion procedure (HCl and HF) and alkali fusion by dissolution with a combination of HF–NHO3 and HF–HCl at 150 °C after adding anhydrous Na_2CO_3. Analytical precision, as estimated by relative deviation values using the geological reference material W-2 (U.S. Geological Survey; Eggins et al., 1997), was less than 10%.

For determining the TOC content, 8 samples were selected for analysis from among the samples analyzed for major element concentrations. After the removal of carbonates using 1 N HCl in powdered samples, TOC contents were determined using NA 2500 NCS housed at Kanazawa University.

4. 2. Results of geochemical analyses

The results of geochemical analyses are listed in Tables 1 and 2, and stratigraphic variations in the compositional data are shown in Fig. 14. Chert and red mudstone (E-01, E-02, E-03, E-03.5e, E-04, E-05, E-06, E-07, E-08, E-09, E-10, and 784) from the analyzed succession have high SiO_2 contents, in excess of 80% (Fig. 14). As for the micritic limestone, the value of SiO_2 becomes lower as the upper limit, whereas the upper limit value of CaO becomes higher in reverse (Fig. 14). Al_2O_3 contents vary from 1.59 to 7.8%, although the mean value for the red mudstone is 9.72 % (Fig. 14). Red metalliferous sediments and dark purple metalliferous sediments are characterized by relatively high Fe_2O_3 contents (mean value of 19.07 to 21.92%, Fig. 14), and the dark purple metalliferous sediments are relatively high MnO contents (mean value of 9.42 %, Fig. 14). In addition, the dark purple metalliferous sediments is characterized by high V and Ni contents. The micritic limestone contains high Sr contents in excess of 140 ppm (Table 2).

Figs.15 and 16 shows REE patterns normalized to chondrite. The REE patterns of the metalliferous sediments, red mudstone, chert, and micritic limestone are similar to the pattern of NASC (North American Shale Composite; Gromet et al., 1984; McLennan, 1989). There is a strong cerium anomaly in the sample of Oman. The cerium anomaly (Ce/Ce*) was estimated by the equation Ce/ Ce*=2Cen/(Lan+Prn), where the subscript n indicates a NASC normalized value (De Baar et al., 1985; Murray et al., 1992). The obtained Ce anomalies range from 0.86 to 1.39, showing an increase at the red mudstone and the average value of the chert is 1.05 (Fig. 17).

TOC values for the 8 samples of chert are 0.0038 to 0.0094 %, representing the very low values in the succession (Fig. 18). The obtained values of Th/U are 5.67–6.1 for the red mudstone, 2.06–5.59 for the chert, showing an upward increasing trend and a negative correlation with TOC values (Fig. 17, Fig. 18).

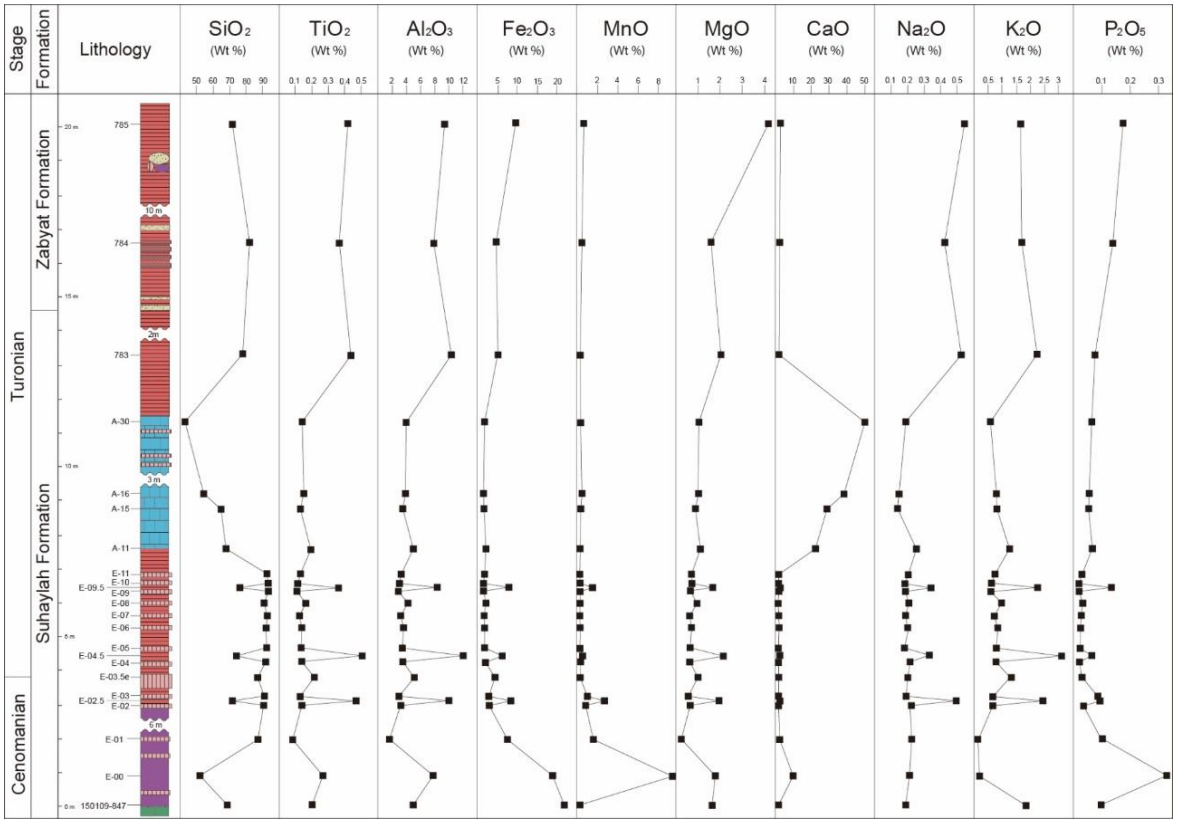

Fig. 14. Lithological column (Suhaylah exposure) and stratigraphic variations in geochemistry of major elements.

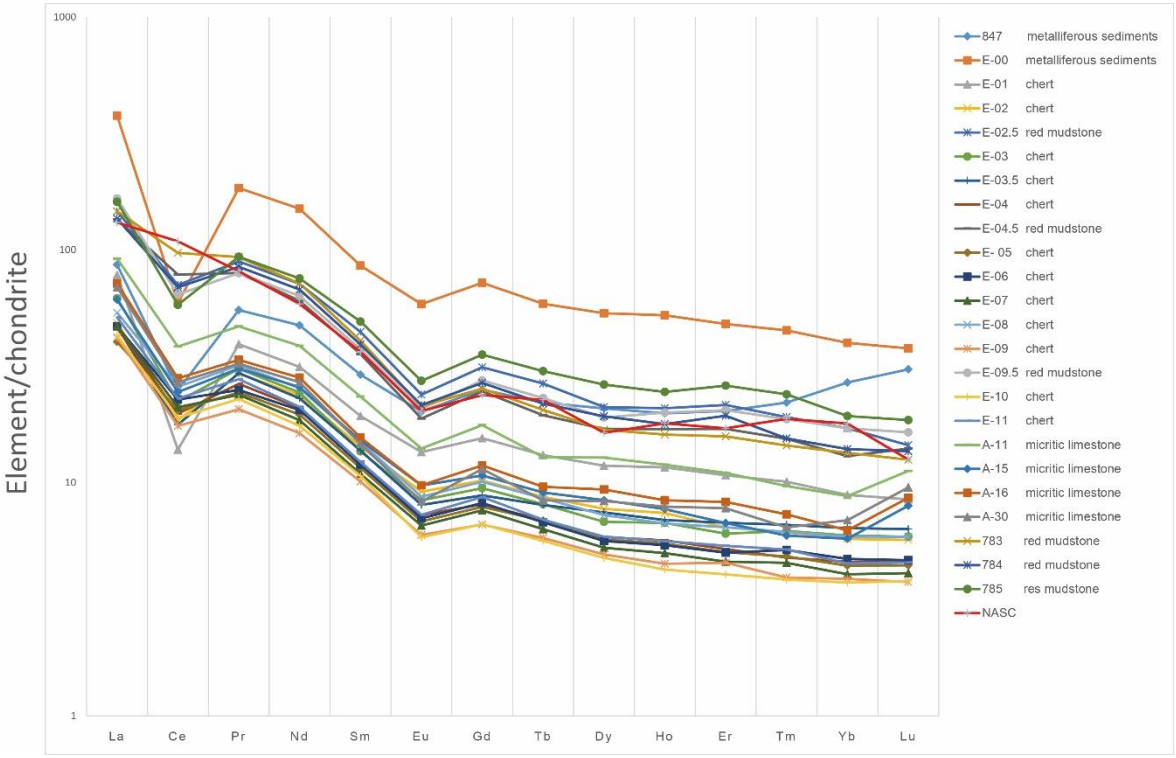

Fig. 15. Chondrite-normalized rare earth element (REE) patterns in the Suhaylah exposure. NASC: North American Shale Composite (Gromet et al., 1984; McLennan, 1989).

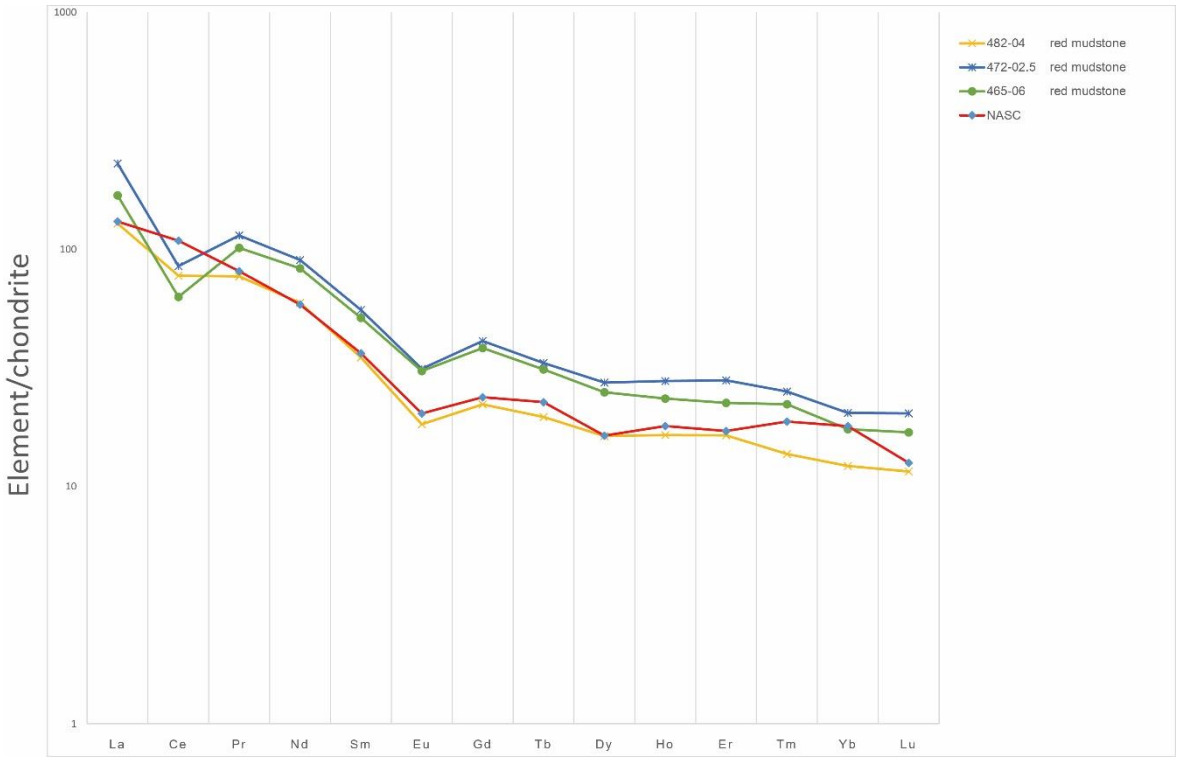

Fig. 16. Chondrite-normalized rare earth element (REE) patterns in the Zabyan and Lasail exposures. NASC: North American Shale Composite (Gromet et al., 1984; McLennan, 1989).

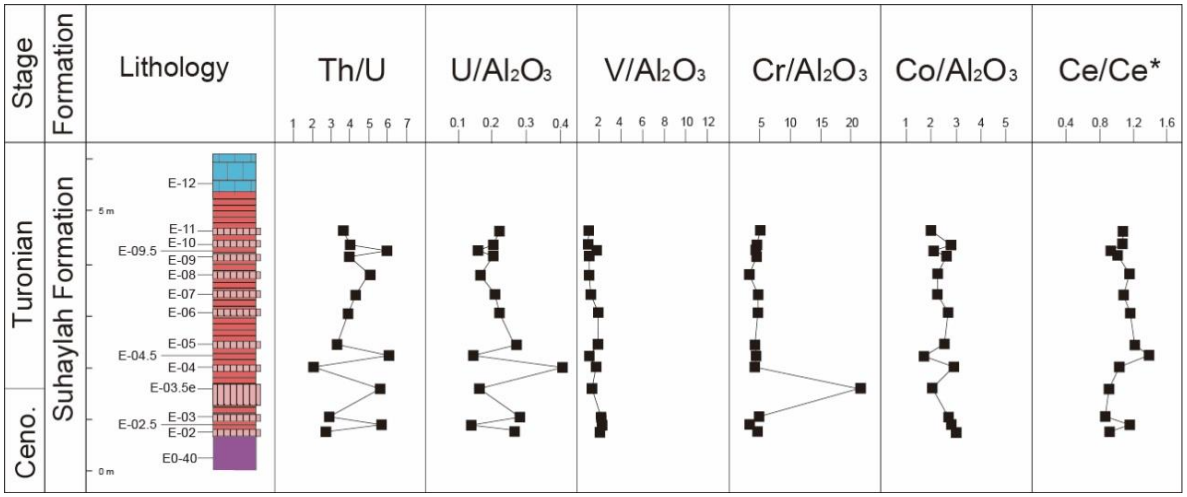

Fig. 17. Lithological column (Suhaylah exposure) and stratigraphic variations in geochemistry of redox indicators. Ce/Ce* is the Ce anomaly (De Baar et al., 1985).

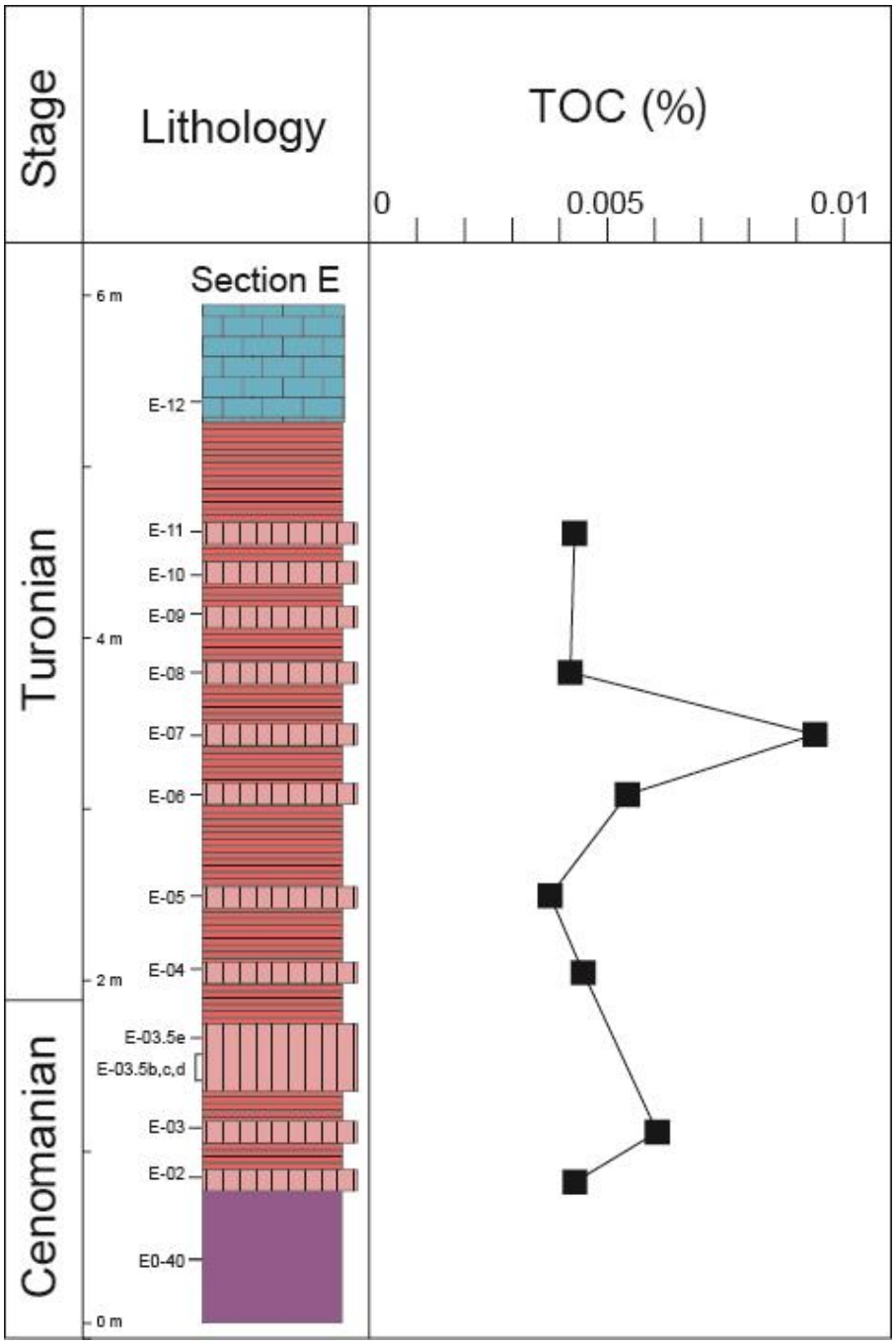

Fig. 18. Lithological column (Suhaylah exposure) and stratigraphic variations of TOC (total organic carbon).

Table 1. Results of geochemical analyses. Fe_2O_3* is total iron as Fe_2O_3. LOI: weight loss on ignition. Ce/Ce* is the Ce anomaly (De Baar et al., 1985). La_n and Ce_n indicate NASC-normalized values. TOC: Total organic carbon.

Section	Suhayl ah	Suhayl ah	Suhayl ah	Suhayl ah	Suhayl ah	Suhayl ah	Suhayl ah	Suhayl ah	Suhayl ah	Suhayl ah	Suhayl ah	Suhayl ah	Suhayl ah	Suhayl ah	Suhayl ah	Suhayl ah	Suhayl ah
Lithology	metasiltstone	metasiltstone	chert	chert	redmudstone	chert	chert	chert	red mudstone	chert	chert	chert	chert	chert	red mudstone	chert	chert
sample No	847	e-00	e-01	e-02	E-02.5	e-03	e-3.5	e-04	E-04.5	e-05	e-06	e-07	e-08	e-09	E-09.5	e-10	e-11
Major element (wt%)																	
SiO2	68.31	51.37	88.38	92.97	71.82	93.32	89.86	93.91	74.75	94.64	95.47	95.19	91.84	95.03	76.51	95.51	91.24
TiO2	0.20	0.27	0.08	0.14	0.47	0.13	0.22	0.14	0.51	0.14	0.14	0.13	0.17	0.11	0.36	0.12	0.13
Al2O3	4.97	7.71	1.62	3.29	10.04	3.03	5.30	3.53	12.17	3.52	3.72	3.27	4.24	2.96	8.41	3.10	3.24
Fe2O3	21.88	18.85	7.79	3.02	8.38	2.88	4.54	2.04	6.27	1.77	1.91	1.76	2.17	1.56	7.82	1.52	1.78
MnO	0.25	9.31	1.63	0.91	2.63	1.01	0.13	0.33	0.52	0.20	0.19	0.14	0.17	0.13	1.50	0.12	0.10
MgO	1.64	1.75	0.23	0.68	1.93	0.56	1.02	0.64	2.14	0.64	0.72	0.62	0.85	0.66	1.67	0.73	0.68
CaO	0.46	8.87	1.41	0.42	1.66	0.44	0.45	0.36	0.98	0.32	0.32	0.29	0.32	0.26	1.35	0.28	0.31
Na2O	0.19	0.21	0.22	0.22	0.49	0.19	0.20	0.21	0.33	0.18	0.20	0.19	0.20	0.18	0.34	0.18	0.20
K2O	1.84	0.16	0.08	0.66	2.43	0.65	1.35	0.79	3.13	0.79	0.86	0.71	0.97	0.60	2.25	0.62	0.71
P2O5	0.10	0.33	0.10	0.04	0.09	0.09	0.03	0.02	0.07	0.02	0.02	0.03	0.03	0.02	0.13	0.02	0.03
Total	99.83	98.81	101.54	102.35	99.95	102.30	103.12	101.97	100.96	102.22	103.55	102.32	101.06	101.54	100.34	102.19	98.41
LOI (%)	3.29	4.85	2.11	2.23	5.76	1.99	3.49	2.07	5.98	2.08	2.14	1.92	2.51	1.87	4.57	1.95	2.06
Trace element (ppm)																	
Ba	149.90	83.90	484.10	103.90	279.00	112.20	108.90	98.70	389.60	83.70	97.30	85.00	102.50	106.80	268.30	75.90	149.20
Cr	47.00	1.80	7.90	14.60	33.00	14.10	110.60	14.10	51.20	14.10	16.00	14.70	17.20	12.70	34.70	13.40	16.30
Nb	3.80	6.04	2.95	3.61	8.36	3.28	4.78	3.95	10.67	3.23	4.31	2.83	4.88	2.51	8.25	3.90	3.73
Ni	70.60	218.50	50.70	20.30	70.80	21.00	27.60	8.70	56.20	13.30	11.10	12.00	19.60	9.50	56.10	13.90	16.10
Rb	65.98	13.17	6.43	29.80	98.72	31.15	61.85	35.81	125.24	34.64	38.70	33.62	43.77	27.52	94.88	28.95	31.85
Sr	52.57	136.42	87.70	62.54	582.04	67.45	69.76	56.60	1132.84	58.38	58.62	49.25	51.47	46.49	425.13	45.55	55.23
V	281.40	727.24	124.65	44.72	163.20	45.47	47.09	41.70	88.70	45.96	47.48	27.52	29.46	20.03	102.60	29.12	23.33
Y	29.62	75.95	16.81	11.70	32.15	12.47	9.77	9.30	25.68	9.22	9.08	8.78	11.24	7.76	32.36	7.13	10.14
Zr	44.90	77.76	23.93	29.25	100.66	28.85	47.63	29.94	113.43	28.46	28.99	25.99	35.61	22.48	89.48	23.72	26.57
Pb	41.48	58.51	31.06	17.51	43.93	20.42	16.38	16.17	35.40	15.99	14.45	15.97	16.16	17.82	53.84	14.64	16.31
REE (ppm)																	
La	20.49	89.58	18.51	11.52	34.75	14.72	11.09	10.95	32.09	9.57	11.15	11.13	12.75	9.99	39.42	10.19	12.16
Ce	15.30	36.30	8.60	11.36	43.32	13.69	10.87	12.14	48.03	12.55	13.95	12.93	15.86	10.76	39.44	11.66	14.09
Pr	5.25	17.53	3.75	2.80	8.49	2.94	2.62	2.53	7.58	2.32	2.36	2.27	3.04	1.97	7.57	2.19	2.65
Nd	22.17	70.23	14.71	11.11	33.44	11.41	10.78	9.79	28.28	9.19	9.60	8.68	11.92	7.64	29.64	8.20	9.89
Sm	4.46	13.12	2.96	2.19	6.81	2.09	2.11	1.83	5.47	1.77	1.83	1.67	2.29	1.55	5.73	1.64	1.88
Eu	1.18	3.40	0.79	0.53	1.39	0.49	0.47	0.42	1.10	0.40	0.41	0.38	0.51	0.35	1.28	0.34	0.42
Gd	5.17	14.87	3.20	2.10	6.45	1.95	1.82	1.66	5.08	1.62	1.69	1.57	2.08	1.36	5.67	1.37	1.79
Tb	0.83	2.20	0.49	0.33	1.00	0.30	0.30	0.26	0.73	0.26	0.25	0.24	0.32	0.22	0.86	0.21	0.26
Dy	5.30	13.61	3.01	1.97	5.38	1.73	1.90	1.49	4.33	1.45	1.43	1.34	1.85	1.25	4.85	1.21	1.49
Ho	1.13	2.97	0.66	0.42	1.19	0.38	0.39	0.32	0.96	0.31	0.31	0.28	0.38	0.25	1.13	0.24	0.32
Er	3.37	7.96	1.78	1.07	3.58	1.00	1.12	0.86	2.82	0.83	0.83	0.76	1.07	0.75	3.40	0.67	0.89
Tm	0.56	1.15	0.26	0.16	0.49	0.16	0.17	0.12	0.39	0.12	0.13	0.12	0.16	0.10	0.48	0.10	0.13
Yb	4.59	6.79	1.51	0.98	2.92	1.01	1.09	0.78	2.21	0.75	0.80	0.69	1.00	0.66	2.92	0.63	0.77
Lu	0.78	0.96	0.22	0.14	0.37	0.15	0.16	0.12	0.36	0.11	0.12	0.10	0.15	0.10	0.42	0.10	0.12
Th	3.32	5.16	1.52	2.31	7.75	2.43	4.57	2.91	10.39	3.08	3.10	2.83	3.42	2.30	7.64	2.45	2.64
U	0.59	1.17	0.44	0.85	1.37	0.84	0.82	1.41	1.70	0.93	0.79	0.66	0.68	0.58	1.28	0.61	0.73
Ce/Ce*	0.69	0.38	0.43	0.91	1.16	0.86	0.91	1.03	1.39	1.22	1.16	1.08	1.15	1.00	0.93	1.06	1.08
TOC				0.0043		0.0061		0.0045		0.0038	0.0054	0.0094	0.0042				0.0043
Th/U	5.62	4.42	3.48	2.71	5.67	2.90	5.59	2.06	6.10	3.31	3.91	4.31	5.02	3.96	5.96	3.99	3.64

Table 2. Results of geochemical analyses. Fe_2O_3* is total iron as Fe_2O_3. LOI: weight loss on ignition. Ce/Ce* is the Ce anomaly (De Baar et al., 1985). La_n and Ce_n indicate NASC-normalized values. TOC: Total organic carbon.

Section	Suhaylah	Suhaylah	Suhaylah	Suhaylah	Suhaylah	Suhaylah	Suhaylah	Zabyan	Zabyan	Zabyan	Lasail	Lasail
Lithology	micritic limestone	micritic limestone	micritic limestone	micritic limestone	red mudstone	red mudstone	red mudstone	chert	chert	red mudstone	red mudstone	red mudstone
sample No	a-11	a-15	a-16	a-30	783	784	785	479-05	479-08	482-04	472-02.5	465-06
Major element (wt%)												
SiO2	68.62	64.93	53.86	43.17	79.01	83.33	72.37	88.37	91.32	80.43	69.80	69.00
TiO2	0.20	0.13	0.15	0.14	0.44	0.37	0.42	0.08	0.07	0.41	0.45	0.33
Al2O3	4.98	3.49	3.92	3.98	10.49	8.14	9.51	2.59	1.79	9.56	10.52	7.59
Fe2O3	2.13	1.58	1.37	1.73	5.45	4.57	9.67	8.61	7.33	5.20	9.48	10.78
MnO	0.73	0.28	0.47	0.31	0.23	0.34	0.81	0.29	0.18	0.20	1.98	2.30
MgO	1.12	0.87	1.02	1.03	2.08	1.66	4.24	0.67	0.29	1.83	1.78	1.75
CaO	21.91	28.12	37.58	49.55	0.71	0.79	1.33	0.32	0.22	1.27	2.57	5.93
Na2O	0.25	0.13	0.17	0.19	0.53	0.43	0.55	0.14	0.13	0.64	0.71	0.50
K2O	1.27	0.80	0.77	0.58	2.25	1.69	1.66	0.41	0.27	2.17	2.77	1.48
P2O5	0.07	0.05	0.06	0.06	0.08	0.14	0.18	0.03	0.02	0.08	0.20	0.15
Total	101.28	100.39	99.36	100.74	101.27	101.44	100.73	101.51	101.61	101.77	100.25	99.79
LOI (%)	16.82	19.76	24.55	29.55	4.31	3.80	4.75	2.72	1.78	4.29	4.93	5.03
Trace element (ppm)												
Ba	287.60	163.30	741.10	1196.90	183.90	117.30	229.90	46.10	60.70	294.50	293.40	277.10
Cr	24.90	20.20	24.10	27.60	49.40	62.60	116.30	24.10	13.10	43.80	43.50	19.90
Nb	4.72	3.78	4.53	3.08	8.92	8.41	6.76	3.00	2.05	7.82	10.29	7.04
Ni	23.70	12.50	13.30	9.80	46.30	67.90	127.80	48.50	47.20	42.20	85.70	77.30
Rb	46.93	32.58	29.47	22.53	101.20	75.22	74.04	20.38	15.51	86.47	106.39	63.55
Sr	143.03	174.25	263.12	369.40	103.81	102.77	101.62	50.40	38.84	693.51	628.37	616.82
V	55.46	24.25	34.62	28.97	89.50	64.90	206.30	152.16	152.69	59.40	146.40	209.00
Y	21.91	15.70	19.43	18.82	25.33	30.12	38.38	8.87	10.43	24.34	42.67	32.34
Zr	47.49	32.89	37.77	40.51	94.55	73.51	78.64	18.66	14.99	90.03	107.04	85.65
Pb	9.06	7.98	11.33	2.22	32.90	31.29	43.54	20.80	32.05	30.41	63.83	57.52
REE (ppm)												
La	21.79	14.50	17.01	16.39	34.70	32.31	38.16	9.30	13.67	30.53	54.74	40.10
Ce	23.56	15.02	17.22	16.53	59.53	42.31	35.62	11.32	13.18	47.47	52.13	38.65
Pr	4.46	2.94	3.21	3.09	8.86	8.05	8.88	2.41	2.71	7.32	10.90	9.66
Nd	18.12	12.04	13.22	12.65	33.54	31.58	35.23	9.35	10.64	27.82	42.20	38.93
Sm	3.59	2.32	2.39	2.25	6.24	6.01	7.55	1.92	2.12	5.37	8.51	7.88
Eu	0.82	0.57	0.57	0.48	1.24	1.25	1.59	0.53	0.55	1.06	1.82	1.78
Gd	3.64	2.21	2.44	2.36	5.22	5.52	7.30	1.83	2.20	4.57	8.46	7.90
Tb	0.48	0.34	0.36	0.31	0.77	0.82	1.13	0.28	0.30	0.74	1.24	1.17
Dy	3.26	2.14	2.38	2.12	4.30	4.91	6.72	1.92	1.85	4.15	6.98	6.35
Ho	0.68	0.44	0.48	0.45	0.91	1.01	1.39	0.37	0.37	0.93	1.58	1.33
Er	1.83	1.11	1.37	1.29	2.62	3.21	4.33	0.99	1.00	2.72	4.65	3.73
Tm	0.25	0.15	0.19	0.16	0.37	0.40	0.61	0.17	0.13	0.35	0.64	0.57
Yb	1.49	0.98	1.06	1.18	2.29	2.38	3.29	1.05	0.76	2.08	3.48	2.97
Lu	0.29	0.20	0.22	0.24	0.32	0.35	0.47	0.17	0.17	0.29	0.52	0.43
Th	3.81	2.48	2.68	2.65	9.19	6.71	6.09	1.22	1.03	7.85	10.15	6.56
U	0.67	0.59	0.73	0.50	1.42	1.06	1.01	0.79	0.38	1.24	1.52	1.25
Ce/Ce*	1.00	0.96	0.94	0.94	1.59	1.22	0.87			1.44	0.88	0.89
TOC												
Th/U	5.73	4.21	3.70	5.25	6.46	6.34	6.02			6.35	6.69	5.24

5. Radiolarian zones and age assignments

5. 1. Materials and methods

More than 400 samples were collected from metalliferous and pelagic sediments of the Suhaylah and Zabyat formations to determine the depositional age. Radiolarians of siliceous samples (red mudstone and chert) were extracted using a standard hydrofluoric acid (HF) etching technique (Dumitrica, 1970; Pessagno and Newport, 1972). Samples of micritic limestone were soaked in a dilute hydrochloric acid (HCl) solution (ca. 38%) for about 24 hours to remove carbonate and were then treated with HF. Well-preserved radiolarians were recovered from metalliferous sediments, chert within metalliferous sediments, red mudstone, chert intercalated with red mudstone, and micritic limestone. Occurrence data of identified species from the samples are provided in Table 3.

5. 2. Radiolarian zones

From the occurrence patterns of the species, four radiolarian zones were defined (Fig. 18, Fig. 25 to 27). The *Guttacapsa gutta* Zone was defined in metalliferous sediments and intercalated chert of units SS1, ZS1, and LS1, and chert interbedded with red mudstone of units SS2, ZS2, and LS2. The *Rhopalosyringium scissum* Zone was defined in red mudstone and chert of units SS2, ZS2, and LS2. The *Foremanina schona* Zone was defined in micritic limestone of units SS3, ZS3, and LS3. The *Eostichomitra perapedhia* Zone was defined in red mudstone of units SS4 and LZ3. In the following sections, the definition, faunal characteristics, and ages of these radiolarian zones are described.

5. 2. 1. *Guttacapsa gutta* Zone

Index species is *Guttacapsa gutta* (Squinabol). The base of this zone is defined by the first appearance of *G. gutta*. The top is defined by the last appearance of *G. gutta* (Fig. 18, Fig. 25).

The *Guttacapsa gutta* Zone is characterized by abundant *Thanarla pulchra* (Squinabol), *Thanarla veneta* (Squinabol), *Novixitus mclaughlini* (Pessagno), *Rhopalosyringium majuroense* Schaaf, *Holocryptocanium barbui* Dumitrica, *Holocryptocanium tuberculatum* Dumitrica, *Holocryptocanium* sp. A, *Guttacapsa biacuta* (Squinabol), *Guttacapsa gutta* (Squinabol), and *Hemicryptocapsa tuberosa* Dumitrica (Fig. 25). Among these species, *T. pulchra*, *T. veneta*, *N. mclaughlini*, and *H. barbui* dominate the assemblage of the metalliferous sediments and chert of Unit SS1. In contrast, *G. biacuta* and *G. gutta* are less abundant in the sediments of Unit SS1 but they are abundant in the basal part of Unit SS2, particularly in the chert. *Dactyliosphaera silviae* Squinabol, *Dactyliodiscus longispinus* (Squinabol), *Archaeodictyomitra montisserei* (Squinabol), *Rhopalosyringium petilum* (Foreman), *Pseudotheocampe* sp. A, and *Myllocercion* sp. are sparsely present in this zone. All species listed above disappear at horizons within Unit SS2. *Dictyomitra multicostata* Zittel, *Hemicryptocapsa prepolyhedra* Dumitrica, *Hemicryptocapsa polyhedra* Dumitrica, *Pseudodictyomitra pseudomacrocephala* (Squinabol), *Pseudodictyomitra tiara* (Holmes), *Rhopalosyringium elegans* (Squinabol), *Rhopalosyringium hispidum* O'Dogherty, and *Stichomitra communis* Squinabol occur in the *G. gutta* Zone to the *Eostichomitra perapedhia* Zone.

5. 2. 2. *Rhopalosyringium scissum* Zone

Index species is *Rhopalosyringium scissum* (O'Dogherty). The base of this Zone is defined by the first appearance of *R. scissum*. The top is defined by the first appearance of *Foremanina schona* (Fig. 18, Fig. 26).

The *Rhopalosyringium scissum* Zone is characterized by the abundance of *Rhopalosyringium scissum*, *Dictyomitra formosa* Squinabol, *Dictyomitra*

multicostata Zittel, *Hemicryptocapsa polyhedra* Dumitrica, *Stichomitra communis* Squinabol, *Eostichomitra* sp. A, and *Alievium superbum* (Squinabol) (Fig. 26). *Crucella cachensis* Pessagno, *Praeconocaryomma californiaensis* Pessagno, and *Praeconocaryomma universa* Pessagno are also present. *Pseudotheocampe urna* (Foreman) begins to appear in the chert interbedded within red mudstone of Unit SS2. In this zone, *Rhopalosyringium scissum* is abundant in all analyzed sections and has its first occurrence (FO) in sample E-03.5e (ca. 10 cm above E-03.5d, which yielded the *G. gutta* Zone) in section 846.

5. 2. 3. *Foremanina schona* Zone

Index species is *Foremanina schona* Empson-Morin (Fig. 18, fig. 26) The base of this zone is defined by the first appearance of *F. schona*. The top is defined by the first appearance of *Eostichomitra perapedhia* (Fig. 18, Fig. 26).

The *Foremanina schona* Zone is characterized by the FOs of *Annikaella omanensis* De Wever, Bourdillon-de Grissac, and Beurrier, *Myllocercion valgus* (De Wever, Bourdillon-de Grissac, and Beurrier), *Foremanina schona* Empson-Morin, *Patellula verteroensis* (Pessagno), *Patellula ecliptica* O'Dogherty, *Patellula helios* (Squinabol), *Praeconocaryomma lipmanae* Pessagno, and *Pseudoaulophacus putahensis* Pessagno (Fig. 26). In addition to these species, the following are also abundant: *Rhopalosyringium scissum* O'Dogherty, *Hemicryptocapsa polyhedra* Dumitrica, *Dictyomitra formosa* Squinabol, *Dictyomitra multicostata* Zittel, *Pseudodictyomitra* sp. A, *Pseudodictyomitra* sp. B, *Pseudotheocampe urna* (Foreman), *Amphipternis* sp. cf. *A. stocki* (Campbell and Clark), *Alievium superbum* (Squinabol), *Crucella cachensis* Pessagno, Praeconocaryomma californiaensis Pessagno, and *Praeconocaryomma universa* Pessagno. The LO of *Pseudodictyomitra pseudomacrocephala* (Squinabol) is recognized in sample C-28 from near the top of the Suhaylah Formation in section 059-2 (Table 3).

5. 2. 4. *Eostichomitra perapedhia* Zone

Index species is *Eostichomitra perapedhia* (Bragina). The base of this zone is defined by the first appearance of *E. perapedhia*. The top is defined by the last appearance of *E. perapedhia* (Fig. 18, Fig. 27).

The *Eostichomitra perapedhia* Zone , recovered from Unit SS4 (849-783), Unit ZS4 (482-05), and Unit LZ3 (472-05), is characterized by the occurrence of *Dictyomitra multicostata* Zittel, *Hemicryptocapsa polyhedra* Dumitrica, *Xitus plenus* Pessagno, *Stichomitra manifesta* Foreman, *Pseudotheocampe urna* Foreman, *Myllocercion valgus* (De Wever, Bourdillon-de Grissac, and Beurrier), *Alievium gallowayi* Pessgno, *Annikaella omanensis* De Wever, Bourdillon-de Grissac, and Beurrier, *Dictyomitra* aff. *formosa* (Squinabol), *Pseudodictyomitra crassa* Bragina, *Theocampe salillum* Foreman, *Eostichomitra perapedhia* (Bragina), *Archaeospongoprunum* aff. *bipartitum* Pessagno (Fig. 27). In particular, *D. multicostata*, *X. plenus*, *P. urna*, *A. gallowayi*, *A. omanensis*, *Dictyomitra* aff. *formosa* occur abundantly in this zone. The FOs of *Dictyomitra* aff. *formosa*, *P. crassa*, *T. salillum*, *E. perapedhi*a, *Archaeospongoprunum* aff. *bipartitum* are recognized in this zone.

4. 2. 5. Age of *Guttacapsa gutta* Zone

Of the species listed above, *T. pulchra* and *T. veneta* are well known from the Albian to Cenomanian worldwide, with last occurrences (LOs) at the top of the upper Cenomanian (Pessagno, 1977; O'Dogherty, 1994; Bragina, 2004; Musavu-Moussavou et al., 2007). According to the occurrence data of O'Dogherty (1994) that were obtained from the Northern Apennines (Italy) and the Betic Cordillera (Spain), the strata yielding *G. gutta* Zone of this study can be correlated with the *Silviae* Zone (*Dactyliosphaera silviae* Zone) of the uppermost early-late Cenomanian age, based on the occurrences of *D. silviae*, *Guttacapsa* species, *R. majuroense*, and *N. mclaughlini*. In this zone,

D. longispinus was recovered from the lowest radiolarian-bearing horizon of Unit SS1 of section 846 (sample E0-370). This species has been reported from Unitary Associations (UAs) 13 to 18 (middle Albian to late Cenomanian) and latest Cenomanian (Musavu-Moussavou et al., 2007). *Rhopalosyringium petilum*, of which the UAs are in the range 14 to 18 (late Albian to late Cenomanian), are also present in this assemblage. Furthermore *G. biacuta* and *G. gutta* are commonly found in *G. gutta* Zone. The range of *G. biacuta* and *G. gutta* are restricted to UAs 17 to 19, corresponding to the upper part of the *Spica* Subzone (*Patellula spica* Subzone) and the whole *Biacuta* Subzone (*Guttacapsa biacuta* Subzone) of the *Silviae* Zone. This interval has been correlated to the middle to upper Cenomanian (Fig. 19 of O'Dogherty, 1994). In the present study, the LOs of *G. biacuta* and *G. gutta* are recognized in horizons (samples E-03 and E-03.5d, respectively) within Unit SS2 of section 846. Considering all data together, it appears reasonable to assign a middle to late Cenomanian age to *G. gutta* Zone, placing emphasis on the occurrences of *G. biacuta* and *G. gutta* (Fig. 23).

5. 2. 6. Age of *Rhopalosyringium scissum* Zone

To determine the age of *R. scissum* Zone, we mainly follow the radiolarian studies of O'Dogherty (1994) and Musavu-Moussavou et al. (2007). O'Dogherty (1994) established the *Superbum* Zone (*Alievium superbum* Zone) for the Turonian. The FOs of *A. superbum* and other species such as *R. scissum* and *C. cachensis* have been reported as being at the base of this zone. The UAs of these species are in the range 20 to 21, indicating a Turonian age (Fig. 23).

In addition, the precise correlation between our studied section and the late Cenomanian to early Turonian stratigraphic intervals (around the Bonarelli level: BL) of Europe can provide an upper age limit for *G. gutta* Zone. In this interval, the late Cenomanian oceanic anoxic event (OAE2) is a well-known geological event characterized by widespread deposition of

organic-rich marine sediments, associated with a large perturbation of the carbon cycle (e.g., Schlanger and Jenkyns, 1976; Arthur et al., 1988). Many radiolarian studies have been conducted on the BL in terms of paleoenvironmental changes and radiolarian response during the OAE2 (e.g., Erbacher, 1994; Bąk, 2011). Musavu-Moussavou et al. (2007) examined the detailed radiolarian biostratigraphy across the BL of the Gubbio section, Italy, which is the one of the representative sections of the OAE2 (e.g., Tsikos et al., 2004; Wagreich et al., 2008). This section contains bituminous black mudstone and shale alternating with green-gray silty shale, radiolarian-rich mudstone, and silty sandstone, and is assigned to the latest Cenomanian (Whiteinella archaeocretacea Zone). Musavu-Moussavou et al. (2007) compiled the stratigraphic ranges of radiolarians across the BL from previous studies (Marcucci Passerini et al., 1991; Erbacher, 1994; Erbacher and Thurow, 1997; O'Dogherty, 1994; Gallicchio et al., 1996; Salvini and Marcucci Passerini, 1998). In Gubbio, the LOs of *G.* b*iacuta*, *G. gutta*, and *R. majuroense* were recognized in the lower part of the BL (sample BL 1/02 of Musavu-Moussavou et al., 2007). In our section 846, the LOs of *G. biacuta* and *R. majuroense* are recognized in the horizon of sample E-03. The LO horizon of *G. gutta* is sample E-03.5d. Based on the correlation of the LO horizon of *G. gutta*, the uppermost part yielding *G. gutta* Zone (basal part of Unit SS2) is assigned to the latest Cenomanian (Fig. 23).

Musavu-Moussavou et al. (2007) recognized the FOs of *A. superbum*, *H. polyhedra*, and *C. cachensis* in the interval of the BL and placed the base of the *Superbum* Zone in the latemost Cenomanian (within the *W. archaeocretacea* Zone). The FO of *R. scissum* was recognized in the limestone several tens of centimeters above the BL (sample BTT 566 of Musavu-Moussavou et al., 2007). *Dictyomitra multicostata* also first appeared in the limestone overlying the BL (sample BTT 564 of Musavu-Moussavou et al., 2007). In the Gubbio section, the Cenomanian-Turonian boundary deduced from the $\delta^{13}C$ profile and the biostratigraphic marker (the calcareous

nannofossil *Quadrum gartneri* Prins and Perch-Nielsen) was placed ca. 1 m above the stratigraphic top of the BL (Tsikos et al., 2004). The FOs of *R. scissum* and *D. multicostata* in the Gubbio section are thus considered to be very close to the base of the Turonian. In the Suhaylah Formation, the FO of *R. scissum*, which is a potential biostratigraphic marker for the base of the Turonian, was confirmed at the horizon of sample E-03.5e. Based on the correlation between the radiolarian occurrences of the Gubbio section and the section analyzed in this study (section 846), the stratigraphic interval from sample E-03.5e to E-04 at section 846 could be considered to contain the C-T boundary (Fig. 24). Considering all the data together, we conclude that the age of *R. scissum* Zone is early Turonian (Fig. 23).

5. 2. 7. Age of *Foremanina schona* Zone

This assemblage contains typical Turonian species such as *R. scissum*, *H. polyhedra*, *A. superbum*, and *C. cachensis* (e.g., O'Dogherty, 1994; Musavu-Moussavou et al., 2007). Considering the stratigraphic relationship to *R. scissum* Zone (early Turonian), it is reasonable to conclude that the age of the basal micritic limestone of Unit SS3, which yields *F. schona* Zone, is within the Turonian, because the limestone changes gradually from the underlying red mudstone of Unit SS2 that contains *R. scissum* Zone. However, *F. schona* Zone contains some species previously known to occur from the Coniacian onward. For example, *A. omanensis* is present abundantly in this assemblage, and is considered to be Santonian (De Wever et al., 1988) or late Coniacian to late Santonian in age (O'Dogherty et al., 2009). *Foremanina schona* has been reported from the Campanian (Empson-Morin, 1981; Urquhart and Banner, 1994; Moix et al., 2009) and *M. valgus* from the Santonian-Campanian (De Wever et al., 1988). This combination of species makes the age of the assemblage unclear; however, as a similar example to *F. schona* Zone, Dumitrica et al. (1997) reported a Late Cretaceous radiolarian assemblage containing *A. omanensis* and *M. valgus*

from the Masirah ophiolite of Oman, and noted that that assemblage possessed many species in common with the early Turonian assemblage described by O'Dogherty (1994). Robin et al. (2010) also reported *A. omanensis* in assemblage with typical Turonian species such as *H. polyhedra* from deep-water sediments in Iran (Pichakun nappes). We conducted research on the radiolarians of the micritic limestone by checking over 3,000 specimens, using SEM identifications. As a result, *F. schona* Zone did not contain typical index species of Santonian to Campanian age, such as *Dictyomitra koslovae* Foreman, *Amphipyndax pseudoconulus* (Pessagno), *Amphipyndax tylotus* Foreman, and *Pseudoaulophacus floresensis* Pessagno (e.g., Hollis and Kimura, 2001).

For age constraints on *F. schona* Zone, the occurrence of *P. pseudomacrocephala* at the top of the studied section indicates that the upper age limit of this zone is approximately within the Turonian (Pessagno, 1977; O'Dogherty, 1994; Bragina, 2004). In conclusion, the age of *F. schona* Zone is determined as Turonian in the present study (Fig. 23).

5. 2. 8. Age of *Eostichomitra perapedhia* Zone

In the present study, the age assignment for *E. perapedhia* Zone is based on the radiolarian studies by Bandini et al. (2008) and Bragina (2016). According to Bandini et al. (2008), *A. gallowayi* is appeared from middle Turonian to Maastrichtian, *T. salillum* is from Coniacian to Maastrichtian, and *E. perapedhia* is from Coniacian to Santonian. Bragina (2016) reported that the age ranges of *E. perapedhia* and *P. crassa* are from middle Turonian to Santonian and from Coniacian to Santonian, respectively. In addition, this Zone does not contain the typical species of Santonian to Campanian age, such as *D. koslovae* (e.g., Sanfilippo and Riedel, 1985; Hollis and Kimura, 2001). Here, we conclude that the age of *E. perapedhia* Zone is middle Turonian to Coniacian, most possible Coniacian (Fig. 23).

6. Occurrence pattern of radiolarians and faunal characteristics

6. 1. Occurrence pattern and faunal characteristics of the *Guttacapsa biacuta* Zone

Dactyliodiscus longispinus (Squinabol) and *Protoxiphotractus ventosusu* O'Dogherty are occurred only from E0-370 of Unit SS1. The FO horizons of *Holocryptocanium geyserensis* Pessagno, *Pseudodictyomitra quasilodogaensis* Pessagno, and *Theocampe praevandwrhoofi* (Bragina) are E0-370 in the middle part of Unit SS1, and their LO horizons are E0-40. In particular, among these species, *T. praevandwrhoofi* shows characteristic occurrence in E0-40. The FO horizons of *Rhopalosyringium euganeum* (Squinabol) and *Thanarla pulchra* (Squinabol) are E0-370 in the middle part of the Unit SS1, and their LO horizons are E-02 in the lower part of Unit SS2. *T. pulchra* occurs a lot from E0-210 to E-02, and in particular, it shows characteristically abundant occurrence in E-02. The FO horizons of *Guttacapsa biacuta* (Squinabol), *Rhopalosyringium majuroense* Schaaf, *Acanthocircus multidentatus* (Squinabol), and *Dactyliosphaera silviae* Squinabol are E0-370 in the middle part of Unit SS1, and their LO horizons are E-03 in the lower part of Unit SS2. *G. biacuta* occurs a lot in E-02 and E-03, and *R. majuroense* occurs a lot from E 0-370 to E-03. Especially this species occur abundantly in E0-370. The FO horizons of *Dictyomitra naparnsis* Pessagno and *Thanarla* sp. are E0-370 in the middle part of Unit SS2, and their LO horizons are E-03.5b of Unit SS2. The FO horizons of *Holocryptocanium tuberculatum* Dumitrica and *Novixitus mclaughlini* (Pessagno) are E0-370 in the middle part of Unit SS1, and their LO horizons are E-03.5c in the lower part of Unit SS2. The FO horizon of *Dictyomitra montisserei* (Squinabol) is E-210 in the middle part of Unit SS1, and the LO horizon is E0-03.5c in the lower part of Unit SS2. *N. mclaughlini* occurs a lot in E0-40, and it is occurred again in E-03. 5c. There is no occurrence interval (E - 02, E - 03, E-03.5b). *D. montisserei* occurs a lot in E-03.

The FO horizons of *Guttacapsa gutta* (Squinabol), *Holocryptocanium astiensis* Pessagno, *Pseudodictyomitra pseudomacrocephala* (Squinabol), *Sethocapsa bossoensis* Salvini and Passerini, *Thanarla veneta* (Squinabol), *Xitus picenus* Salvini and Passerini, and *Guttacapsa* sp. are E0-370 in the middle part of Unit SS1, and their LO horizons are E-03.5d in the lower part of Unit SS2 (uppermost part of *G. gutta* Zone). Among these species, *H. astiensis* occurs a lot from E-03.5 to E-03.5 d. *T. veneta* occurs a lot in E0-40. *Guttacapsa* sp. occurs abundantly from E-02 to E-03.5c and decreases at E0-03.5 d.

6. 2. Occurrence pattern and faunal characteristics from the *Guttacapsa gutta* Zone to the *Rhopalosyringium scissum* Zone

The LO horizon of *Cryptamphorella conara* (Foreman) is E0-370 of Unit SS1, and the LO horizon is E-05 of Unit SS2. This species occurs a lot from E-03.5c to E-03.5f. The LO horizon of *Stichomitra communis* Squinabol is E0-370 of Unit SS1, and the LO horizon is E-10 of Unit SS2. This species occurs abundantly in E0-370 and E0-210 in the middle part of Unit SS1, and it also occurs a lot from E-05 to E-10 of Unit SS2. The FO horizon of *Myllocercion* sp. is E-370 of Unit SS 1, and the LO horizon is E-11 of Unit SS2. This species occurs a lot in E-03. The FO horizons of *Hemicryptocapsa prepolyhedra* Dumitrica, *Pseudodictyomitra tiara* (Holmes), and *Holocryptocanium* sp. are E0-370 of Unit SS1, and the LO horizons are E-19 of Unit SS3. In particular, *H. prepolyhedra* and *Holocryptocanium* sp. show dramatic increases from E -03.5b to E-03.5d of Unit SS2, and they are hardly occurred at upper levels. The FO horizons of *Rhopalosyringium hispidum* O'Dogherty, *Sciadiocapsa multiradiata* O'Dogherty, and *Praeconocaryomma universa* Pessagno are E0-370 of Unit SS1, and their LO horizon are 472-05 of Unit LZ3. Among these species, *R. hispidum* increases in occurrence from E-03.5b to E-03.5d of Unit SS2, and it increases dramatically from E-03.5e through E-11. The FO horizon of *Holocryptocanium barbui* Dumitrica is E0-210 of Unit SS1, the LO

horizon is E-16 of Unit SS3. This species is common in E0-40. It does not occur E-05, and it poorly occurs from E-05. The FO horizon of *Hemicryptocapsa polyhedra* Dumitrica is E0-40 of Unit SS1, and the LO horizon is 472-05 of Unit LZ2. This species occurs a lot from E-03.5 to E-03.5d. The FO horizons of *Dictyomitra formosa* (Squinabol), *Rhopalosyringium adriaticum* O'Dogherty, and *Alievium superbum* (Squinabol) are E0-40 at upper part of Unit SS1, and the LO horizon is E-19 of Unit SS3. *D. formosa* occurs a lot in E0-40 which is the FO horizon, and this species does not occur from upper part of E-07. *R. adriaticum* occurs a lot in E-03.5c and E-03.5d, and it is occurred in the upper level, although the number of specimens decreases. *A. superbum* does not occur until E-03.5 after being occurred at E-02. The FO horizon of *Dictyomitra densicostata* Pessagno is E-02 at the uppermost Unit SS1, and the LO horizon is E-11. This species frequently occurs from E-03.5e to E-11 which is the LO horizon, and are frequently occurred from E-03.5e to E-05. The FO horizon of *Archaeocenosphaera*? *mellifera* O'Dogherty is E-03.5b, and LO is E-07. This species occurs a lot in E-03.5E. The FO horizon of *Eostichomitra* sp. is E-03.5b of Unit SS2, and the LO horizon is 472-05 of Unit LZ2. This species increases dramatically from E-03.5e, and this trend continues until E-07. The FO horizon of *Rhopalosyringium radiosum* O'Dogherty is E-03.5c of Unit SS2, and E-05 is the LO horizon. This species occurs a lot from E-03.5f and E-04.

6. 3. Occurrence pattern and faunal characteristics from the *Rhopalosyringium scissum* Zone

The FO horizon of *Dictyomitra* sp. is E-03.5e, and the LO horizon is E-10. This species occurs a lot from E-03.5e to E-05. The FO horizons of *Rhopalosyringium scissum* O'Dogherty and *Praeconocaryomma californiaensis* Pessagno are E-03.5e of Unit SS1, and the LO horizons are E-19 of Unit SS3. *R. scissum* occurs a lot from E-03.5e to E-11, especially

from E-03.5e to E-04. The FO horizon of *Pseudotheocampe tina* Foreman is E-05 of Unit SS 2, and the LO horizon is E-19 of Unit SS 3. This species is abundant from E-05 to E-11.

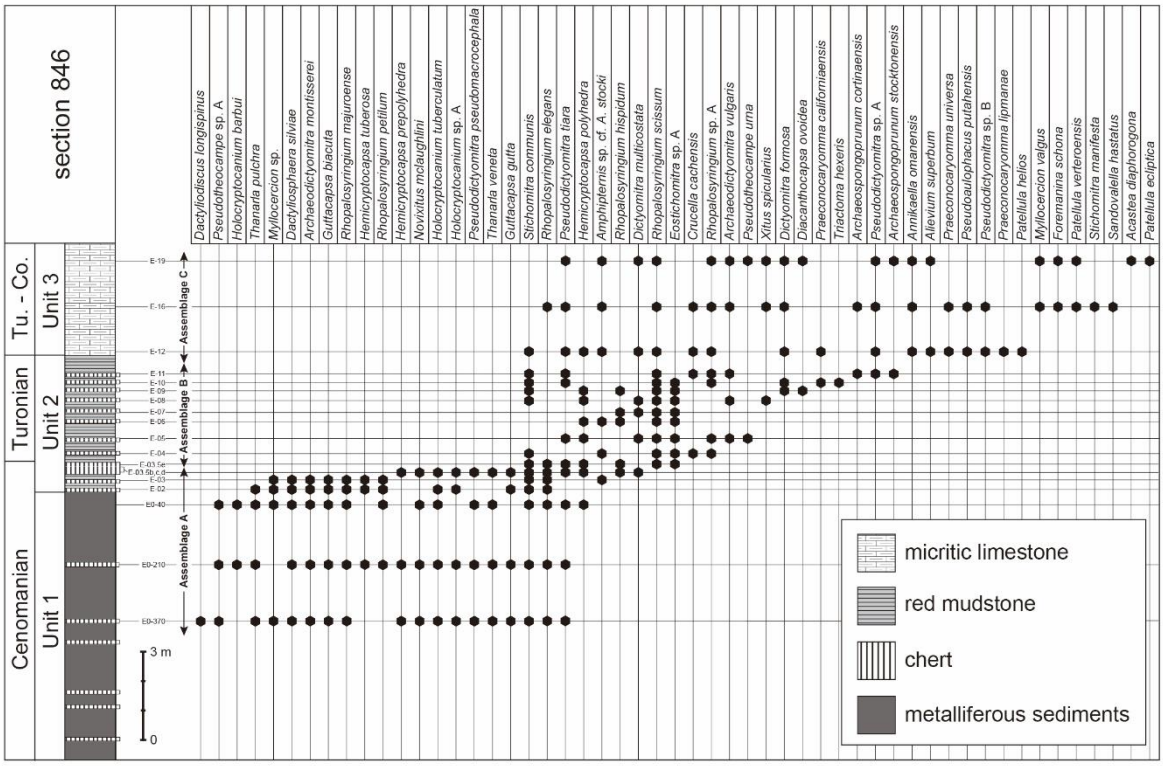

Fig. 19. Occurrence of Late Cretaceous radiolarians in section 846. Tu.: Turonian, Co.: Coniacian.

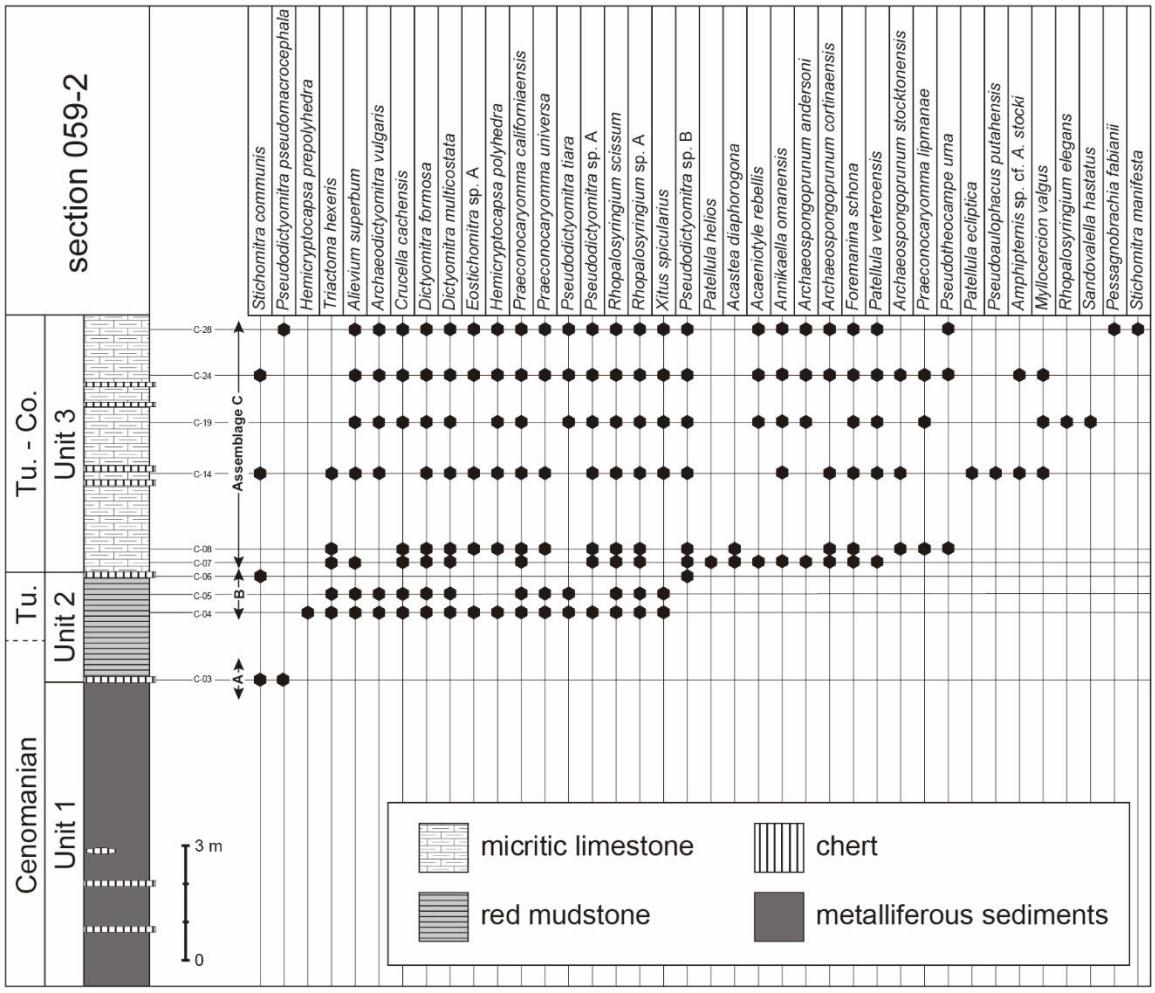

Fig. 20. Occurrence of Late Cretaceous radiolarians in section 059-2. Tu.: Turonian, Co.: Coniacian.

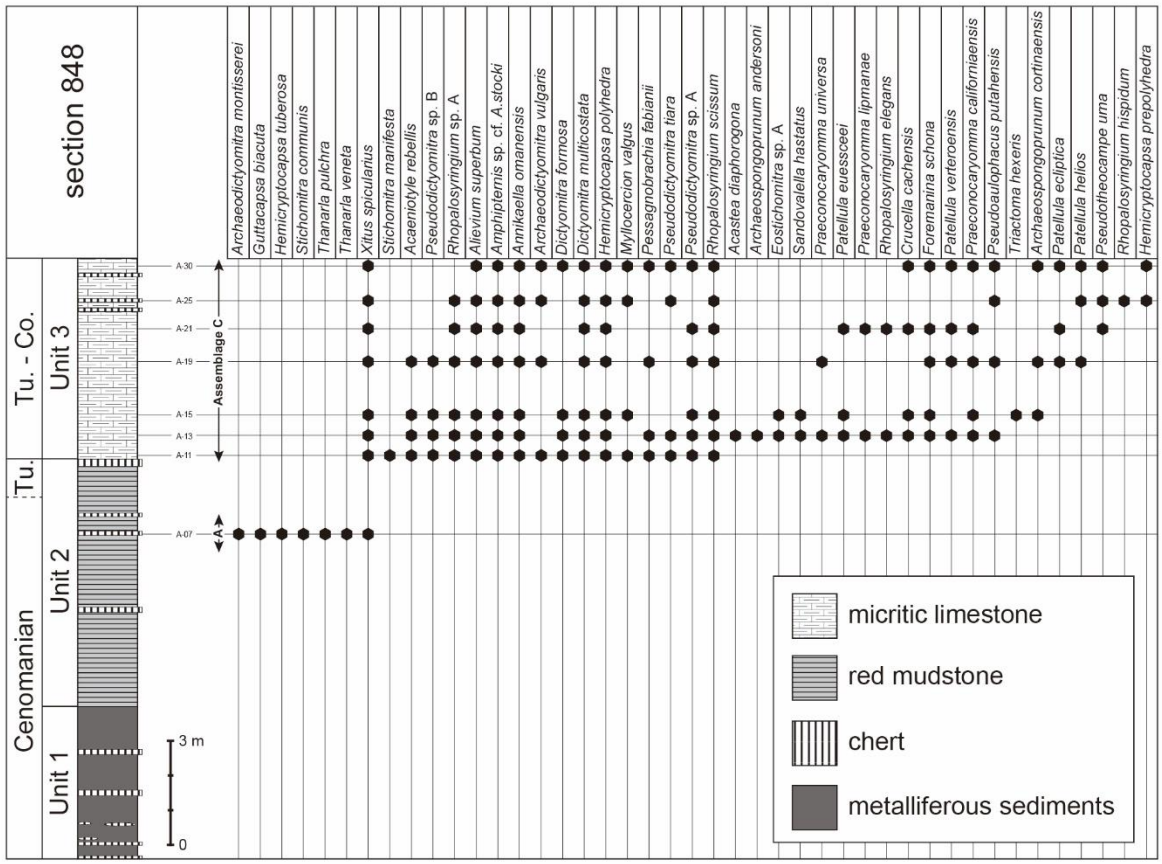

Fig. 21. Occurrence of Late Cretaceous radiolarians in section 848. Tu.: Turonian, Co.: Coniacian.

Table 3. List of Late Cretaceous radiolarians from the Suhaylah and Zabyat formations.

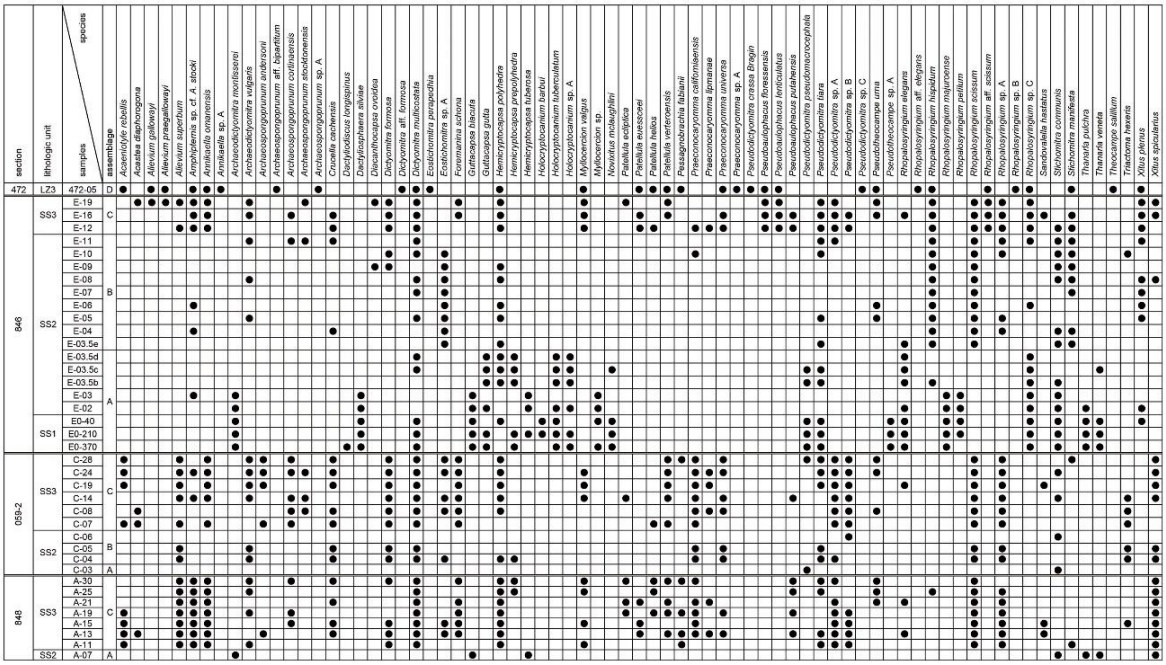

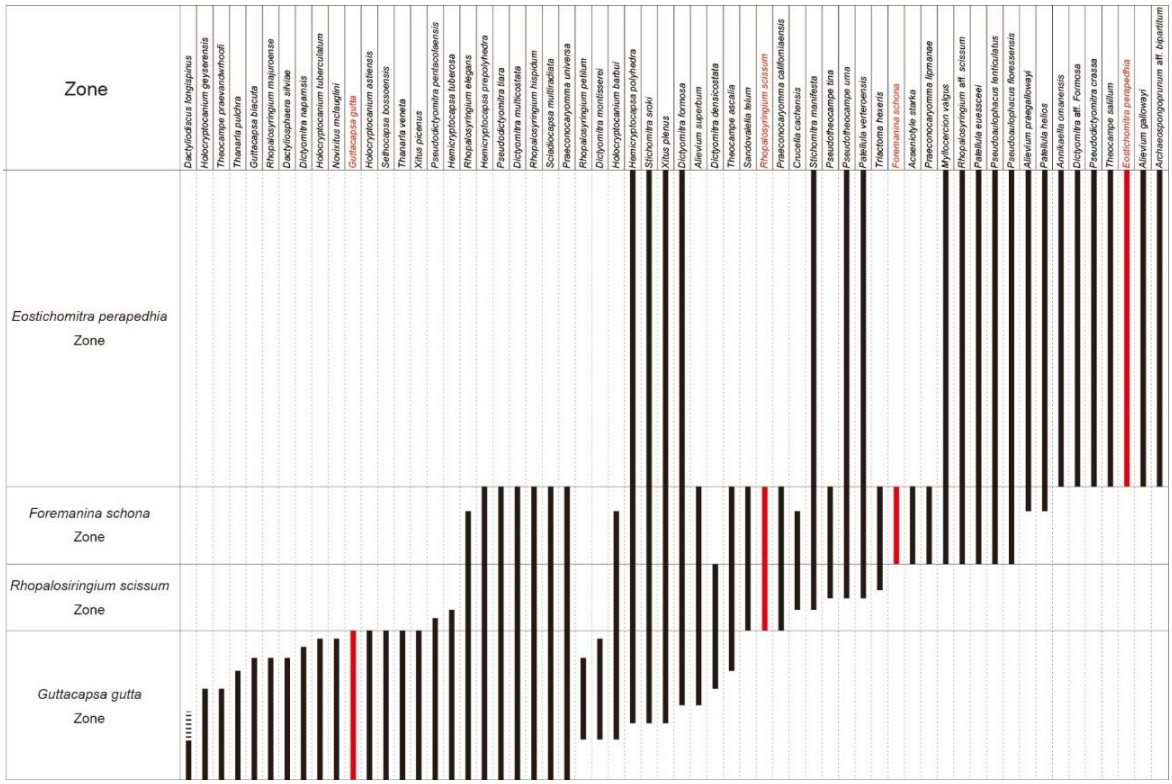

Fig. 22. The range of primary marker taxa and other species.

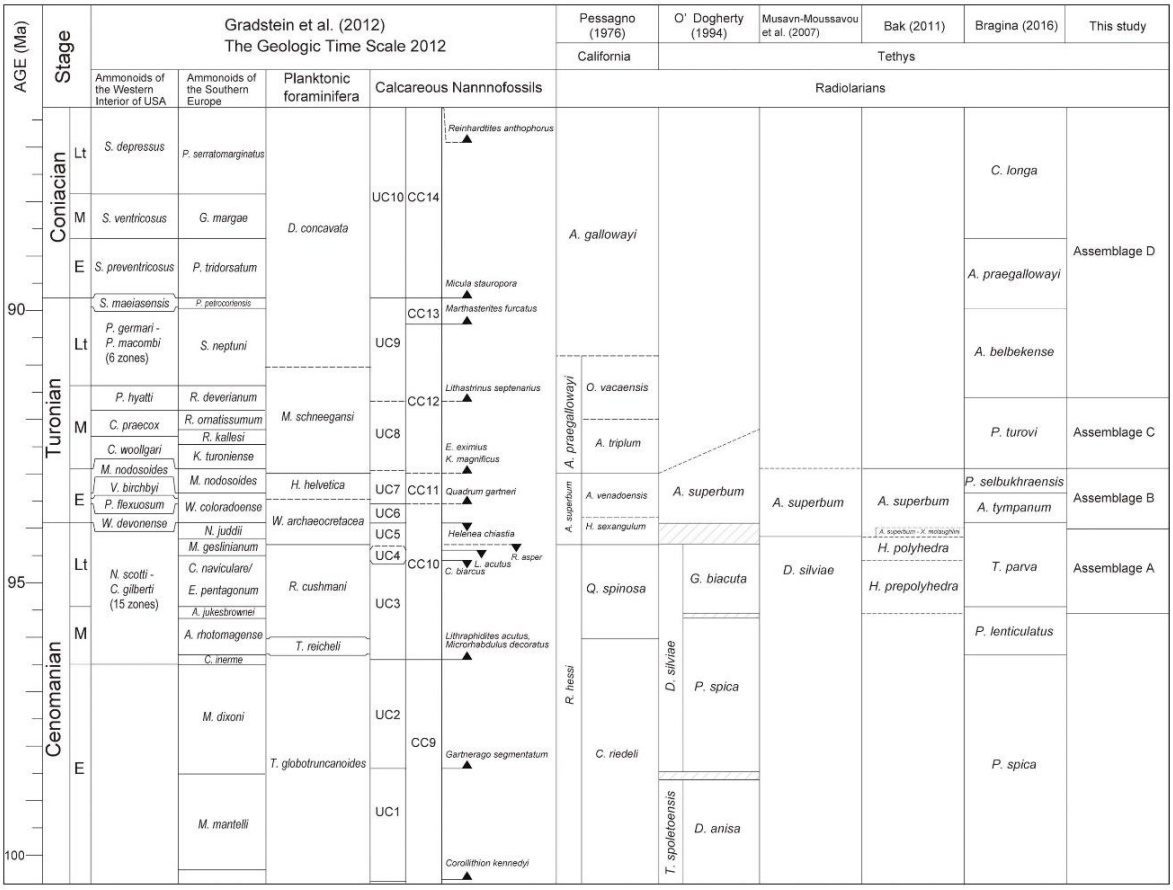

Fig. 23. Correlation of the Cenomanian to Coniacian radiolarian assemblages of the present study and biozones established in other areas (Pessagno, 1977; O'Dogherty, 1994; Musavu-Moussavou et al., 2007; Bąk, 2011; Bragina, 2016).

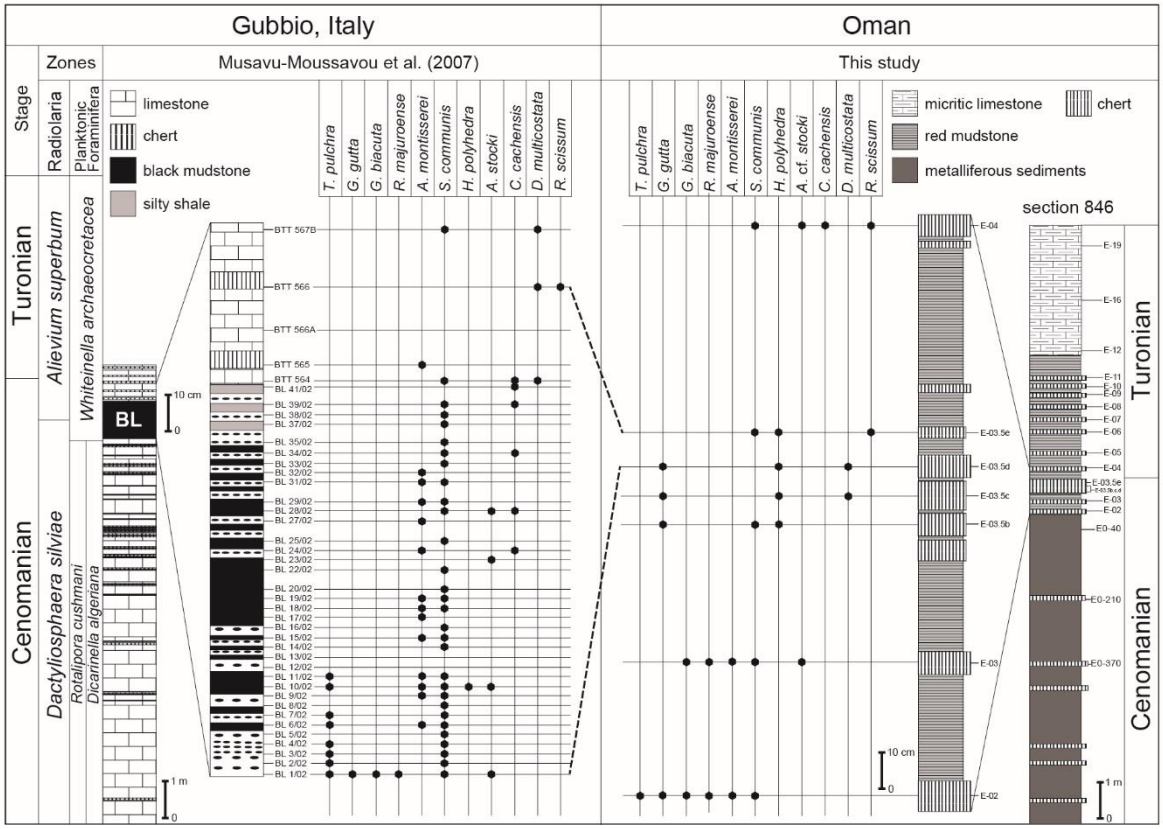

Fig. 24. Correlation of the upper Cenomanian and Turonian between section I and the strata across the Bonarelli level (BL) in Gubbio, Italy (Musavu-Moussavou et al., 2007), based on radiolarian occurrences. The position of the Cenomanian-Turonian boundary in the Gubbio section is after Tsikos et al. (2004), who placed the level at ca. 1 m above the stratigraphic top of the BL. Broken lines indicate correlations based on key biohorizons: the last occurrence of *Guttacapsa gutta* (Squinabol) and the first occurrence of *Rhopalosyringium scissum* O'Dogherty.

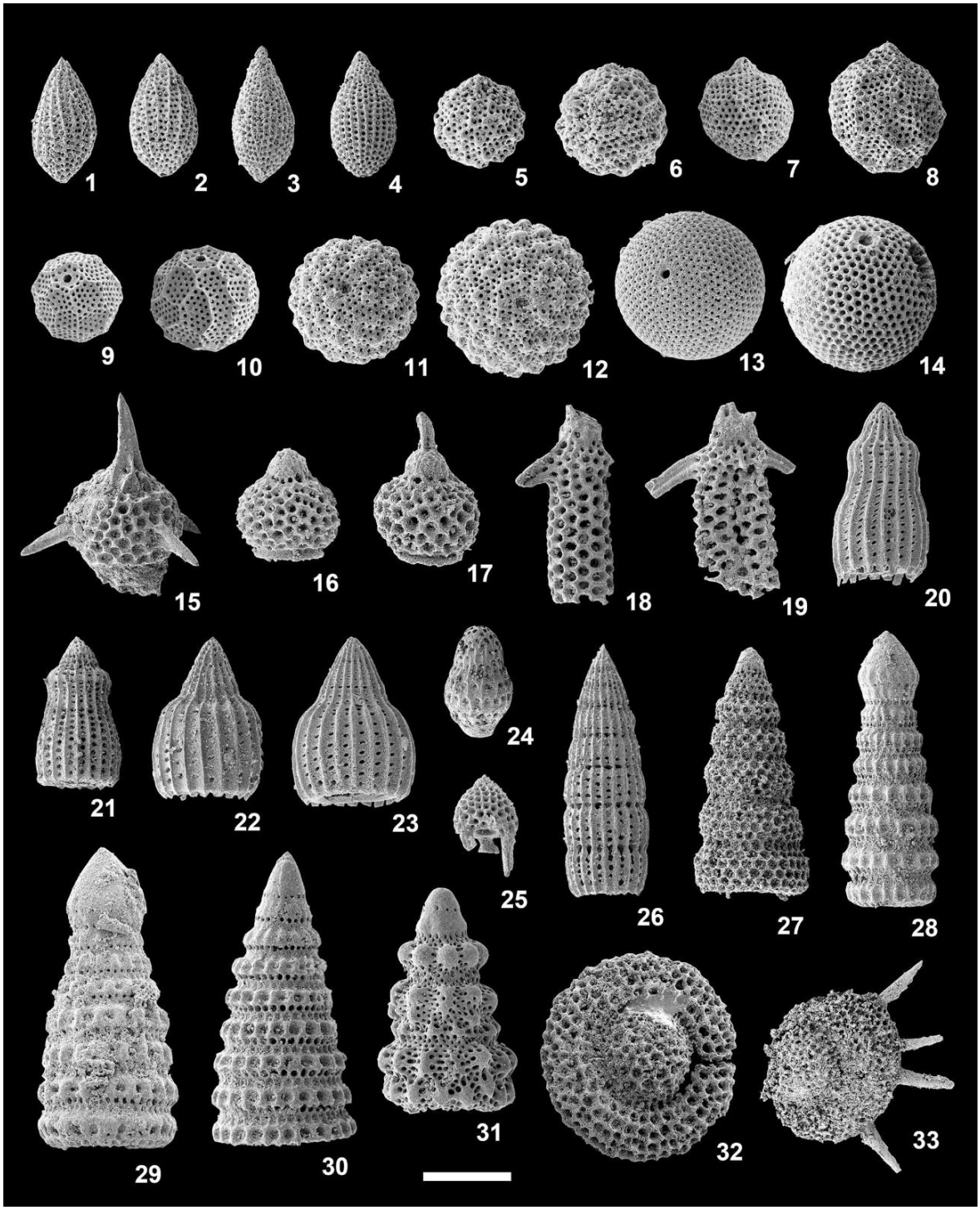

Fig 25. (1, 2) *Guttacapsa biacuta* (Squinabol), 1: E-03, 2: E0-370. (3, 4) *Guttacapsa gutta* (Squinabol), 3: E-02, 4: E-03.5b. (5, 6) *Hemicryptocapsa tuberosa* Dumitrica, 5: E-03.5b, 6: E0-210. (7, 8) *Hemicryptocapsa prepolyhedra* Dumitrica, 7: E-02, 8: E-03.5b. (9, 10) *Hemicryptocapsa polyhedra* Dumitrica, 9: C-08, 10: C-24. (11, 12) *Holocryptocanium tuberculatum* Dumitrica, 11: E-02, 12: E0-370. (13) *Holocryptocanium barbui*

Dumitrica, E0-40. (14) *Holocryptocanium* sp. A, E-03.5c. (15) *Rhopalosyringium elegans* (Squinabol), E-02. (16, 17) *Rhopalosyringium majuroense* Schaaf, 16: E0-370, 17: E-02. (18, 19) *Rhopalosyringium petilum* (Foreman), 18: E-02, 19: E0-40. (20, 21) *Thanarla veneta* (Squinabol), 20: E0-40, 21: E0-370. (22, 23) *Thanarla pulchra* (Squinabol), 22: E0-370, 23: E0-40. (24) *Pseudotheocampe* sp. A, E0-370. (25) *Myllocercion* sp., E0-40. (26) *Archaeodictyomitra montisserei* (Squinabol), E0-210. (27) *Stichomitra communis* Squinabol, E0-210. (28, 29) *Pseudodictyomitra pseudomacrocephala* (Squinabol), 28: E-03.5b, 29: C-28. (30) *Pseudodictyomitra tiara* (Holmes), E-03.5c. (31) *Novixitus mclaughlini* (Pessagno), E0-40. (32) *Dactyliosphaera silviae* Squinabol, E0-210. (33) *Dactyliodiscus longispinus* (Squinabol), E0-370. Scale bar = 100 μm.

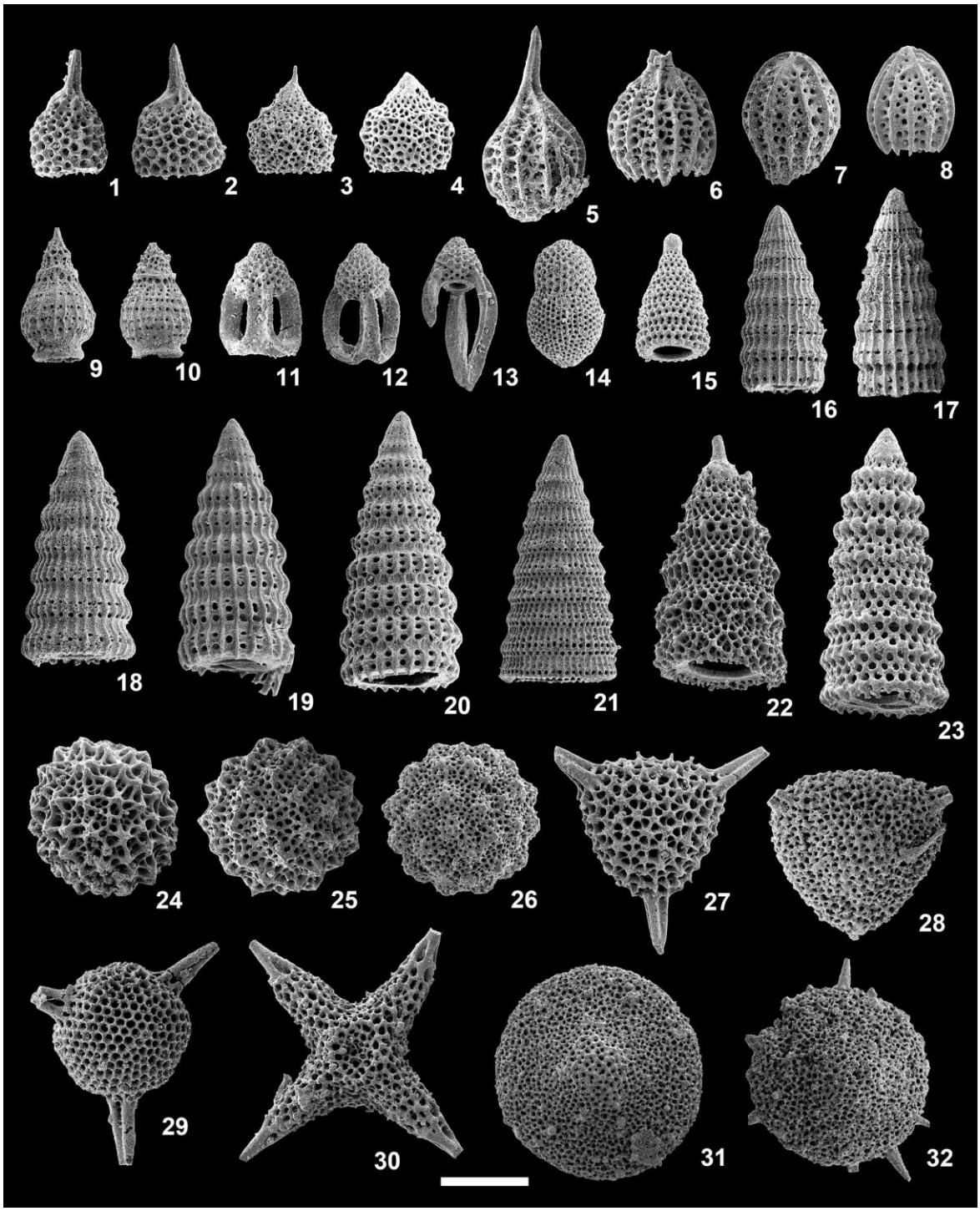

Fig. 26. (1, 2) *Rhopalosyringium hispidum* O'Dogherty, 1: E-06, 2: A-25. (3, 4) *Rhopalosyringium* sp. A, 3: a-15, 4: c-08. (5-8) *Rhopalosyringium scissum* O'Dogherty, 5: E-03.5e, 6: C-24, 7: A-15, 8: C-07. (9, 10) *Pseudotheocampe urna* (Foreman), 9: A-25, 10: C-24. (11, 12) *Annikaella omanensis* De Wever, Bourdillon-de Grissac, and Beurrier, 11: C-24, 12: A-25. (13) *Myllocercion valgus* (De Wever, Bourdillon-de Grissac, and Beurrier), C-24. (14)

Diacanthocapsa ovoidea Dumitrica, A-25. (15) *Amphipternis* sp. cf. *A. stocki* (Campbell and Clark), C-14. (16, 17) *Dictyomitra multicostata* Zittel, 16: A-13, 17: E-03.5c. (18, 19) *Dictyomitra formosa* Squinabol, 18: A-13, 19: E-12. (20) *Pseudodictyomitra* sp. A, A-11. (21) *Pseudodictyomitra* sp. B, A-11. (22) *Eostichomitra* sp. A, C-14. (23) *Foremanina schona* Empson-Morin, C-07. (24) *Praeconocaryomma californiaensis* Pessagno, C-07. (25) *Praeconocaryomma universa* Pessagno, C-24. (26) *Praeconocaryomma lipmanae* Pessagno, C-19. (27) *Alievium superbum* (Squinabol), A-11. (28) *Pseudoaulophacus putahensis* Pessagno, A-19. (29) *Triactoma hexeris* O'Dogherty, A-15. (30) *Crucella cachensis* Pessagno, C-24. (31) *Patellula verteroensis* (Pessagno), C-24. (32) *Patellula helios* (Squinabol), A-19. Scale bar = 100 μm.

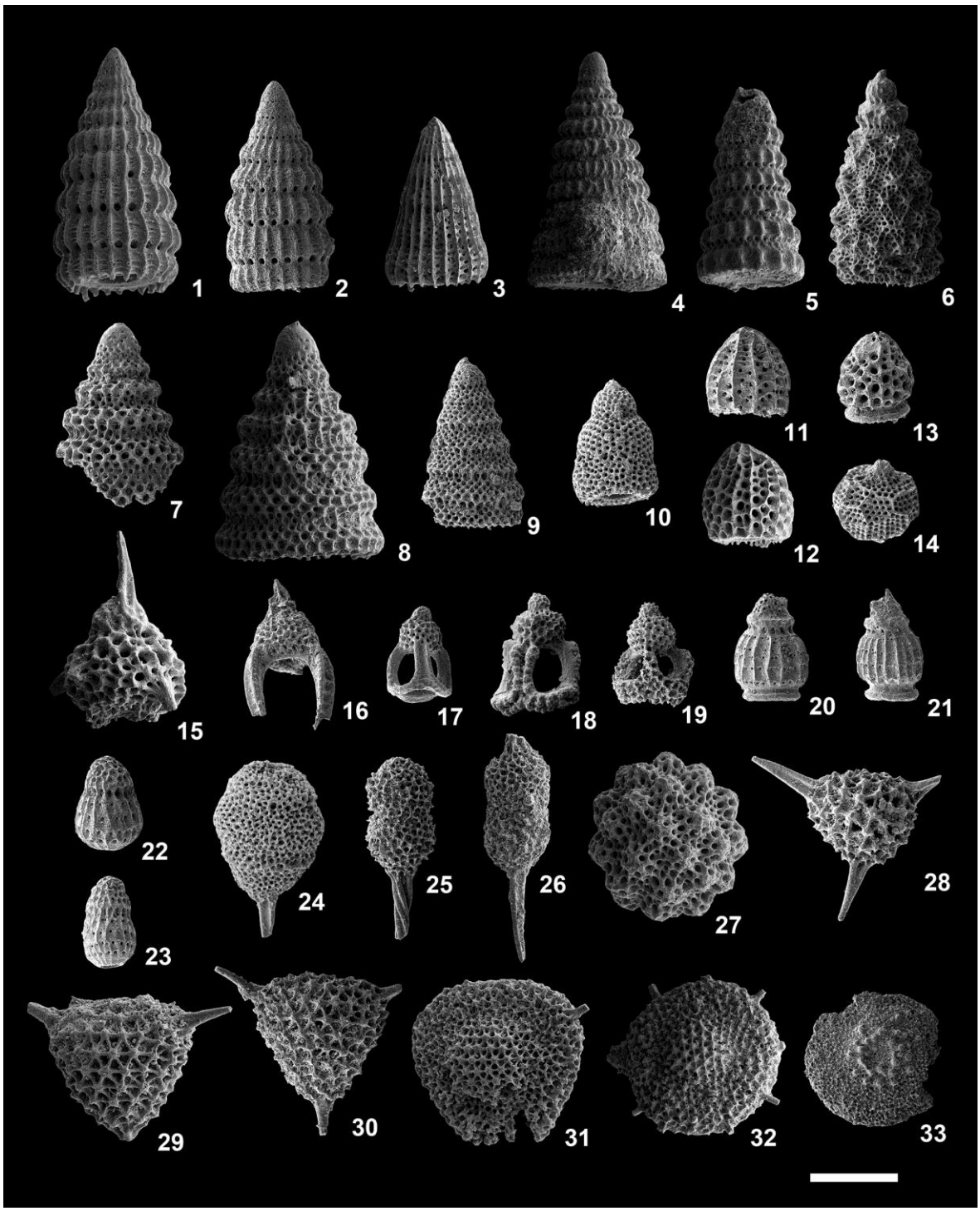

Fig. 27. (1, 2) *Dictyomitra* aff. *formosa* (Squinabol). (3) *Archaeodictyomitra* sp. A. (4) *Pseudodictyomitra crassa* Bragina. (5) *Pseudodictyomitra* sp. C. (6) *Xitus plenus* Pessagno. (7, 8) *Eostichomitra perapedhia* (Bragina). (9) *Eostichomitra* sp. (10) *Stichomitra manifesta* Foreman. (11) *Rhopalosyringium* aff. *scissum* O'Dogherty. (12) *Rhopalosyringium* sp. B. (13) *Rhopalosyringium* sp. C. (14) *Hemicryptocapsa polyhedra* Dumitrica. (15)

Rhopalosyringium aff. *elegans* (Squinabol). (16) *Myllocercion valgus* (De Wever, Bourdillon-de Grissac, and Beurrier). (17, 18) *Annikaella omanensis* De Wever, Bourdillon-de Grissac, and Beurrier. (19) *Annikaella* sp. A. (20, 21) *Pseudotheocampe urna* Foreman. (22, 23) *Theocampe salillum* Foreman. (24) *Archaeospongoprunum* sp. A. (25, 26) *Archaeospongoprunum* aff. *bipartitum* Pessagno. (27) *Praeconocaryomma* sp. A. (28) *Alievium praegallowayi* Pessagno. (29, 30) *Alievium gallowayi* Pessagno. (31) *Pseudoaulophacus floresensis* Pessagno. (32) *Pseudoaulophacus lenticulatus* (White). (33) *Patellula euessceei* Empson-Morin. All specimens were obtained from sample 472-05. Scale bar = 100 μm.

7. Discussion

7. 1. Depositional setting inferred from geochemical data of sedimentary rocks

All of the rocks in the siliceous succession, excluding the metalliferous sediments, red mudstone, and micritic limestone, have an SiO_2 content exceeding 85%, being consistent with geochemical data published for chert (Adachi et al., 1986; Yamamoto, 1987). The siliceous rocks contain abundant radiolarian fossils and suggest that high SiO_2 contents are mostly originated from biogenic silica (Hori et al., 2007). The SiO_2 content of the red mudstone (mean value of 87.5%) is higher than that of NASC (Gromet et al., 1984). Al_2O_3 and TiO_2 contents within sedimentary rocks are supplied from terrigenous material such as clay minerals, and are insensitive to the effects of diagenesis (Tada and Iijima, 1992; Murray, 1994). The occurrence of Rb, Zr, Nb, and Th is also indicative of a supply of terrestrial detritus (Jones and Manning, 1994; Hori et al., 2007). In the red mudstone, chert, and micritic limestone analyzed in this study, the contents of Al_2O_3 and Zr are relatively low, and the contents of TiO_2, K_2O, Rb and Th are also relatively low (Fig. 14, Tables 1 and 2).

Murray (1994) proposed a discrimination diagram for the depositional environment of chert, based on Al_2O_3, Fe_2O_3, TiO_2, La_n, and Ce_n. The rocks of the Suhaylah and Zabyat formations ranges from the ridge to pelagic environments (Figs. 28 and 29). In particular, metalliferous sediments and chert intercalated with metalliferous sediments plot within the ridge field, whereas the other sediments plots within the pelagic field in the $Al_2O_3/(Al_2O_3+Fe_2O_3)$ versus Fe_2O_3/TiO_2, diagram. These findings suggest that the Suhaylah and Zabyat formations are not influenced by inputs of terrigenous materials.

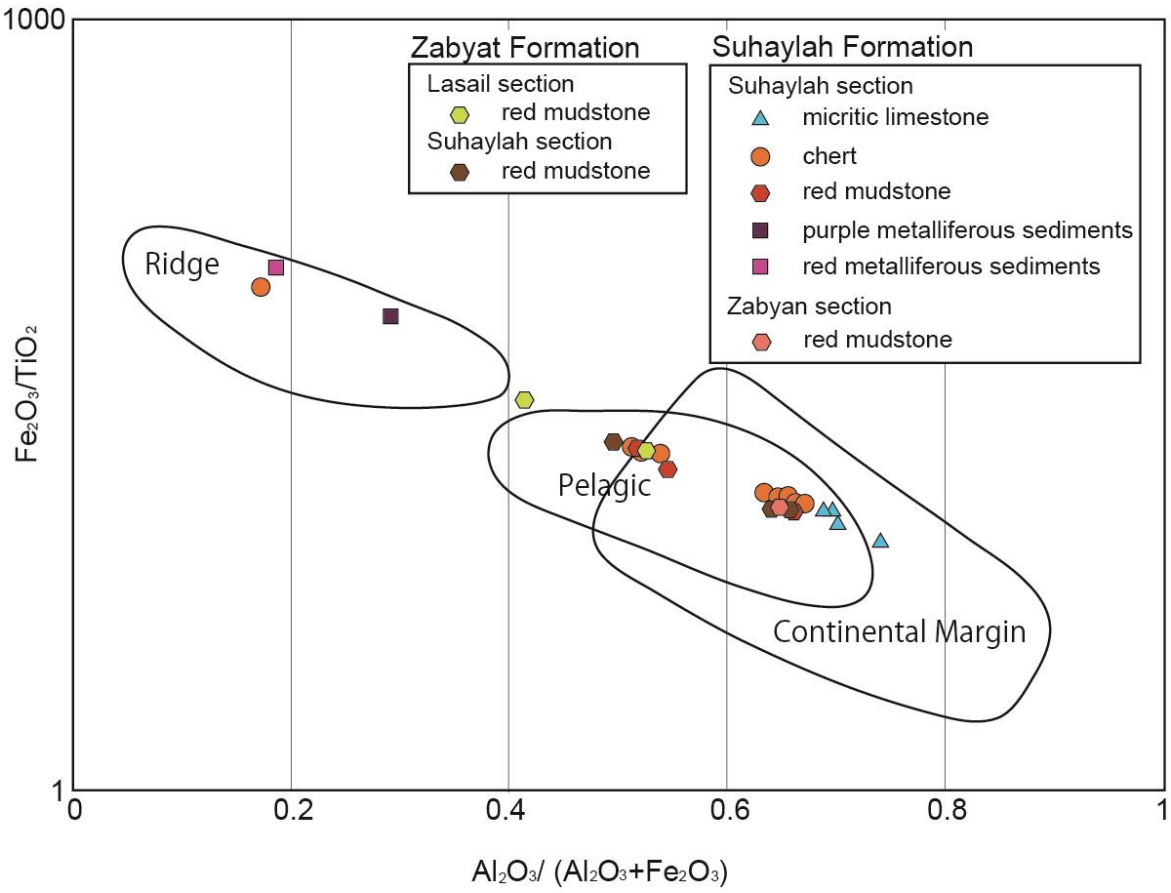

Fig. 28. Plots of $Al_2O_3/(Al_2O_3+Fe_2O_3)$ versus Fe_2O_3/TiO_2 showing data for the Suhaylah and Zabyat formations. The fields of ridge, pelagic, and continental margin are from Murray (1994).

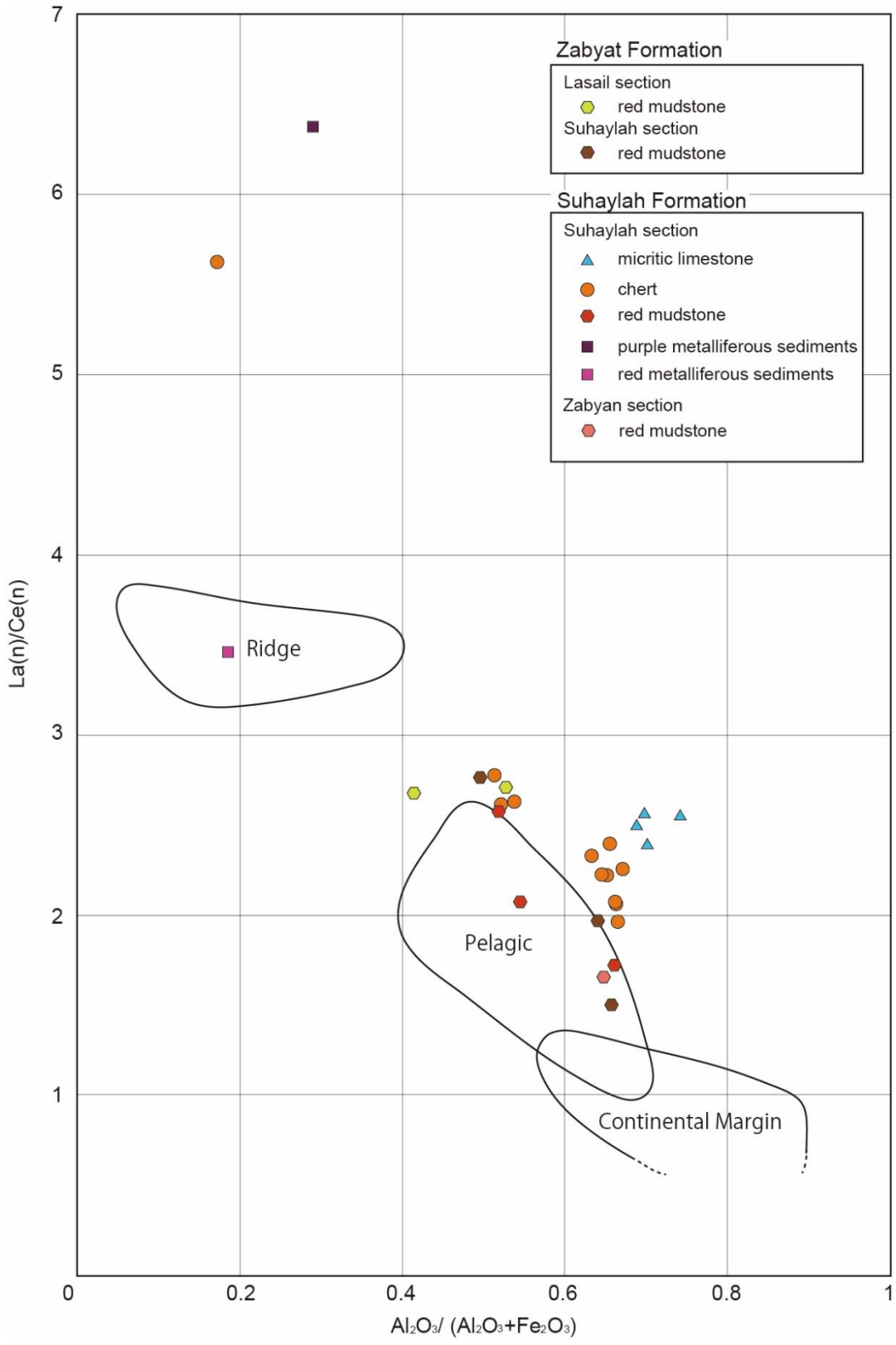

Fig. 29. Plots of Al2O3/(Al_2O_3+Fe_2O_3) versus Lan/Cen showing data for the Suhaylah and Zabyat formations. The fields of ridge, pelagic, and continental margin are from Murray (1994).

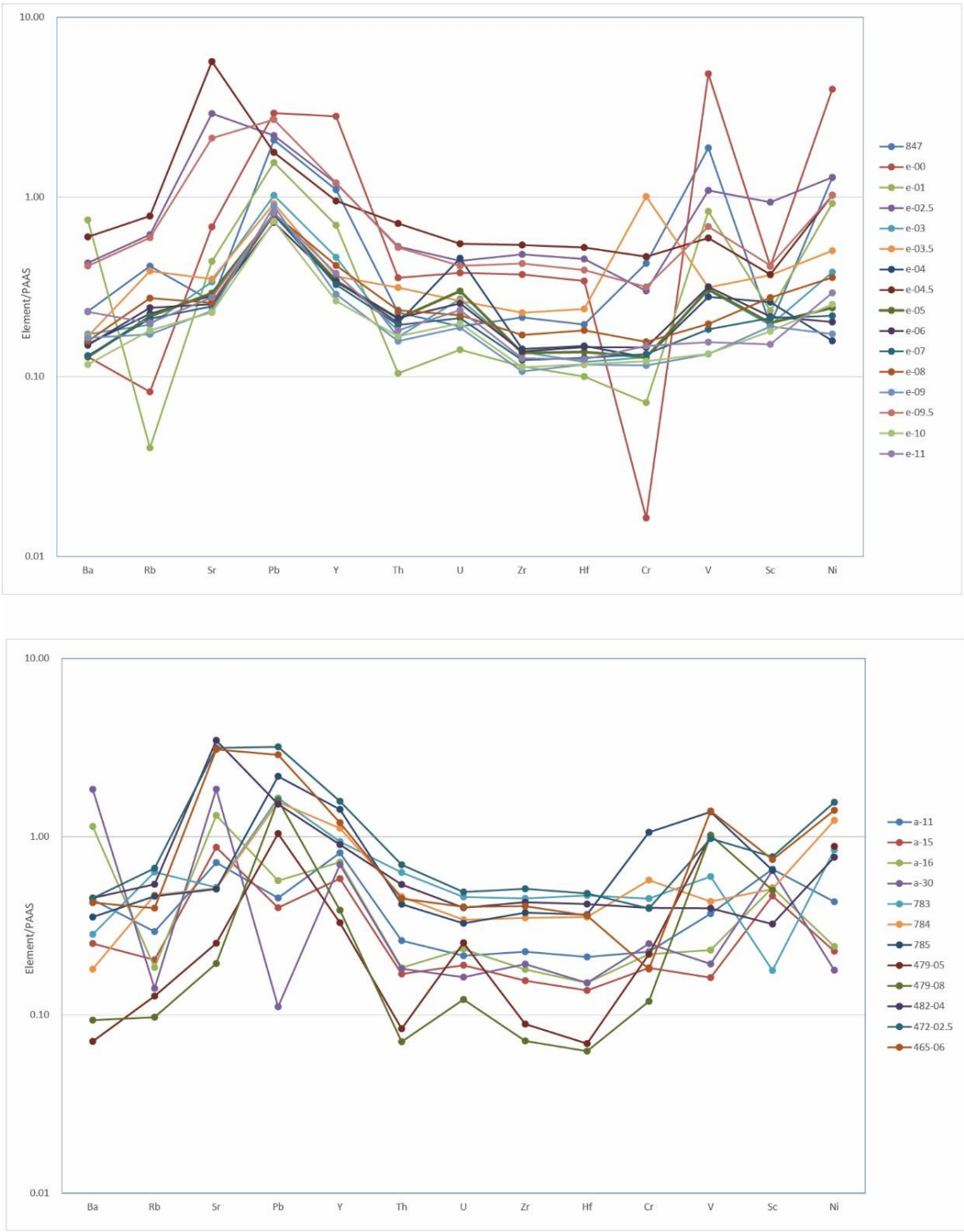

Fig. 30. Mean trace element compositions normalized against Post-Archean Australian Shale (Taylor and McLennan; 1985; McLennan, 1989).

7. 2. Revision of the biostratigraphic age of the Suhaylah and Zabyat formations

Until now, the main evidence for the age of the Suhaylah and Zabyat formations were the radiolarian faunas reported by Tippit et al. (1981) from the Suhaylah Formation. Herein we examined this fauna based on the current biostratigraphic scheme and determine the age of the formations based on our new radiolarian data.

Tippit et al. (1981) reported the following species from metalliferous sediments (sample 173) overlying the Geotimes Unit (V1 lava) in a location near Suhaylah (exact position not provided) in our mapped area (Fig. 2): *Quinquecapsularia spinosa* Pessagno, *Pseudodictyomitra pseudomacrocephala* (Squinabol), *Thanarla pulchra* (Squinabol), *Thanarla veneta* (Squinabol), *Hemicryptocapsa prepolyhedra* Dumitrica, *Holocryptocanium tuberculatum* Dumitrica, and *Holocryptocanium geysersensis* Pessagno. Based on the occurrences of these species, they assigned the sediments to the early Cenomanian. From micritic limestone underlain by metalliferous sediments and red radiolarian mudstone, *Hemicryptocapsa polyhedra* Dumitrica, *Crucella cachensis* Pessagno, *Praeconocaryomma universa* Pessagno, *Dictyomitra formosa* Squinabol, *Dictyomitra duodecimcostata* (Squinabol), and *Archaeospongoprunum rumseyense* Pessagno were recovered. The authors indicated the age of this fauna as Coniacian to Santonian. In addition, Tippit et al. (1981) noted the occurrence of planktonic foraminifera that are assigned to the '*Marginotruncana helvetica* Assemblage Zone (*Marginotruncana sigali* Subzone)' of Pessagno (1969) from the upper part of the red radiolarian mudstone (corresponding to the upper part of Unit SS2 in this study), indicating the early Turonian, although species names and photographs were not provided in their study. Based on their data, the age of the Suhaylah Formation ranges from the early Cenomanian, through the early Turonian, to the Coniacian-Santonian.

In the present study, *G. gutta* Zone included almost all the species reported in sample 173 of Tippit et al. (1981). According to O'Dogherty (1994), these species have Albian to Turonian age ranges, and the co-occurrence of *T. pulchra*, *T. veneta*, and *H. prepolyhedra* indicates UAs 17 to 19 (middle to late Cenomanian). As mentioned above, our biostratigraphic result for *G. gutta* Zone indicates that the metalliferous sediments corresponding to the basal part of the Suhaylah Formation can be assigned a middle to late Cenomanian age (Figs. 31 and 32); in other words, the chronological reinterpretation of the previously reported fauna is consistent with the results of our reexamination of the biostratigraphy. Tippit et al. (1981) described the red radiolarian mudstone as yielding early Turonian foraminifera; however, it is difficult to reexamine this foraminiferal age because no photographs of fossils were provided. This lithology corresponds to Unit SS2 in our lithostratigraphic subdivision, which has an age range of latest Cenomanian to early Turonian across the possible C-T boundary. This finding is also consistent with the description of Tippit et al. (1981).

The fauna from micritic limestone reported by Tippit et al. (1981), which was assigned a Coniacian-Santonian age, has some species in common with our *F. schona* Zone, but typical index species of Santonian age are not present, such as *Dictyomitra koslovae* Foreman and *Pseudoaulophacus floresensis* Pessagno (e.g., Hollis and Kimura, 2001). Based on the age determination of *F. schona* Zone, the age of the micritic limestone is within the Turonian (Figs. 31 and 32). In addition, both the ages of the uppermost parts of the Suhaylah Formation and the top of the Zabyat Formation can be assigned to Coniacian, based on the age determination of *E. perapedhia* Zone (Figs. 31 and 32).

In conclusion, the biostratigraphy of the studied sections indicates that the Suhaylah and Zabyat formations ranges in age from middle-late Cenomanian to Coniacian, on the basis of the ages assigned to the four radiolarian assemblages in the sections. According to Gradstein et al. (2012), the numerical ages of the base of the middle Cenomanian and the top of the

Coniacian are 96.5 Ma and 86.3 Ma, respectively. Therefore, the biostratigraphic results indicate that the time interval represented by the Suhaylah and Zabyat formations is a maximum of approximately 10 Myr.

7. 3. Significance for age constraints on the V1 lavas

For ophiolite studies, it is critical to understand the formation of the oceanic crustal features of ophiolites and their emplacement process along the time-dimension established from radiometric and biostratigraphic ages (e.g., Hacker and Gnos, 1997). From this point of view, the maximum age of the metalliferous and pelagic sediments immediately above the V1 lava provides information about the approximate termination age of the mid-ocean-ridge magmatism; this can provide age constraints on the changes in tectonic setting indicated by different basaltic lava units, each of which has its own geochemical characteristics.

The comparison between the U–Pb isotopic age of crustal rocks (trondhjemites) within the ophiolite and the biostratigraphic age of the overlying sediments (Tippit et al., 1981) was first discussed by Tilton et al. (1981). Both ages were in accordance with each other at that time, although the precision of the age data could be improved. Tippit et al. (1981) concluded that the volcanic activity of a ridge-axis, represented by the Geotimes Unit (V1 lava), occurred in the early Cenomanian; however, we revised the age of the metalliferous sediments to middle-late Cenomanian, meaning the estimated maximum possible age is 96.5 Ma. After the study of Tilton et al. (1981), the chronology of trondhjemites related to the ridge magmatism was investigated by Warren et al. (2005), indicating an age of ca. 95 Ma; however, these younger ages were suggested to reflect post-crystallization Pb-loss (Rioux et al., 2012; Searle et al., 2015).

High-precision U–Pb zircon dating has been conducted by Rioux et al. (2012, 2013, 2014, 2016) on gabbros, tonalites, and trondhjemites exposed (from south to north) in the Wadi Tayin, Samail, Rustaq, and Haylayn areas,

south and west of Muscat, and the Fizh area, northwest of Sohar. According to Rioux et al. (2013, 2014), the rocks fall into two groups in terms of their structural positions, dates, and isotopic composition: the older group, dated at ca. 96.0–95.5 Ma (middle Cenomanian), is attributed to ridge magmatism, whereas the younger group (ca. 95.5–95.0 Ma) is related to post-ridge magmatism (Fig. 33). The V1 lava is interpreted as the extrusive component of the former group (Lippard et al., 1986; Ernewein et al., 1988; Rioux et al., 2013). Although there is generally some difficulty in comparing radiometric and biostratigraphic ages for the Mesozoic, our detailed radiolarian study allows a substantial discussion, as follows. We estimate 96.5–93.9 Ma (middle-late Cenomanian) as the maximum possible age of the metalliferous sediments, based on the age of *G. gutta* Zone (Figs. 31 and 32). This estimated age overlaps with the U–Pb zircon age of gabbroic crustal rocks formed by ridge magmatism (ca. 96.0–95.5 Ma: Rioux et al., 2013, 2014, 2016). In addition, the base of strata yielding *R. scissum* Zone within Unit 2 lies across the possible C-T boundary (Fig. 24). It is worth of note that the C-T boundary is well constrained by $^{40}Ar/^{39}Ar$ ages from bentonites as 93.9 Ma (Gradstein et al., 2012). All that can be said with certainty is that the V1 lava generated by ridge magmatism has an age not younger than 95.5 Ma and therefore there had been sufficient time for the continuous deposition of a 10-m thickness of metalliferous and pelagic sediments upon the lava. Thus, we conclude that the radiolarian age of the overlying sediments on the V1 lava is in good agreement with the U–Pb zircon dates of the ophiolite crusts that formed by ridge magmatism, and considering all the data we could indicate a late Cenomanian age for *G. gutta* Zone.

7. 4. Significance for age constraints on the V2 lavas

The maximum age of the metalliferous and pelagic sediments immediately above the V2 lava provides information about the approximate termination age of the intra-oceanic arc-like volcanism. The sediments on the V2 lava of

the Zabyan, Lasail, and Hilti exposures can be correlated with the middle to late Cenomanian based on *G. gutta* Zone (Figs. 31 and 32). The radiolarian ages of the V1 lava obtained from this study are middle Cenomanian-late Cenomanian. These findings reveal that the activity from the V1 to UV2 lavas was terminated in late Cenomanian.

High-precision U–Pb zircon dating has been conducted by Rioux et al. (2016) on plutonic rocks related to V2 lava exposed (from south to north) in the Wadi Tayin, Samail, Rustaq, and Haylayn areas, south and west of Muscat, and the Fizh area, northwest of Sohar. The high-precision U–Pb zircon ages was reported as 95.5 to 95 Ma for crustal rocks formed by post-ridge magmatisms (Rioux et al., 2016). The radiolarian ages mentioned above are consistent with this age. Therefore, these age constraints imply that the change of tectonic setting progressed rapidly in a short period of middle–late Cenomanian.

7. 5. Significance for age constraints on the V3 lavas

The micritic limestone of 490 sections where the thickest pelagic sediments are developed in Hilti exposure is correlated to the *F. schona* Zone, and the red mudstone just beneath the V3 lava is correlated to the *E. perapedhia* Zone. Therefore it is concluded that the V3 lava erupted from late Turonian to Coniacian.

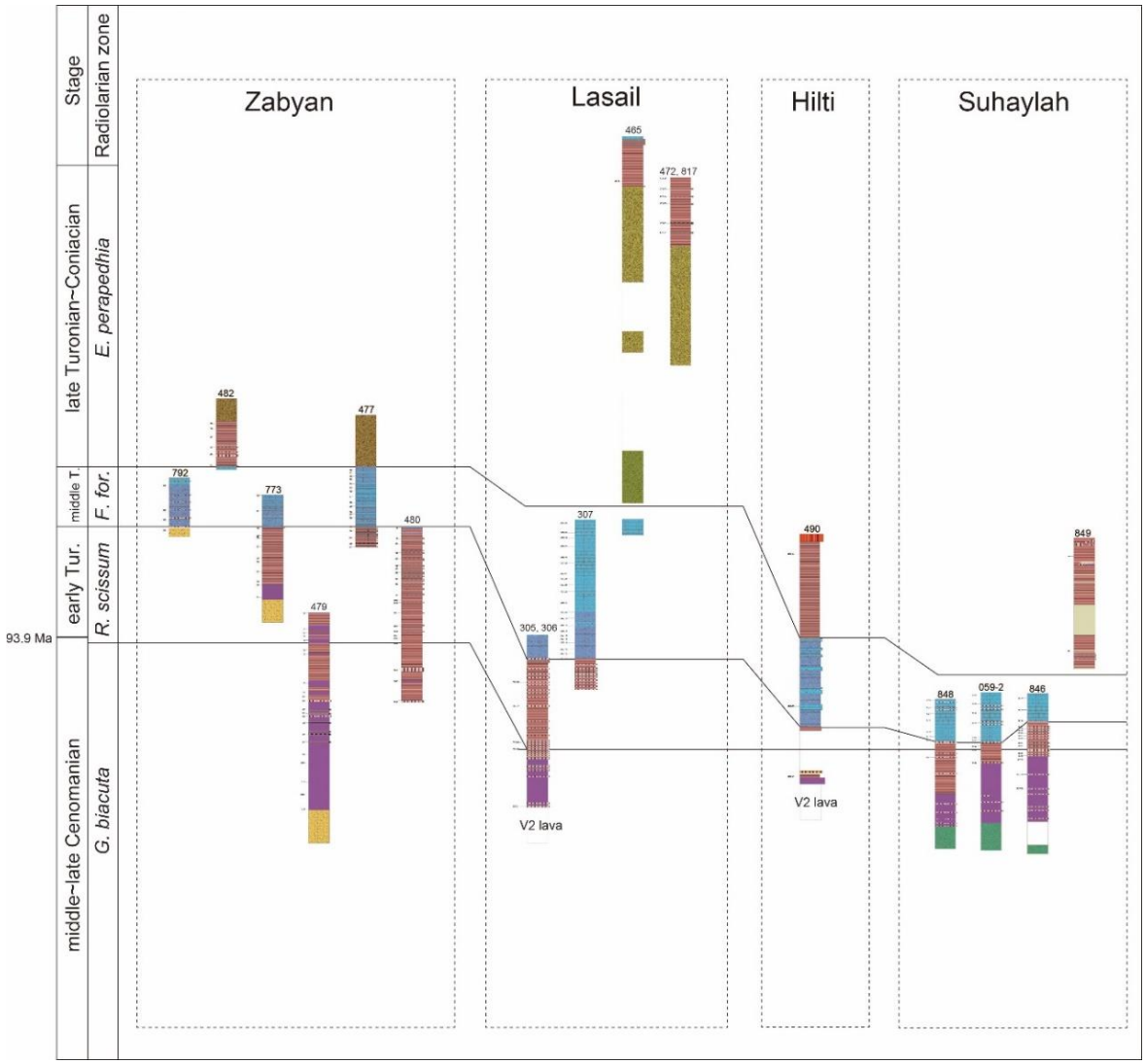

Fig. 31. Correlation among the study sections by based on the radiolarian zones.

7. 6. Development process of pelagic sediments

From the obtained data, the development process of pelagic sediments within the Oman Ophiolite is discussed in this section. The V1 lava erupted at 96 ~ 96.5 Ma in the mid-ocean ride, and metalliferous sediments deposited on the V1 lava due to the hydrothermal activity of the V1 lava. The radiolarian age of the metalliferous sediments underlain by the V1 lava is the middle Cenomanian-late Cenomanian. The V1 lava erupted in pelagic realm based on the geochemical composition of the sediments above the V1 lava (Figs. 28 and 29). Subsequently, the hydrothermal activity gradually weakened and the metalliferous sediments on the V1 lava gradually changed to red mudstone in early Turonian. Then, the hydrothermal activity stopped completely, and micritic limestone deposited in the pelagic realm in middle Turonian. The sediments on the V1 lava are not micritic limestone; carbonates could be dissolved by hydrothermal activity (Fleet and Robertson 1980). The micritic limestone changed to red mudstone in late Turonian to Coniacian, indicating that biological productivity of calcareous nannoplanktons of the ocean surface layer may decrease and the CCD becomes shallower. After that, ophiolite debris of the Zabyat Formation covered red mudstone. The red mudstone of the Zabyat Formation is also considered to have deposited in the pelagic realm based on the geochemical composition (Figs. 28 and 29). In Suhaylah exposure, the Zabyat Formation is dominated by fine grained mudstone and pebbles of ophiolite debris are minor. It is concordant with the argument by Tippit et al. (1981) that the V2 lava is also not distributed in Suhaylah exposure because the sediments of this exposure deposited in the rise around an ocean ridge.

After eruption of the V1 lava, the tectonic setting changed in a very short period less than approximately one million years and the V2 lava erupted by intra-oceanic arc-like volcanism. Based on the geochemical composition of sediments on the V2 lavas, the V2 lava erupted in the pelagic realm (Figs. 28 and 29). In addition, based on the comparison with the geochemical

composition of PAAS (post-Archean Australian shale: Taylor and Mclennan, 1985), incompatible elements such as Zr are lower than PAAS (Fig. 30). Therefore, it is considered that a mature island arc did not develop at the time of V2 lava eruption. After the eruption of the V2 lava, a stratigraphic sequence consisting of metalliferous sediment, red mudstone, micritic limestone, red mudstone like the sediments on the V1 lava was formed, and then the conglomerate of the Zabyat Formation covered it. In the Hilti exposure, the red mudstone on the micritic limestone was covered by the V3 lava rather than the Zabyat Formation. This red mudstone is correlated with the *E. perapedhi*a Zone, so the V3 lava erupted at least late Turonian-Coniacian by intra-plate volcanism.

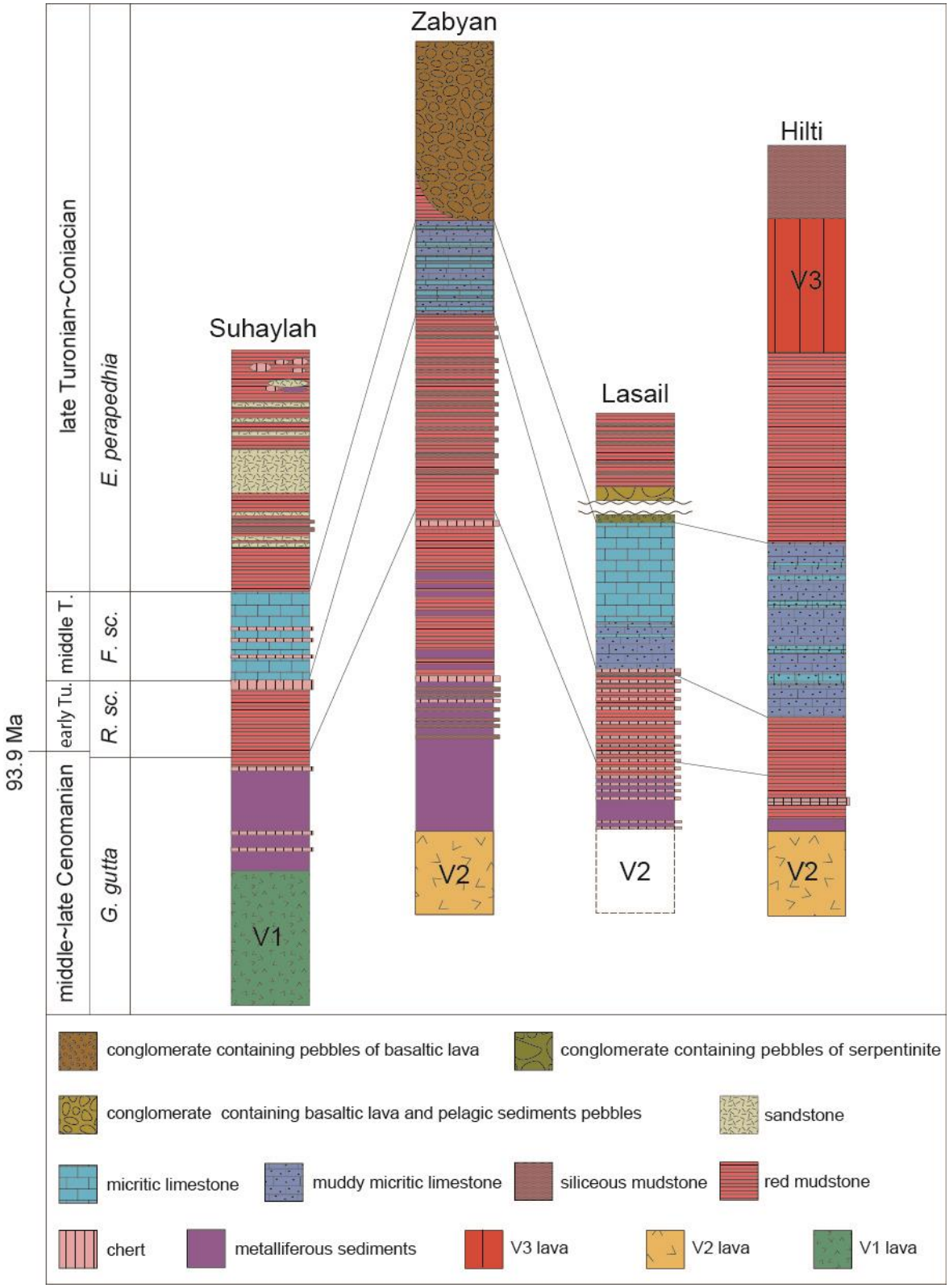

Fig. 32. Radiolarian age of pelagic sediments in Suhaylah, Zabyan, Lasail and Hilti exposure and the ages of extrusive lavas.

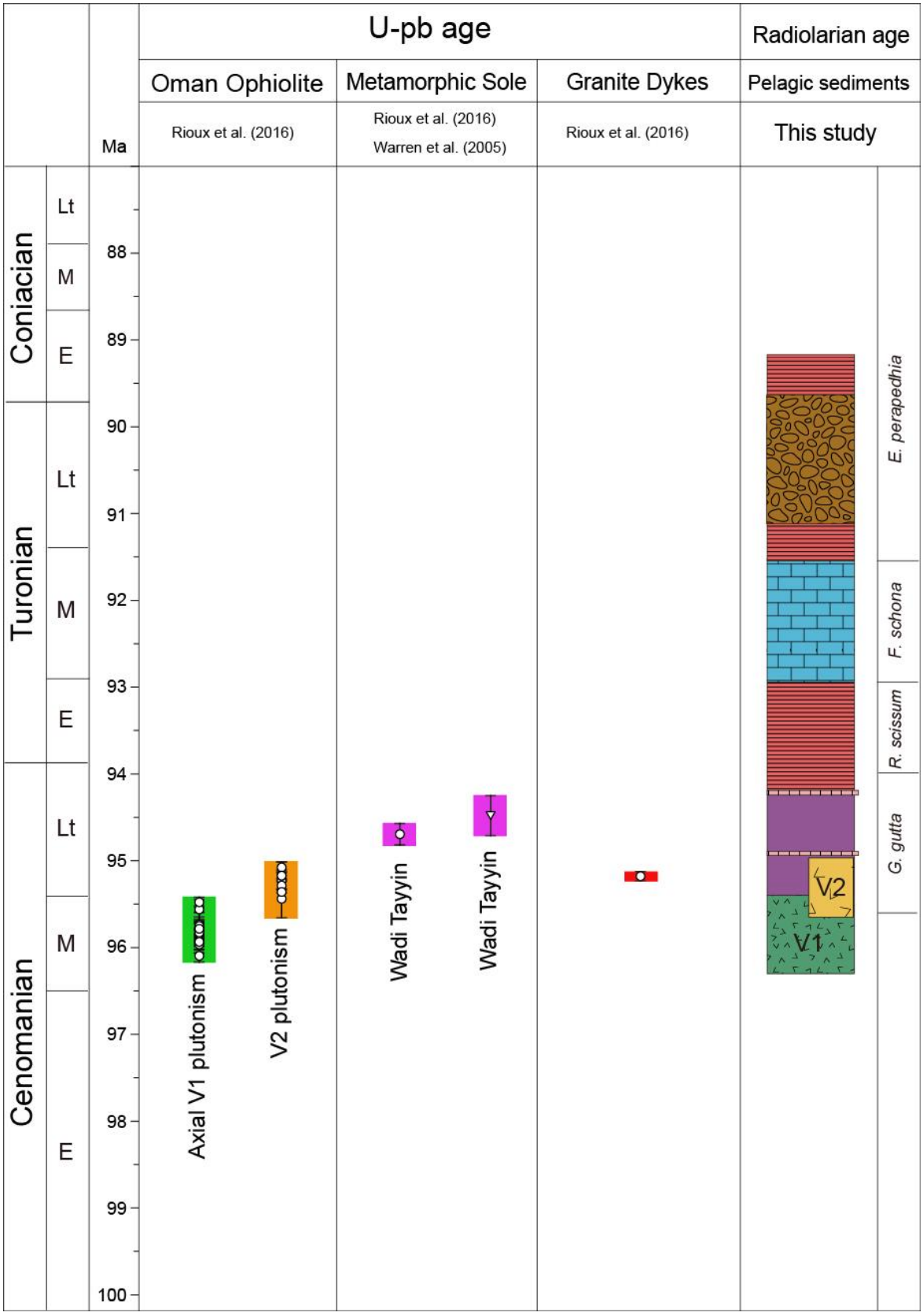

Fig. 33. Comparison between the radiolarian age and U-Pb age of zircons.

7. 7. Environmental change across the Cenomanian/Turonian boundary: a review

The oceanic anoxic event (OAE) characterized by deposition of black shale can be said to be one expression of extremely high temperate environment. The Oceanic anoxic events have occurred a total of 6 times in Cretaceous (OAE1a, OAE1b, OAE1c, OAE1d, OAE2, and OAE3). In the Tethyan region, most of the Atlantic region, and a part of the Pacific, black shale was deposited. In addition, it is characterized by a positive excursion of the carbon isotope ratio. These OAEs have a great influence on marine organisms and have exterminated invertebrates such as planktonic foraminifera, radiolarians, cephalopods (e.g., Elder, 1989; Leckie et al., 2003; Erbacher et al., 1996; Erbacher and Thurow, 1997). Regarding the mechanism of the OAEs, several ideas have been proposed: essential elements were brought to an ocean surface layer by hydrothermal activity of LIPs, and then primary producers increased and the oxygen minimal layer was expanded (e.g., Larson and Erba, 1999; Snow et al. , 2005); global warming and high sea level due to the activities of LIPs increased nutrients from the continental region, and then primary ocean producers increased (e.g., Larso and Erba. 1999; Leckie et al., 2002; Ozaki and Tajika, 2013). Tajika and Yamanaka (2003) studied the behavior of ocean circulation and the conditions under OAE using vertical one-dimensional and two-dimensional marine circulation models. Tajika and Yamanaka (2003) have shown two pattern of ocean circulation when the ocean circulation becomes active: one is that the middle layer becomes anoxic, and the other is that the deep water becomes anoxic by stagnant ocean circulation.

Among the OAEs, OAE2, occurred at the middle of the Cretaceous (Cenomanian/Turonian), is known as the largest scale OAE. Many paleontological and geochemical studies have been conducted in the Tethyan, Atlantic, and Pacific regions. The extinction rate during the OAE2 have been estimated as 8% at the family level, 26% at the genus level, and 33-55% at

the species level (Sepkoski 1989, 1996). For radiolarians, researches have been actively conducted on the Cenomanian/Turonian boundary where OAE2 occurred (e.g. Erbacher, 1994; O'Dogherty, 1994; Erbacher and Thurow, 1997; O'Dogherty and Guex, 2002; Musavu- Moussavou and Danelian; 2006; Musavu-Moussavou et al., 2007; Back 2011). With regard to the extinction of radiolarians at the OAE2, Erbacher and Thurow (1997) pointed out that 29 species of late Cenomanian species (58%) were extinct during OAE2 in the Tethyan region and 20 species (49%) were newly speciated after OAE2. According to Musavu-Moussavou et al., 2007, 54 species (40.6%) were extinct from the lower to middle parts of the Bonorelei Level, and 42 species (34.7%) were newly added in the early Turonian limestone covering black shale.

Various isotopic ratios have been measured in the OAE2 horizon of C/T boundary. In particular, the carbon isotopic ratio has been measured in various regions. The contrast between the Tethyan-Atlantic region and the Pacific region where black shale was not deposited has been discussed (e.g. Hasegawa and Saito, 1993; Hasegawa et al., 2013). Recently, studies on isotopic ratios of Pb and Os in sediments have been conducted extensively. According to Kuroda et al. (2007), the lead isotopic ratios (^{208}Pb, ^{206}Pb, and ^{204}Pb) of the black shale of the Bonarelli Level, which is the standard of the OAE2 in Italy, are similar to the composition range of Madagascar Flood Basalt Province and Caribbean Large Igneous Province, indicating the relationship between the OAE2 and LIPs. The osmium isotopic ratio ($^{187}Os/^{188}Os$) can detect the change in the balance between the weathering effect and the supply amount of hydrothermal activity from the mantle, and the relationship between the OAE2 and LIPs (Madagascar Flood Basalt Province and Caribbean Large Igneous Province). Turgeon and Creaser (2008) examined osmium isotope ratios in the Bonarelli Level and the OAE2 horizon of the Atlantic Demerara Rise. As a result, the osmium isotopic ratio has drastically decreased by several ten thousand years ahead of the

occurrence of the oceanic anoxic event. In addition, the weathering could be gradually prominent toward the end of OAE2.

7. 8. Redox conditions inferred from geochemical data

V, Cr, Co, Ni, Cu, Zn, Mo, Pb, and U are known to be redox-sensitive elements (Algeo and Maynard, 2004; Rimmer, 2004). These elements are typically enriched in anoxic sediments. In the present study, all analyzed samples are impoverish in V, Cr, Ni, Zn, and U (Fig. 17, Table 1).

Several indicators of redox conditions have been proposed in previous geochemical studies (Hatch and Leventhal, 1992; Jones and Manning, 1994; Rimmer, 2004). This study applies the Th/U ratio to understand the redox conditions of the environment in which the red mudstone and the chert were deposited. This ratio has been used as a proxy for the redox conditions of the depositional environment (Wignall and Twitchett, 1996; Kimura and Watanabe, 2001). Th is unaffected by redox conditions and is supplied from terrigenous material. In contrast, U is a redox-sensitive element found in organic matters.

Wignall and Twitchett (1996) proposed that Th/U ratios vary from 0 to 2 in anoxic environments, 2 to 7 in oxic environments, and are in excess of 7 in strongly oxidizing environments. According to this scheme, the red mudstone and the chert in the present study was deposited under oxic conditions.

The cerium anomaly (Ce/Ce*) in ocean sediments is controlled by several factors, including redox conditions (De Baar et al., 1985; Bellanca et al., 1997; Holser, 1997; Pattan et al., 2005), depositional setting (Matsumoto et al., 1988; Murray et al., 1990, 1991), sedimentation rate (Sholkovitz et al., 1994), and variation of the Ce content within the ocean (Thomson et al., 1984). Within the red mudstone and the chert analyzed in the present study, Ce/Ce* values show hardly changed, consistent with the obtained Th/U ratios as an indicator of redox conditions (Fig. 17). In the case of an anoxic ocean, seawater generally shows a positive anomaly due to the elution of Ce into

the ocean, whereas bottom sediment shows no such anomaly. In contrast, the sediment in an oxic ocean shows a positive anomaly due to the precipitation of Ce, and seawater is depleted in Ce (Holser, 1997). The Ce/Ce* values observed in the red mudstone and chert supports the trend of redox conditions inferred from TOC values and Th/U ratios. Together, these redox indicators suggest that they are constantly oxic conditions within the succession.

7. 9. Comparison with the occurrence patterns of radiolarians in the European Tethys Ocean

In the extinction interval (E-03, E-03.5b, E-03.5, and E-03.5d of Unit SS2: upper part of G. gutta Zone) in the Suhaylah Formation, *H. astiensis*, *C. conara*, spherical Nassellaria of the genera *Hemicryptocapsa* and *Holocryptocanium* are dramatically increased. *Hemicryptocapsa* and *Holocryptocanium* very rarely occur immediately after the extinction. On the contrary, many spherical Spumellaria such as *Praeconocaryomma* and *Acanthocircus* occur abundantly. In addition, in the extinction horizons of E-03, E-03.5b, E-03.5c, and E-03.5d, the genus *Rhopalosyringium* was gradually diversified, and *R. scissum* begins to be occurred in E-03.5e corresponded to after the end of the extinction. In E-03.5, *R. scissum* and *R. hispidum* dramatically increase. This trend continues to E-11 in the upper part of Unit SS2. *Eostichomitra* sp. and *Dictyomitra* sp. increases dramatically from E-03.5e, and this trend also continues until E-11 (Fig. 36).

Bak (2011) and Moussavou et al. (2007) have conducted detailed studies on the extinction at the C/T boundary of radiolarians. Therefore, the present study attempts to compare the occurrence pattern of Bak (2011) which clearly shows the abundance of radiolarians.

Bak (2011) conducted radiolarian biostratigraphy in Umbria-Marche basin in Italy and Outer Carpathian basins in Poland (Fig. 34). The Umbria-Marche Apennines is located in the center of the Apenninic chain and

consists of thrust and fold belts formed in Late Miocene. Cretaceous sediments of Umbria-Marche basin deposited on complex basins and swell topography along the continental margin of the Apulian block. Apulian block moved from North Africa to Northern Europe and was strongly influenced by pre-orogenic deformation (Marchegiani et al., 1999).

The basement of Umbria-Marche Apennines is the continent, pelagic sediments of Upper Jurassic to Lower Miocene covering the carbonate platform of Lower Jurassic from Triassic. The upper Cenomanian-Lower Turonian are subdivided into two lithostratigraphic units: the Scaglia Bianca Formation in the upper most Albian–lowest Turonian, and the Scaglia Rossa Formation in the earliest Turonian–early Lutetian. The Scaglia Bianca Formation consists mostly of limestones, with several intercalations of marlstones and shales. The limestones consist of calcareous nannoplankton and planktonic foraminiferal ooze deposited above the CCD, at depths between 1,500 and 2,500 m (Arthur & Premoli Silva, 1982; Kuhnt, 1990). The upper most member also consists of mostly limestone with common nodules and lenses of dark-grey to black chert. The Bonarelli Level (OAE2 horizon, 1 m thick) occurs near the top of the Scaglia Bianca Formation. This horizon consists of olive-green to black mudstones and black, organic carbon-rich, laminated shales. The Scaglia Bianca Formation is composed mostly marly limestones.

The Carpathians can be subdivided into two tectonic zones, the Inner and Outer Carpathians. The boundary between these two zones is marked by a narrow, tectonically complicated zone the Pieniny Klippen Belt. The Polish part of the Outer Carpathians comprises several nappes and thrust sheets, regarded as remnants of oceanic basins. The Silesian and Subsilesian nappes form the core of the Outer Carpathians. The Silesian Nappe consists of a succession of the Upper Jurassic through Miocene sediments, mainly siliciclastic turbidites. Deposits of the Subsilesian Nappe represent a Lower Cretaceous to Miocene sequence. The deposits of the Silesian Nappe were

laid down in the Silesian basin. During Cretaceous through Paleogene this was a long trough, bordered on the north by the Subsilesian submerged ridge and on the south by the Silesian ridge. The deposits of the Subsilesian Nappe were laid down close to the northern margin of the Carpathian basin in the west, and on a submarine ridge (Subsilesian submerged ridge) between the Silesian and the Skole basins in the east. Sedimentation in the Subsilesian–Silesian basins began during Tithonian time or earlier.

In the Silesian Nappe, the radiolarian-bearing sediments occur in successive lithostratigraphical divisions: the upper part of the middle Lgota beds, the Mikuszowice Chert beds, the lower part of the Barnasiówka Radiolarian Shale Formation, and the Variegated Shale. The Lgota beds (up to 300 m thick) have been subdivided into three informal lithostratigraphic units: the lower, middle and upper Lgota beds. The lower unit consists of thick-bedded sandstones and conglomerates with thin intercalations of black and grey shales. The middle Lgota beds consist mostly of thin to medium bedded siliceous dark grey sandstones and siltstones, interbedded with black, grey, green and spotty, mainly non-calcareous shales. The upper Lgota beds, named the Mikuszowice Chert beds (up to 35 m thick) is a turbiditic sequence of sandstones consisting predominantly of siliciclastic or carbonate grains. The most characteristic feature of these deposits, visible only in thin sections, is high content of siliceous sponge spicules. The microfaunal composition indicates that the material was derived from an outer shelf and transported into a deep basin, below the CCD. In the Subsilesian Nappe, the equivalent of the Lgota beds are the Gaize beds (Albian–upper Cenomanian). Lithologically, these deposits are spiculite-rich turbidites (up to 250 m thick). Both the Lgota beds and the Gaize beds are followed by the Barnasiówka Radiolarian Shale Formation (14 m thick), which includes the organic rich facies of the OAE2 and ferromanganese layers. This unit is followed by the Turonian hemipelagic non-calcareous Variegated Shale which are mainly

non-calcareous, red and green, with rare silty and sandy turbidite intercalations.

According to Bak (2011), there are relatively many spherical Nassellaria such as *H. barbui* and *C. conara* in the OAE 2 horizon in Italy and Poland in the European Tethys Sea. Other species are rare due to phosphorus and eutrophic environment. According to Musavu-Moussavou et al. (2007), *A. sliteri* and *S. communis* occurred in the OAE 2 horizon in Italy in the European Tethys Sea. This occurrence is interpreted that these species favor the eutrophic environment. Both studies was conducted in the OAE2 horizon characterizing by the occurrence of black shale.

In the pelagic sequence within the Oman Ophiolite in the Tethys, black shale is developed and the value of TOC is very low ranging from 0.004 to 0.009 (Fig. 18). However, extinction had occurred in common species (e.g., *H. geyserensis*, *T. pulchra*, *G. biacuta*, *N. mclaughlini*, *G. gutta*, and *T. veneta*) with the assemblage of the OAE2 horizon in Poland. In addition, the extinction patterns are very similar (Fig. 35); the occurrences of the genera *Hemicryptocapsa* and *Holocryptocanium* (although the species are different) are similar to those of Bak (2011), and sporadic occurrence of multi-segmented Nassellaria is also very similar. On the other hand, the diversification and rapid increase of the genus *Rhopalosyringium* after the OAE2 are not recognized in Poland.

In the sediments of the Oman Ophiolite, there is no black shale of the OAE 2. The value of TOC is extremely low as 0.004 to 0.009% (Fig. 18) and no trace of organic matters can be recognized. From this fact, although the scale is unknown, at least the deep ocean bottom of the Tethys of Oman is oxidative and the anoxic water mass was not developed in the bottom. However, similar species are extinct in the Tethys of Oman and European Tethys and there is a commonality that spherical Nassellaria increases rapidly in the OAE2 horizon. From this, the cause of the extinction of radiolarians in the Tethys of Oman is considered to be the development of anoxic water mass as well as

the European Tethys in the middle layer within a water column. On the other hand, after the OAE2, the diversification and rapid increase of *Rhopalosyringium* can be recognized in the Tethys of Oman. These characteristics is not recognized in the European Tethys. Therefore, it is possible that the recovery processes are different in the Tethys of Oman and the European Tethys.

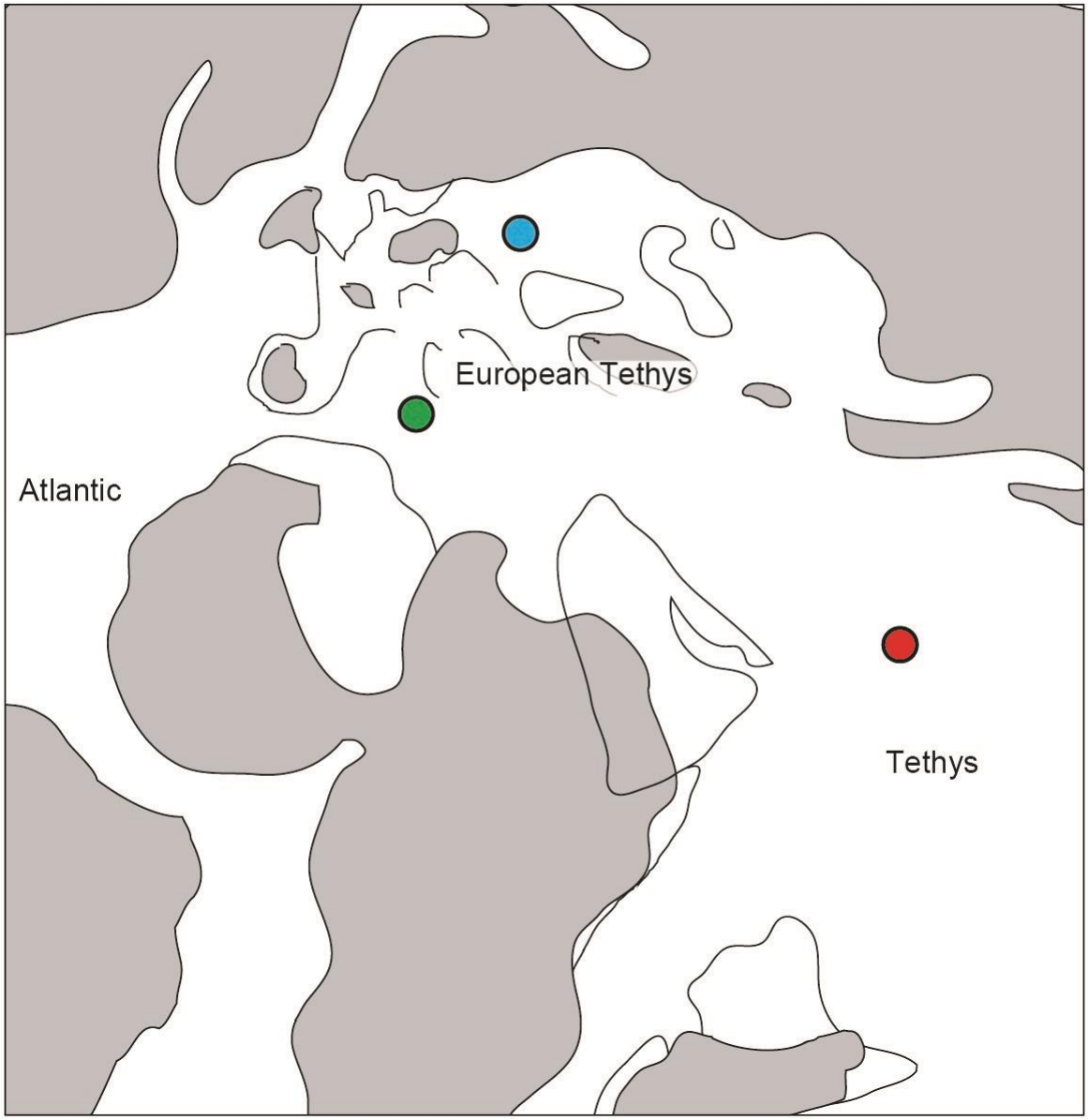

Fig. 34. Paleogeographic map showing the sections (modified from Arthur et al., 1990). Red circle indicates the location of an oceanic floor of the future Oman Ophiolite (This study). Green circle indicates the location of the study section by Bak (2011) Musavu-Moussavou et al. (2007) in Italy. Blue circle indicates the location of the study section by Bak (2011) in Poland.

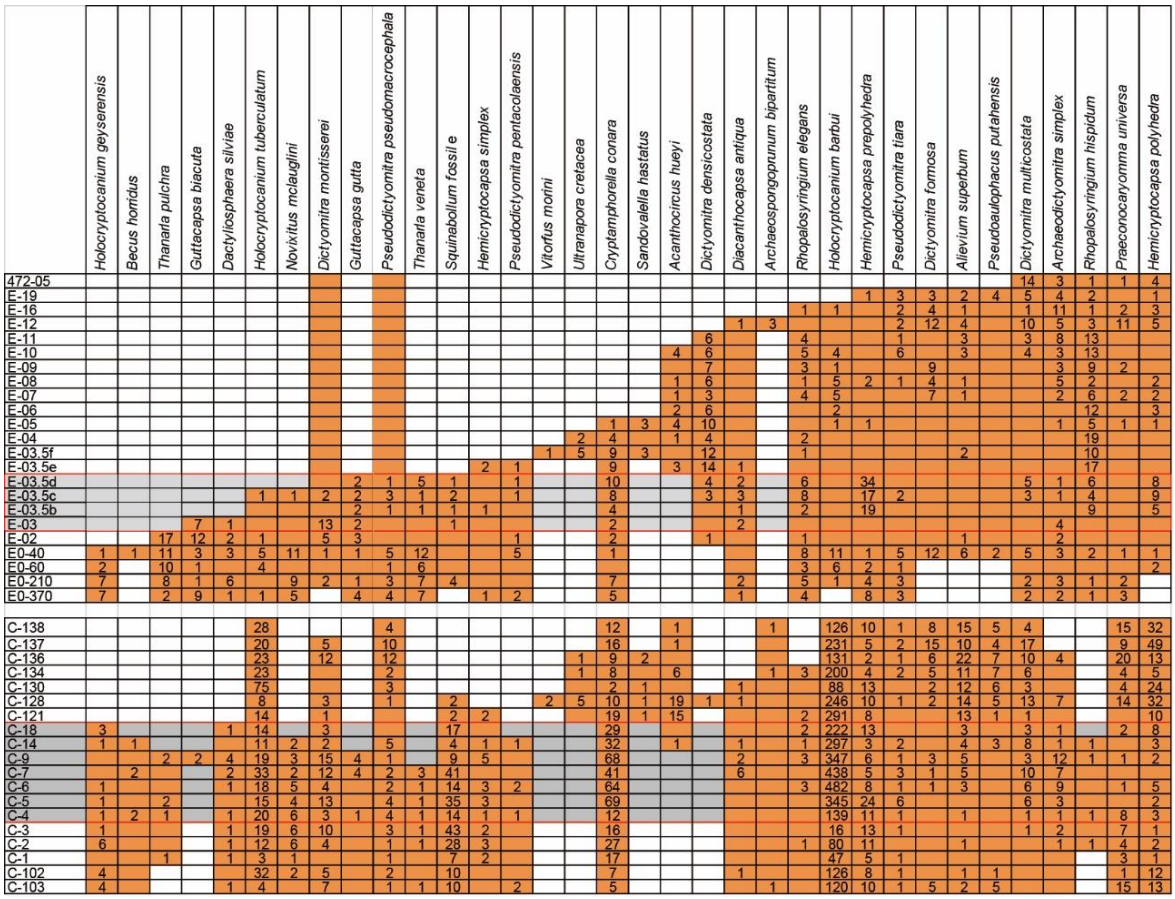

Fig. 35. Occurrence pattern of radiolarians in the pelagic sequence within the Oman Ophiolite (this study) and Poland (Bak, 2011). The upper indicates the radiolarian occurrence of Oman. The lower indicates the radiolarian occurrence of Poland. The gray cells of Poland are the OAE2 horizons. The gray cells of Oman are equivalent to the OAE2 horizons.

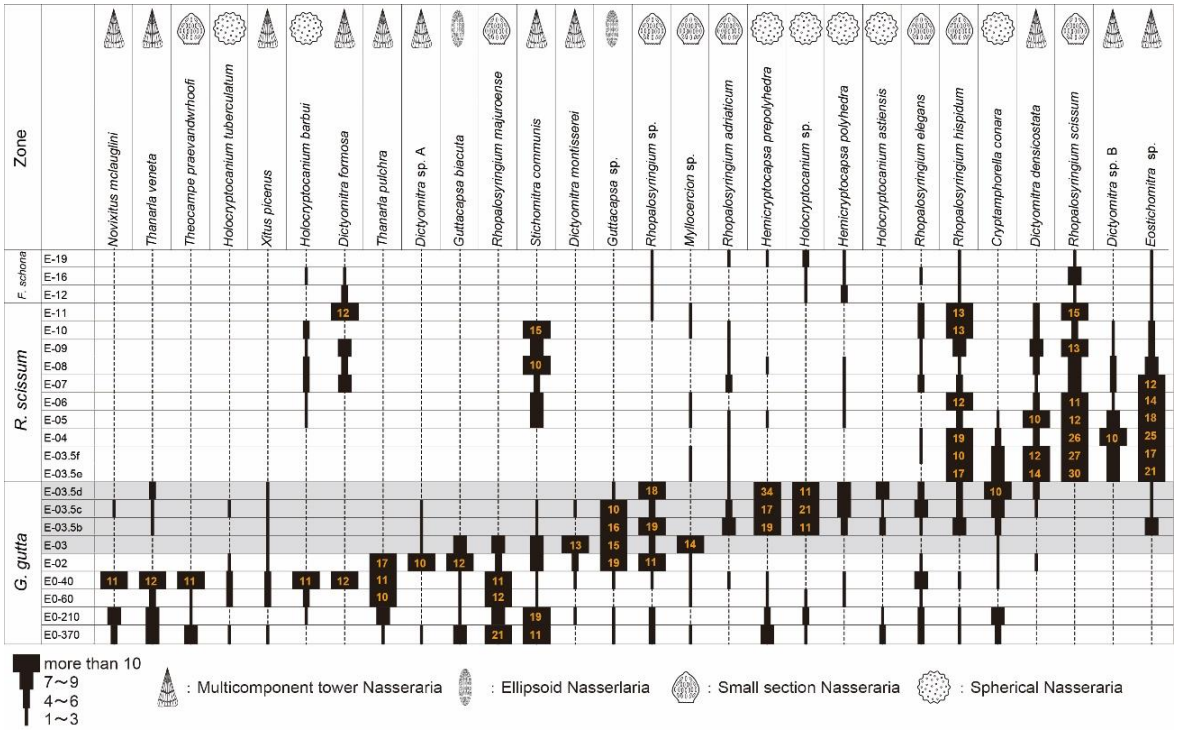

Fig. 36. Number of radiolarians in the pelagic sequence within the Oman Ophiolite. The gray cells of Oman are equivalent to the OAE2 horizons.

7. 10. Marine environmental change of the Tethys sea in the Late Cretaceous

Regarding the normal marine environment in the late Cretaceous, the present study follows the model by Tajika and Yamanaka (2003). In the model by Tanaka and Yamanaka (2003), the amount of evaporation of seawater from the sea surface in the equatorial region increased due to global warming, and then a heavy surface water with relatively high oxygen and salt contents was formed. This water sank in the equatorial region, and the deep water circulation became active along with the supply of nutrient from a deep water. This led to high biological productivity of the surface layer. In this model, anoxic condition mainly occurs in the middle layer of the water column and the amount of dissolved oxygen in the deep water increases. In the following, the change of the marine environment in the late Cenomanian to Coniacian are discussed.

Normal state of marine environment in the Late Cretaceous: In the Late Cretaceous period, the magmatic activity was activated by the influence of hot plume. CO2 concentration was steadily high, meaning that it was in a very hot environment. The main primary producer of the marine surface layer was calcareous nannoplankton Both in Tethys of Oman and European Tethys. Biological productivity of the surface layer was high, and the oxygen minimum zone was developed in the middle layer. Carbonate rocks were accumulated in Europe, whereas red mudstone was deposited in Oman due to the dissolution of carbonates by the influence of the hydrothermal activity related to the erupted of the V1 lava (Fig. 37).

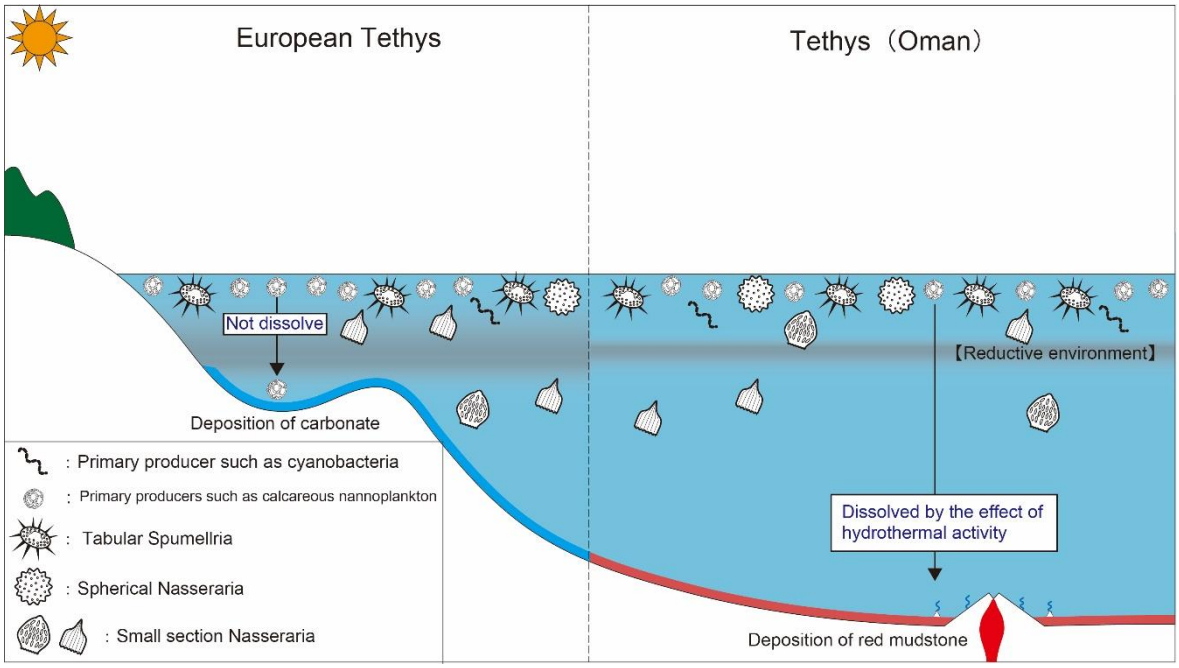

Fig. 37. Normal state of marine environment in the Late Cretaceous time.

Formation of LIPs and associated environmental changes: The Caribbean Large Igneous Province erupted in the late Cenomanian (95-92 Ma) (Snow et al., 2005). Large amounts of CO_2 and SO_2 were released into the atmosphere, and the CO_2 concentration in the atmosphere rose leading to global warming. The high temperature environment promoted weathering of continents, which caused to flow nutrients into the ocean and eutrophication. Eutrophication stimulates primary producers of marine surface layers such as calcareous nannoplankton. At the same time, the high concentration of CO_2 in the atmosphere caused ocean acidification (Du Vivier et al., 2015) (Fig. 38).

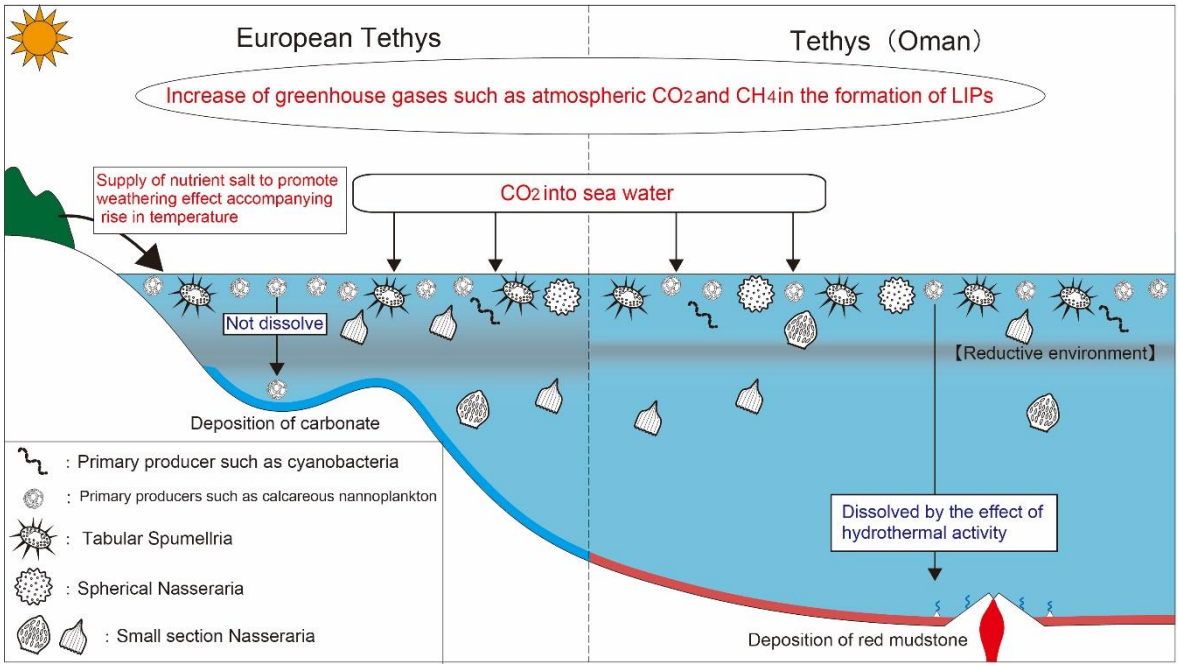

Fig. 38. Marine environment in the late Cenomanian.

Expansion phase of oxygen minimum layer: Due to ocean acidification, calcareous nannoplankton was greatly damaged and drastically decreased. Primary producers of oceanic surface were replaced by cyanobacteria and dinoflagellates, and they were increased rapidly due to abundant nutrients (Okochi, 2003; Ando et al., 2016). By using oxygen to decompose organic matter such as increased cyanobacteria and dinoflagellates, the oxygen minimum zone in the middle layer was expanded. The expansion of the oxygen minimum zone caused stepwise extinction of radiolarians in the European Tethys and Tethys of Oman. In addition, in the European Tethys, the oxygen minimum zone reached the ocean floor, leading to the deposition of black shale. On the other hand, because of the depth in the Tethys Sea of Oman, the oxygen minimum layer was not developed up to the ocean floor. Thus, the ocean floor was an oxidative environment. The organic matter was decomposed, and red mudstone was deposited under oxic condition (Fig. 39).

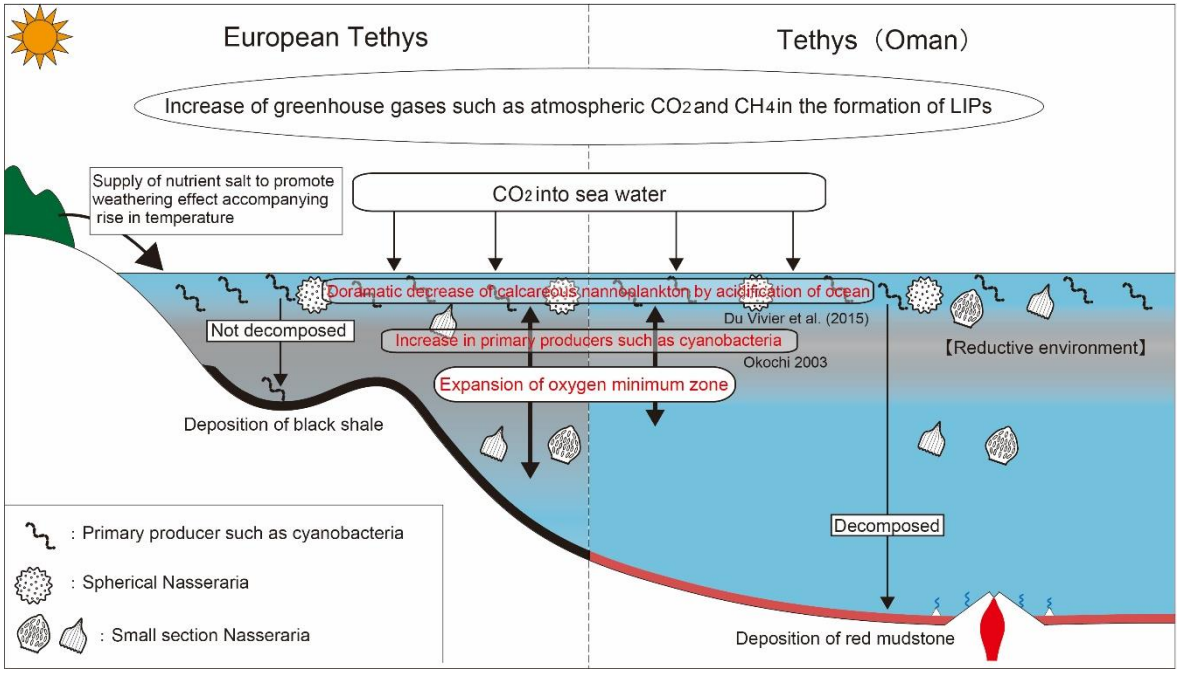

Fig. 39. Marine environment in the beginning of the OAE2 in the late Cenomanian.

Developed phase of the oxygen minimum zone: The oxygen minimum zone was most developed. In the European Tethys, most of radiolarians were extinct in the middle to bottom layers. Similarly, radiolarians living in the middle layer were extinct in the Tethys of Oman. However, in both the areas, spherical Nassellaria increased dramatically in the surface layer that is rich in oxygen (Fig. 40).

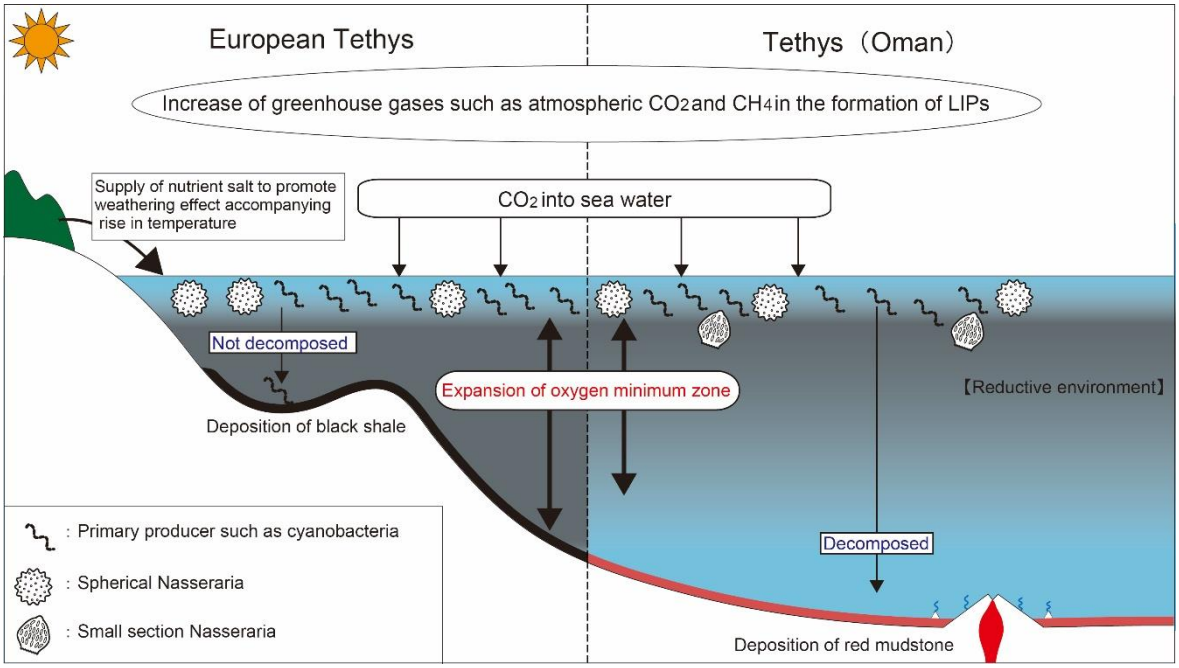

Fig. 40. Marine environment in the OAE2 in late Cenomanian.

Recovery from the expansion of the oxygen minimum Zone: The subduction of a surface water and ocean circulation were activated again in the Tethyan equatorial area in the latest Cenomanian. Along with this, the oxygen minimum zone shrank and the marine environment returned to the normal condition. Primary producers of the surface layer were again taken over from cyanobacteria and dinoflagellates to calcareous nannoplankton. Spherical Nassellaria were also decreased, whereas discoidal and spherical Spumellaria were increased. In addition, the increase and diversification the genus *Rhopalosyringium* were progressed in the Tethys of Oman. On the other hand, the recovery in European Tethys could be delayed because the area was geographically closed and remained the influence of the anoxic water (Fig. 41).

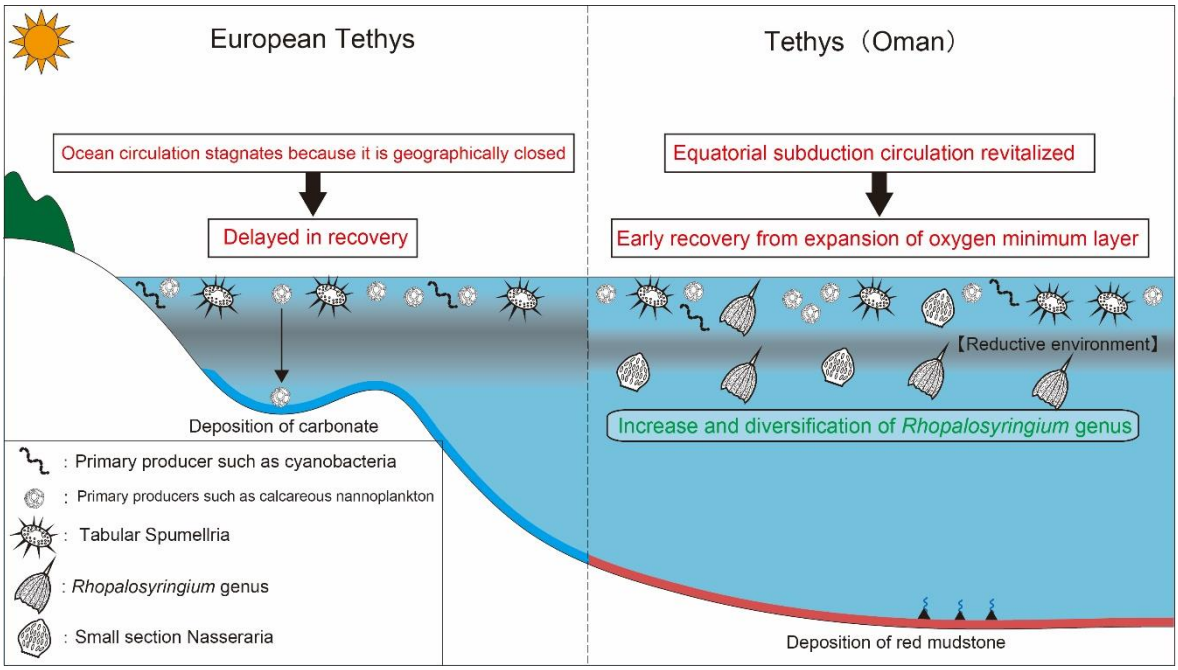

Fig. 41. Recovery from the OAE 2 in the latest Cenomanian.

Complete recovery from the expansion of the oxygen minimum Zone: In the middle Turonian, the ocean environment recovers completely in the European Tethys. The genus *Rhopalosyringium* migrated from the Tethys of Oman to the European Tethys, taking the ocean current from the east to west. In the Tethys of Oman, the hydrothermal activity of the seafloor was weakened, and then the micritic limestone began to deposit (Fig. 42). In the late Turonian to Coniacian, the depth of the CCD became shallow, and red mudstone deposited again

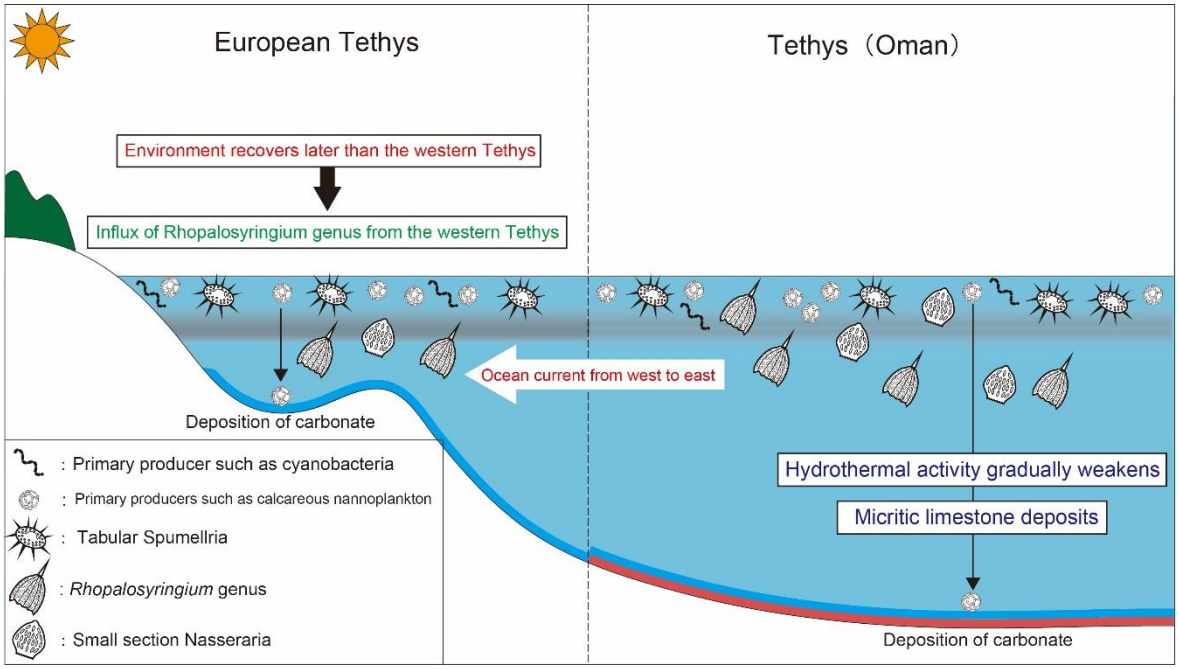

Fig. 42. Marine environment after the OAE2 in the Turonian.

8. Conclusion

New results of the present lithostratigraphic and biostratigraphic study for the Suhaylah and Zabyat formations are summarized as follows. In particular, the high-resolution radiolarian biostratigraphic study provides age constraints on the termination of the V1, V2, and V3 lava. In addition, the comparative study for the radiolarian assemblages between the Tethys of Oman and Europe Tethys has been conducted to clarify the marine environment during late Cenomanian to early Turonian.

(1) As described in previous studies, the Suhaylah Formation consists mainly of lower metalliferous sediments (umbers) that grade into overlying red mudstone intercalated with radiolarian chert, which is in turn overlain by upper micritic limestone. These strata preserve an essentially continuous record from the first deposition of metalliferous sediments related to hydrothermal activity around a ridge, to the subsequent pelagic sedimentation of red mudstone with chert and micritic limestone slightly farther from the ridge. All lithologies contain moderately to well-preserved radiolarians that allow age determinations.

(2) Four distinctive middle-late Cenomanian to Coniacian radiolarian assemblages occur in the studied sections. Based on the biohorizons of radiolarians, four radiolarian zones were defined. The *Guttacapsa gutta* Zone, obtained from metalliferous sediments and chert intercalations within red mudstone, could be correlated with the middle to lateset Cenomanian. The *Rhopalosyringium scissum* Zone, recovered from red mudstone and chert, is assigned to the lateset Cenomanian to early Turonian. The *Foremanina schona* Zone, recognized in micritic limestone, is correlated with the middle Turonian. The *Eostichomitra perapedhia* Zone, recovered from red mudstone of the uppermost part of the Suhaylah Formation and the top of the Zabyat

Formation, is assigned to the late Turonian to Coniacian.

(3) The radiolarian age of the sediments overlying the V1 lava is consistent with the high-precision U-Pb zircon age of crustal rocks formed by ridge magmatism. The depositional age of the pelagic sediments indicates that ridge magmatism had ended by middle–late Cenomanian. In addition, the sediments on the V2 lava can be correlated with the middle–late Cenomanian. These findings reveal that the change of the tectonic setting from mid-ocean ridge through subduction zone to oceanic thrusting occurred in a short period and the activities of the V1 to V2 lavas were terminated in late Cenomanian.

(4) The radiolarian age of the red mudstone just beneath the V3 lava is late Tulonian–Coniacian. Therefore it is concluded that the V3 lava erupted from late Turonian to Coniacian by intra-plate volcanism.

(5) Based on the discrimination diagrams by Murray (1994), the rocks of the Suhaylah and Zabyat formations ranges from the ridge to pelagic environments. In particular, metalliferous sediments and chert intercalation plot within the ridge field, whereas the other sediments plots within the pelagic field. These findings suggest that the Suhaylah and Zabyat formations were deposited in the pelagic environment and were not influenced by inputs of terrigenous materials. Redox indicators of Ce/Ce*, Th/U, and TOC suggest that the ocean floor was oxic conditions during Cenomanian–Turonian.

(6) Similar species are extinct in the Tethys of Oman and European Tethys. There is a commonality that spherical Nassellaria increased rapidly in the OAE2 horizon in both the regions. From these facts, the cause of the extinction of radiolarians in the Tethys of Oman is considered to be the development of anoxic water mass as well as the European Tethys in the

middle layer within a water column.

(7) After the OAE2, the diversification and rapid increase of *Rhopalosyringium* can be recognized in the Tethys of Oman. These characteristics is not recognized in the European Tethys. Therefore, it is possible that the recovery processes are different in the Tethys of Oman and the European Tethys; namely, the radiolarian ecosystem was recovered quickly from environmental degradation in the Tethys of Oman that was open ocean, rather than closed European Tethys.

9. Acknowledgements

I would like to express my gratitude to Professor Atsushi Matsuoka for his supervision. I also wish to express my thanks to Dr. Toshiyuki Kurihara for reading of the manuscript. I am grateful to Professors M. Satish Kumar and Tsuyoshi Toyoshima and Dr. Hiroshi Kurita for their helpful suggestions and encouragements. I express my thanks to Professor Sumio Miyashita, Professor Susumu Umino, Professor Eiichi Takazawa, Dr. Yuki Kusano, Dr. Yoshiko Adachi, and Professor Nobutaka Tuchiya for their kind supports during my field surveys. I heartily thank Professor Takashi Hasegawa and Dr. Hidetoshi Hara for their helps of geochemical analyses. Special thanks are due to Drs. Hayato Ueda and Yuta Shiino for their kind suggestions. I thank the Ministry of Commerce and Industry, Directorate General of Minerals in Oman for facilitating my fieldwork.

10. References

Adachi, Y. and Miyashita, S., 2003, Geology and petrology of the plutonic complexes in the Wadi Fizh area: Multiple magmatic events and segment structure in the northern Oman ophiolite. Geochem. Geophys. Geosyst., 4, 8619, doi: 10.1029/2001GC000272.

Adachi, M., Yamamoto, K and Sugisaki, R., 1986, Hydrothermal chert and associated siliceous rocks from the northern Pacific: their geological significance and indication of ocean ridge activity. Sed. Geol., 47, 125–148.

Alabaster, T., Pearce, J.A. and Malpas, J., 1982, The volcanic stratigraphy and petrogenesis of the Oman ophiolite complex. Contrib. Mineral. Petrol., 81, 168–183.

Algeo, T.J and Maynard, J.B., 2004, Trace-element behavior and redox facies in core shalesof Upper Pennsylvanian Kansas-type cyclothems. Chem. Geol., 206, 289–318.

Arai, S., Kadoshima, K. and Morishita, T., 2006, Widespread arc-related melting in the mantle section of the northern Oman ophiolite as inferred from detrital chromian spinels. J. Geol. Soc. London, 163, 869–879.

Arthur, M. A. and Premoli Silva, I., 1982. Development of wide spread organic car bon-rich strata in the Mediterranean Tethys. In: Schlanger, S. O. & Cita, M. B. (eds), Nature and origin of Cretaceous carbon-rich facies. Academic Press, London, 7–54.

Arthur, M.A., Dean, W.E. and Pratt, L.M., 1988, Geochemical and climatic effects of increased marine organic carbon burial at the Cenomanian/Turonian boundary. Nature, 335, 714–717.

A'Shaikh, D., Miyashita, S. and Matsueda, H., 2005, The petrological and geochemical characteristics of an ophiolite volcanic suite from the Ghayth area of Oman. J. Mineral. Petrol. Sci., 100, 202–220.

Bąk, M., 2011, Tethyan radiolarians at the Cenomanian-Turonian Anoxic Event from the Apennines (Umbria-Marche) and the Outer Carpathians:

palaeoecological and palaeoenvironmental implications. Studia Geol. Polonica, 134, 5–279.

Bandini, A.N., Flores, K., Baumgartner, P.O., Jackett, S.-J. and Denyer, P, 2008, Late Cretaceous and Paleogene Radiolaria from the Nicoya Peninsula, Costa Rica: a tectonostratigraphic application. Stratigraphy, 3–21.

Bellanca, A., Masetti, D. and Neri, R., 1997, Rare earth elements in limestone/marlstonecouplets from the Albian - Cenomanian Cismon section (Venetian region, northern Italy): assessing REE sensitivity to environmental changes. Chem. Geol., 141, 141–152.

Beurrier, M., Bourdillon-de Grissac, C., De Wever, P. and Lescuyer, J.-L., 1987, Biostratigraphie des radiolarites associées aux volcanites ophiolitiques de la nappe de Samail (Sultanat d'Oman): conséquences tectogénétiques. C.R. Acad. Sci. Paris, Série II, 304, 907–910.

Bishimetal Exploration Co. Ltd., 1987, Geological Map of Wadi Bani Umar, sheet NG40-14E-II, scale 1:50,000 with explanatory notes. Minist. of Pet. and Miner., Muscat.

Blome, C.D. and Irwin, W.P., 1985, Equivalent radiolarian ages from ophiolitic terranes of Cyprus and Oman. Geology, 13, 401–404.

Bragina, L.G., 2004, Cenomanian-Turonian radiolarians of northern Turkey and the Crimean Mountains. Paleont. J., 38, 325–456.

Bragina, L.G., 2016, Radiolarian-based zonal scheme of the Cretaceous (Albian–Santonain) of the Tethyan Regions of Eurasia. Stratigraphy and Geological Correlation, 2016, 24, 141–166.

Coffi n, M.F., and Eldholm, O., 1994, Large igneous provinces: Crustal structure, dimensions, and external consequences. Reviews of Geophysics, 32, 1–36, doi:10.1029/93RG02508.

De Baar, H.J.W., Bacon, M.P., Brewer, P.G. and Bruland, K.W., 1985, Rare earth elements in the Pacific and Atlantic Oceans. Geochim. Cosmochim., 49, 1943-1959.

De Wever, P., Bourdillon-de Grissac, C. and Beurrier, M., 1988, Radiolaires Sénoniens de la nappe de Samail (Oman). Rev. micropaléont., 31, 166–179.

Du Vivier, A.D., Jacobson, A.D., Lehn, G.O., Selby, D., Hurtgen, M.T. and Sageman, B.B., 2015, Ca isotope stratigraphy across the Cenomanian–Turonian OAE2: links between volcanism, seawater geochemistry, and the carbonate fractionation factor. Earth and Planetary Science Letters, 416, 121–131.

Dumitrica, P., 1970, Cryptocephalic and cryptothoracic Nassellaria in some Mesozoic deposits of Romania. Rev. Roum. Geol. Geophys. Geogr., 14, 45–124.

Dumitrica, P., Immenhauser, A. and Dumitrica-Jud, R., 1997, Mesozoic radiolarian biostratigraphy from Masirah Ophiolite, Sultanate of Oman. Part I: Middle Triassic, uppermost Jurassic and Lower Cretaceous spumellarians and multisegmented nassellarians. Bull. Natl. Mus. Nat. Sci., 9, 1–106.

Eggins, S.M., Woodhead, J.D., Kinsley, L.P.J., Mortimer, G.E., Sylvester, P., McCulloch, M.T., Hergt, J.M. and Handler, M.R., 1997, A simple method for the precise determination of ≥ 40 trace elements in geological samples by ICPMS using enriched isotope internal standardization. Chem. Geol., 134, 311–326.

Einaudi, F., Godard, M., Pezard, P., Cochemé, J.-J., Coulon, C., Brewer, T. and Harvey, P., 2003, Magmatic cycles and formation of the upper oceanic crust at spreading centers: Geochemical study of a continuous extrusive section in the Oman ophiolite. Geochem. Geophys. Geosyst., 4, 8608, doi:10.1029/2002GC000362.

Elder, W.P., 1989, Molluscan extinction patterns across the Cenomaniane–Turonian stage boundary in the western interior of the United States. Paleobiology, 15, 299–320.

Empson-Morin, K.M., 1981, Campanian Radiolaria from DSDP Site 313, Mid-Pacific Mountains. Micropaleontology, 27, 249–292.

Erbacher, J., 1994, Entwicklung und Paläoozeanographie mittelkretazischer Radiolarien der westlichen Tethys (Italien) und des Nordatlantiks. Tübinger Mikropaläont. Mitt., 12, 1–120.

Erbacher, J., Thurow, J., and Littke, R., 1996, Evolution patterns of radiolaria and organic matter variations: a new approach to identify sea-level changes in mid-Cretaceous pelagic environments. Geology, 24, 499–502.

Erbacher, J. and Thurow, J., 1997, Influence of oceanic anoxic events on the evolution of mid-Cretaceous radiolaria in the North Atlantic and western Tethys. Mar. Micropaleont., 30, 139–158.

Ernewein, M., Pflumio, C. and Whitechurch, H., 1988, The death of an accretion zone as evidenced by the magmatic history of the Sumail ophiolite (Oman). Tectonophysics, 151, 247–274.

Fleet, A.J. and Robertson, A.H.F., 1980, Ocean-ridge metalliferous and pelagic sediments of the Semail Nappe, Oman. J. Geol. Soc. London, 137, 403–422.

Gallicchio, S., Marcucci, M., Pieri, P., Premoli Silva, I., Sabato, L. and Salvini, G., 1996, Stratigraphical data from a Cretaceous claystones sequence of the “ArgileVaricolori” in the Southern Apennines (Basilicata, Italy). Palaeopelagos, 6, 261–272.

Glennie, K.W., Boeuf, M.G.A., Hughes Clarke, M.W., Moody-Stuart, M., Pilaar, W.F.H. and Reinhardt, B.M., 1973, Late Cretaceous nappes in Oman Mountains and their geologic evolution. Bull. Am. Ass. Petrol. Geol., 57, 5–27.

Glennie, K.W., Boeuf, M.G.A., Hughes Clarke, M.W., Moody-Stuart, M., Pilaar, W.F.H. and Reinhardt, B.M., 1974, Geology of the Oman Mountains. Verhandelingen van het Koninklijk Nederlands geologisch mijnbouwkundig Genootschap, 31, 423 pp.

Godard, M., Bosch, D. and Einaudi, F., 2006, A MORB source for low-Ti magmatism in the Semail ophiolite. Chem. Geol., 234, 58–78.

Godard, M., Dautria, J.-M. and Perrin, M., 2003, Geochemical variability of the Oman ophiolite lavas: Relationship with spatial distribution and paleomagnetic directions. Geochem. Geophys. Geosyst., 4, 8609, doi:10.1029/2002GC000452.

Goodenough, K.M., Styles, M.T., Schofield, D., Thomas, R.J., Crowley, Q.C., Lilly, R.M., McKervey, J., Stephenson, D. and Carney, J.N., 2010, Architecture of the Oman-UAE ophiolite: evidence for a multi-phase magmatic history. Arab. J. Geosci., 3, 439–458.

Gradstein, F.M., Ogg, J.G., Schmitz, M.D. and Ogg, G., 2012, The Geologic Time Scale 2012, Volume 2. Elsevier, Amsterdam, 1144 pp.

Gromet, L.P., Dymek, R.F., Haskin, R.A. and Korotev, R.L., 1984, The "North American shale composite": its complication, major and trace element characteristics. Geochim. Cosmochim, 48, 2469–2482.

Hacker, B.R. and Gnos, E., 1997, The conundrum of samail: explaining the metamorphic history. Tectonophysics, 279, 215–226.

Hasegawa, T., Crampton, J.S., Schiøler, P., Field, B., Fukushi, K. and Kakizaki, Y., 2013, Carbon isotope stratigraphy and depositional oxia through Cenomanian/Turonian boundary sequences (Upper Cretaceous) in New Zealand. Cretaceous research, 40, 61–80.

Hasegawa, T. and Saito, T., 1993. Global synchroneity of a positive carbon isotope excursion at the Cenomanian/Turonian boundary: validation by calcareous microfossil biostratigraphy of the Yezo Group, Hokkaido, Japan. Island Arc, 2, 181–191.

Hatch, J.R. and Leventhal, J.S., 1992, Relationship between inferred redox potential of the depositional environment and geochemistry of the Upper Pennsylvanian (Missourian) Stark Shale Member of the Dennis Limestone, Wabaunsee Country, Kansas, U.S.A. Chem. Geol., 99, 65–82.

Hollis, C.J. and Kimura, K., 2001, A unified radiolarian zonation for the Late Cretaceous and Paleocene of Japan. Micropaleontology, 47, 235–255.

Holser, W.T., 1997, Evaluation of the application of rare-earth elements to

paleoceanography. Palaeogeogr. Palaeoclimatol. Palaeoecol., 132, 309–323.

Hori, R.S., Higuchi, Y., Fujiki, T., Maeda, T. and Ikehara, M., 2007, Geochemistry of the Oruatemanu Formation, Arrow Rocks, Northland, New Zealand. In: Spoerli, K.B., Takemura, A., Hori, R.S. (Eds.), The Oceanic Permian/Triassic Boundary Sequence at Arrow Rocks (Oruatemanu), Northland, New Zealand. : GNS Sci. Monograph, 24. GNS Sci., Lower Hutt, 123–156.

Huber, B.T., Hodell, D.A. and Hamilton, C.P., 1995, Middle-Late Cretaceous climate of the southern high latitudes: Stable isotopic evidence for minimal equator-to-pole thermal gradients. Geol. Soc. Am. Bull., 107, 1164–1191.

Ishikawa, T., Nagaishi, K. and Umino, S., 2002, Boninitic volcanism in the Oman ophiolite: Implications for thermal condition during transition from spreading ridge to arc. Geology, 30, 899–902.

Jenkyns, H.C., Gale, A.S. and Corfield, R.M., 1994, Carbon-and oxygen-isotope stratigraphy of the English Chalk and Italian Scaglia and its palaeoclimatic significance. Geol. Mag., 131, 1–34.

Jones, B. and Manning, D.A.C., 1994, Comparison of geochemical indices used for the interpretation of paleoredox conditions in ancient mudstones. Chem. Geol., 111, 111–129.

Juteau, T., Ernewein, M., Reuber, I., Whitechurch, H. and Dahl, R., 1988, Duality of magmatism in the plutonic sequence of the Sumail Nappe, Oman. Tectonophysics, 151, 107–135.

Kimura, H. and Watanabe, Y., 2001, Oceanic anoxia at the Precambrian-Cambrian boundary. Geology, 29, 995–998.

Kuhnt, W., 1990, Agglutinated foraminifera of western Mediterranean Upper Cretaceous pelagic limestones (Umbrian Apennines, Italy, and Betic Cordillera, Southern Spain). Micropaleontology, 36, 297–330.

Kuroda, J., Ogawa, N.O., Tanimizu, M., Coffi n, M.F., Tokuyama, H., Kitazato, H., and Ohkouchi, N., 2007, Contemporaneous massive subaerial

volcanism and late Cretaceous Oceanic Anoxic Event 2. Earth and Planetary Science Letters, 256, 211–223, doi:10.1016/j.epsl.2007.01.027.

Kusano, Y., Adachi, Y., Miyashita, S. and Umino, S., 2012, Lava accretion system around mid-ocean ridges: Volcanic stratigraphy in the Wadi Fizh area, northern Oman ophiolite. Geochem. Geophys. Geosyst., 13, Q05012, doi: 10.1029/2011GC004006.

Kusano, Y., Hayashi, M., Adachi, Y., Umino, S. and Miyashita, S., 2014, Evolution of volcanism and magmatism during initial arc stage: constraints on the tectonic setting of the Oman Ophiolite. In: H.R. Rollinson, M.P. Searle, I.A. Abbasi, A. Al-Lazki and M.H. Al Kindi (Eds.), Tectonic Evolution of the Oman Mountains. Geol. Soc. London Spec. Publ., 392, 177–193.

Larson, R.L., 1991, Geological consequences of superplumes. Geology, 19, 963–966, doi:10.1130/0091-7613(1991)019<0963:GCOS>2.3.CO;2.

Larson, R.L., and Erba, E., 1999, Onset of the mid-Cretaceous greenhouse in the Barremian–Aptian. Igneous events and the biological, sedimentary, and geochemical responses. Paleoceanography, 14, 663–678, doi:10.1029/1999PA900040.

Leckie, R.M., Bralower, T.J., and Cashman, R., 2002, Oceanic anoxic events and plankton evolution: Biotic response to tectonic forcing during the mid-Cretaceous. Paleoceanography, 17, 1–29, doi:10.1029/2001PA000623.

Lippard, S.J., Shelton, A.W. and Gass, I.G., 1986, The Ophiolite of Northern Oman. Geol. Soc. London Mem., 11, 178 pp.

Marchegiani, L., Bertotti, G., Cello, G., Deiana, G., Mazzoli, S. and Tondi, E., 1999, Pre-orogenic tectonics in the Umbria-Marche sector of the Afro-Adriatic continental margin. Tectonophysics, 315, 123–143.

Marcucci Passerini, M., Bettini, P., Dainelli, J. and Sirugo, A., 1991, The "Bonarelli Horizon" in the central Apennines (Italy): radiolarian biostratigraphy. Cretaceous Res., 12, 321–331.

Matsumoto, R., Minai, Y. and Okamura, M., 1988, Geochemistry and

depositional environments of bedded chert of the Cretaceous Shimanto Group, Shikoku, southwest Japan. Mod. Geol., 12, 197–224.

McLennan, S.M., 1989, Rare earth elements in sedimentary rocks: influence of provenance and sedimentary processes. Geochemistry and Minerology of Rare Earth Elements, 169–200.

Miller, K.G., Kominz, M.A., Browning, J.V., Wright, J.D., Mountain, G.S., Katz, M.E., Sugarman, P.J., Cramer, B.S., Christie-Blick, N. and Pekar, S.F., 2005, The Phanerozoic record of global sea-level change, Science, 310, 1293–1298, doi:10.1126/science.1116412.

Moix, P., Goričan, Š. and Marcoux, J., 2009, First evidence of Campanian radiolarians in Turkey and implications for the tectonic setting of the Upper Antalya Nappes. Cretaceous Res., 30, 952–960.

Moriya, K., Wilson, P.A., Friedrich, O., Erbacher, J. and Kawahata, H., 2007, Testing for ice sheets during the mid-Cretaceous greenhouse using glassy foraminiferal calcite from the mid-Cenomanian tropics of Demerara Rise. Geology, 35, 615–618, doi:10.1130/G23589A.1.

Murray, R.W., 1994, Chemical criteria to identify the depositional environment of chert: general principles and applications. Sed. Geol., 90, 213–232.

Murray, R.W., Buchholtz ten Brink, M.R., Gerlach, D.C., Russ III, G.P. and Jones, D.L., 1992, Interoceanic variation in the rare earth, major, and trace element depositional chemistry of chert: perspectives gained from the DSDP and ODP record. Geochim. Cosmochim., 56, 1897–1913.

Murray, R.W., Buchholtz ten Brink, M.R., Gerlach, D.C., Russ III, G.P. and Jones, D.L., 1991, Rare earth, major, and trace elements in chert from the Franciscan Complex and Monterey Group, California: assessing REE sources to fine-grained marine sediments. Geochim. Cosmochim., 55, 1875–1895.

Murray, R.W., Buchholtz ten Brink, M.R., Jones, D.L., Gerlach, D.C. and Russ III, G.P., 1990, Rare earth elements as indicators of different marine

depositional environments in chert and shale. Geology, 18, 268–271.

Musavu-Moussavou, B., Danelian, T., Baudin, F., Coccioni, R. and Fröhlich, F., 2007, The Radiolarian biotic response during OAE2. A high-resolution study across the Bonarelli level at Bottaccione (Gubbio, Italy). Rev. micropaléont., 50, 253–287.

Musavu-Moussavou, B. and Danelian, T., 2006, The radiolarian response to oceanic anoxic event 2 in the southern part of the Northern proto-Atlantic (Demerara Rise, ODP leg 207). Revue de Micropal´eontologie, 49, 141–163.

Nicolas A., 1989, Structures of Ophiolites and Dynamics of Oceanic Lithosphere. Kluwer Acad. Publ., Dordrecht, 367 pp.

Nicolas, A. and Boudier, F., 2003, Where ophiolites come from and what they tell us. In: Y. Dilek and S. Newcomb (Eds.), Ophiolite Concept and the Evolution of Geological Thought. Geol. Soc. Am. Spec. Pap., 373, 137–152.

Nicolas, A., Boudier, F. and France, L., 2009, Subsidence in magma chamber and the development of magmatic foliation in Oman ophiolite gabbros. Earth Planet. Sci. Lett., 284, 76–87.

O'Dogherty, L., 1994, Biochronology and paleontology of Mid-Cretaceous radiolarians from northern Apennines (Italy) and Betic Cordillera (Spain). Mém. Géol. (Lausanne), 21, 1–415.

O'Dogherty, L., Carter, E.S., Dumitrica, P., Goričan, Š., De Wever, P., Bandini, A.N., Baumgartner, P.O. and Matsuoka, A., 2009, Catalogue of Mesozoic radiolarian genera. Part 2: Jurassic-Cretaceous. Geodiversitas, 31, 271–356.

O'Dogherty, L. and Guex, J., 2002, Rates and pattern of evolution among Cretaceous radiolarians relations with global paleoceanographic events. Micropaleontology, 48, 1–22.

Ohkouchi, N., Kuroda, J., Okada, M. and Tokuyama, H., 2003 Why Cretaceous black shales have high C/N ratios? Implications from SEM-EDX observations for Livello Bonarelli black shales at the Cenomanian-Turonian boundary. Front. Res. Earth Evol, 1, 239–241.

Ozaki, K. and Tajika, E., 2013, Biogeochemical effects of atmospheric oxygen concentration, phosphorus weathering, and sea-level stand on oceanic redox chemistry: Implications for greenhouse climates. Earth and Planetary Science Letters, 373, 129–139.

Pattan, J.N., Pearce, N.J.G. and Mislankar, P.G., 2005, Constraints in using Cerium-anomaly of bulk sediments as an indicator of paleo bottom water redox environment: a case study from the Central India Ocean Basin. Chem. Geol., 221, 260–278.

Pearce, J.A., Alabaster, T., Shelton, A.W. and Searle, M.P., 1981, The Oman ophiolite as a Cretaceous arc-basin complex: evidence and implications. Philos. Trans. Royal Soc. London, A 300, 299–317.

Pessagno, Jr. E.A., 1969, Upper Cretaceous Stratigraphy of the Western Gulf Coast Area of México, Texas, and Arkansas. Geol. Soc. Am. Mem., 111, 1–139.

Pessagno, Jr. E.A., 1977, Lower Cretaceous radiolarian biostratigraphy of the Great Valley Sequence and Franciscan Complex, California Coast Ranges. Cushman Foundation for Foraminiferal Research, Spec. Publ., 15, 1–87.

Pessagno, Jr. E.A. and Newport, R.L., 1972, A technique for extracting Radiolaria from radiolarian cherts. Micropaleontology, 18, 231–234.

Reinhardt, B.M., 1969, On the genesis and emplacement of ophiolites in the Oman Mountains geosyncline. Schweiz. Min. Petrol. Mitt., 49, 1–39.

Rimmer, S.M., 2004, Geochemical paleoredox indicators in Devonian - Mississippian black shales, Central Appalachian Basin (USA). Chem. Geol., 206, 373–391.

Rioux, M., Garber, J., Bauer, A., Bowring, S., Searle, M., Kelemen, P. and Hacker, B., 2016. Synchronous formation of the metamorphic sole and igneous crust of the Semail ophiolite: New constraints on the tectonic evolution during ophiolite formation from high-precision U–Pb zircon geochronology. Earth and Planetary Science Letters, 451, 185–195.

Rioux, M., Bowring, S., Garber, J., Kelemen, P., Searle, M., Miyashita, S. and Adachi, Y., 2014, The development of subduction below the Oman-UAE ophiolite: Detailed temporal constraints from high precision U-Pb Zircon geochronology. AGU fall meeting 2014, abstracts, V51F-03.

Rioux, M., Bowring, S., Kelemen, P., Gordon, S., Dudás, F. and Miller, R., 2012, Rapid crustal accretion and magma assimilation in the Oman-U.A.E. ophiolite: High precision U-Pb zircon geochronology of the gabbroic crust. J. Geophys. Res., 117, B07201, doi:10.1029/2012JB009273.

Rioux, M., Bowring, S., Kelemen, P., Gordon, S., Miller, R. and Dudás, F., 2013, Tectonic development of the Samail ophiolite: High-precision U-Pb zircon geochronology and Sm-Nd isotopic constraints on crustal growth and emplacement. J. Geophys. Res., Solid Earth, 118, 2085-2101, doi:10.1002/jgrb.50139, 2013.

Robertson, A.H.F., 1975, Cyprus umbers: basalt-sediment relationships on a Mesozoic ocean ridge. J. Geol. Soc. London, 131, 511–531.

Robertson, A.H.F. and Fleet, A.J., 1986, Geochemistry and palaeo-oceanography of metalliferous and pelagic sediments from the Late Cretaceous Oman ophiolite. Mar. Petrol. Geol., 3, 315–337.

Robertson, A.H.F. and Hudson, J.D., 1974, Pelagic sediments in the Cretaceous and Tertiary history of the Troodos Massif, Cyprus. In: K.J. Hsü and H.C. Jenkyns (Eds.), Pelagic sediments: on land and under the Sea. Spec. Publ. Int. Ass. Sedim., 1, 403–436.

Robertson, A.H.F. and Woodcock, N.H., 1983a, Zabyat Formation, Semail Nappe, Oman: sedimentation on to an emplacing ophiolite. Sedimentology, 30, 105–116.

Robertson A.H.F. and Woodcock N.H., 1983b. Genesis of the Batinah mélange above the Semail ophiolite, Oman. J. Struct. Geol., 5, 1–17.

Robin, C., Goričan, Š., Guillocheau, F., Razin, P., Dromart, G. and Mosaffa, H., 2010, Mesozoic deep-water carbonate deposits from the southern Tethyan passive margin in Iran (Pichakun nappes, Neyriz area):

biostratigraphy, facies sedimentology and sequence stratigraphy. In: P. Leturmy and C. Robin (Eds.), Tectonic and Stratigraphic Evolution of Zagros and Makran during the Mesozoic-Cenozoic. Geol. Soc. London Spec. Publ., 330, 179–210.

Salvini, G. and Marcucci Passerini, M., 1998, The radiolarian assemblages of the Bonarelli Horizon in the Umbria-Marche Apennines and Southern Alps, Italy. Cretaceous Res., 19, 777–804.

Sanfilippo, A. and Riedel, W.R., 1985, Cretaceous Radiolaria. Plankton Stratigraphy. In: Bolli, H.M., Saunders, J. B. and Perch-Niel sen, K. (eds), Plank ton Stratigraphy, Cambridge University Press, Cambridge, 573–630.

Schaaf, A. and Thomas, V., 1986, Les Radiolaires campaniens du Wadi Ragmi (nappe de Semail, Oman): un nouveau repère chronologique de l'obduction omanaise. C.R. Acad. Sci. Paris, Série II, 303, 1593–1598.

Schlanger, S.O. and Jenkyns, H.C., 1976, Cretaceous oceanic anoxic events: causes and consequences. Geol. Mijnb., 55, 179–184.

Searle, M.P., Waters, D.J., Garber, J.M., Rioux, M., Cherry, A.G. and Ambrose, T.K., 2015, Structure and metamorphism beneath the obducting Oman ophiolite: Evidence from the Bani Hamid granulites, northern Oman mountains. Geosphere, 11, doi:10.1130/GES01199.1.

Sepkoski Jr, J.J., 1996, Patterns of Phanerozoic extinction: a perspective from global data bases. In Global events and event stratigraphy in the Phanerozoic, 35–51, Springer Berlin Heidelberg.

Sepkoski, J. J., 1989, Periodicity in extinction and the problem of catastrophism in the history of life. Journal of the Geological Society, 146, 7–19.

Sholkovitz, E.R., Landing, W.M., and Lewis, B.L., 1994, Ocean particle chemistry: the fractionation of rare earth elements between suspended particles and seawater. Geochimica et Cosmochimica Acta, 58, 1567–1579.

Snow, L.J., Duncan, R.A., and Bralower, T.J., 2005, Trace element

abundances in the Rock Canyon anticline, Pueblo, Colorado, marine sedimentary section and their relationship to Caribbean plateau construction and oxygen anoxic event 2. Paleoceanography, 20, PA3005,doi:10.1029/2004PA001093.

Svensen, H., Planke, S., Malthe-Sorenssen, A., and Jamtveit, B., 2004, Release of methane from a volcanic basin as a mechanism for initial Eocene global warming. Nature, 429(6991), 542.

Tada, R. and Iijima, A., 1992, Lithostratigraphy and compositional variation of Neogene hemipelagic sediments in the Japan Sea. Proc. ODP Sci. Res. 127/128, 1229–1260.

Tajika, E. and Yamanaka., 2003, Earth system variations during the Cretaceous. Kaseki, 74, 27–35

Tamura, A. and Arai, S., 2006, Harzburgite-dunite-orthopyroxenite suite as a record of supra-subduction zone setting for the Oman ophiolite mantle. Lithos, 90, 43–56.

Taylor, S.R. and McLennan, S.M., 1985, The Continental Crust: Its Composition and Evolution. Blackwell Scientific Publications, Oxford.

Thomson, J., Carpenter, M.S.N., Colley, S., Wilson, T.R.S., Elderfield, H. and Kennedy, H., 1984, Metal accumulation rates in northwest Atlantic pelagic sediments. Geochim. Cosmochim. 48, 1935–1948.

Tilton, G.R., Hopson, C.A. and Wright, J.E., 1981, Uranium-lead isotopic ages of the Samail ophiolite, Oman, with applications to Tethyan ocean ridge tectonics. J. Geophys. Res., 86, 2763–2775.

Tippit, P.R., Pessagno, Jr. E.A. and Smewing, J.D., 1981, The biostratigraphy of sediments in the volcanic unit of the Samail ophiolite. J. Geophys. Res., 86, 2756–2762.

Tsikos, H., Jenkyns, H.C., Walsworth-Bell, B., Petrizzo, M.R., Forster, A., Kolonic, S., Erba, E., Premoli Silva, I., Baas, M., Wagner, T. and Sinninghe Damsté, J.S., 2004, Carbon-isotope stratigraphy recorded by the Cenomanian-Turonian Oceanic Anoxic Event: correlation and

implications based on three key localities. J. Geol. Soc. London, 161, 711–719.

Turgeon, S.C. and Creaser, R.A., 2008, Cretaceous oceanic anoxic event 2 triggered by a massive magmatic episode. Nature, 454(7202), 323.

Umino, S., 2012, Emplacement mechanism of off-axis large submarine lava field from the Oman Ophiolite. J. Geophys. Res., 117, B11210, doi: 10.1029/2012JB009198.

Umino, S., Yanai, S., Jaman, A.R., Nakamura, Y. and Iiyama, J.T., 1990, The transition from spreading to subduction: evidence from the Semail ophiolite, northern Oman mountains. In: J. Malpas, E.M. Moores, A. Panayiotou and C. Xenophontos (Eds.), Ophiolites: Oceanic Crustal Analogues, Proc. Symposium "Troodos 1987". Geol. Surv. Dept., Ministry of Agriculture and Natural Resources, Nicosia, Cyprus, 375–384.

Urquharta, E. and Bannera, F.T., 1994, Biostratigraphy of the supra-ophiolite sediments of the Troodos Massif, Cyprus: the Cretaceous Perapedhi, Kannaviou, Moni and Kathikas formations. Geol. Mag., 131, 499–518.

Wagreich, M., Bojar, A.-V., Sachsenhofer, R.F., Neuhuber, S. and Egger, H., 2008, Calcareous nannoplankton, planktonic foraminiferal, and carbonate carbon isotope stratigraphy of the Cenomanian-Turonian boundary section in the Ultrahelvetic Zone (Eastern Alps, Upper Austria). Cretaceous Res., 29, 965–975.

Warren, C.J., Parrish, R.R., Waters, D.J. and Searle, M.P., 2005, Dating the geologic history of Oman's Semail ophiolite: insights from U-Pb geochronology. Contrib. Mineral. Petrol., 150, 403–422.

Wignall, P.B. and Twitchett, R.J., 1996, Oceanic anoxia and the end Permian mass extinction. Science, 272, 1155–1158.

Wilson, P.A., Norris, R.D. and Cooper, M.J., 2002, Testing the Cretaceous greenhouse hypothesis using glassy foraminiferal calcite from the core of the Turonian tropics on Demerara Rise. Geology, 30(7), 607–610.

Woodcock, N.H. and Robertson, A.H.F., 1982, Stratigraphy of the Mesozoic rocks above the Semail ophiolite, Oman. Geol. Mag., 119, 67–76.

Yamamoto, K., 1987, Geochemical characteristics and depositional environments of cherts and associated rocks in the Franciscan and Shimanto terranes. Sed. Geol., 52, 65–108.

PLATES

Explanation of Plate 1 (E0-370)

Scale=100 µm

1, 2: *Guttacapsa biacuta* (Squinabol)
3: *Guttacapsa gutta* (Squinabol)
4: *Theocampe praevandwrhoofi* (Bragina)
5: *Thanarla pulchra (Squinabol)*
6: *Thanarla vneta* (Squinabol)
7: *Dictyomitra multicostata* Zittel
8: *Pseudodictyomitra pseudomacrocephala* (Squinabol)
9: *Pseudodictyomitra tiara* (Holmes)
10: *Pseudodictyomitra pentacolaensis* Pessagno
11: *Xitus picenus* Salvini and Passerini
12: *Novixitus mclauglini* (Pessagno)
13: *Stichomitra communis* Squinabol
14: *Rhopalosyringium elegans* (Squinabol)
15, 16: *Rhopalosyringium majuroense* Schaaf
17: *Rhopalosyringium* sp. A
18: *Rhopalosyringium euganeum* (Squinabol)
19: *Sethocapsa bossoensis* Salvini and Passerini
20: *Cryptamphorella conara* (Foreman)
21: *Hemicryptocapsa prepolyhedra* Dumitrica
22: *Holocryptocanium astiensis* Pessagno
23: *Holocryptocanium geyserensis* Pessagno
24: *Holocryptocanium tuberculatum* Dumitrica
25: *Sciadiocapsa multiradiata* O'Dogherty
26: *Protoxiphotractus ventosusu* O'Dogherty
27: *Praeconocaryomma universa* Pessagno
28: *Dactyliosphaera silviae* Squinabol
29: *Dactyliodiscus longispinus* (Squinabol)

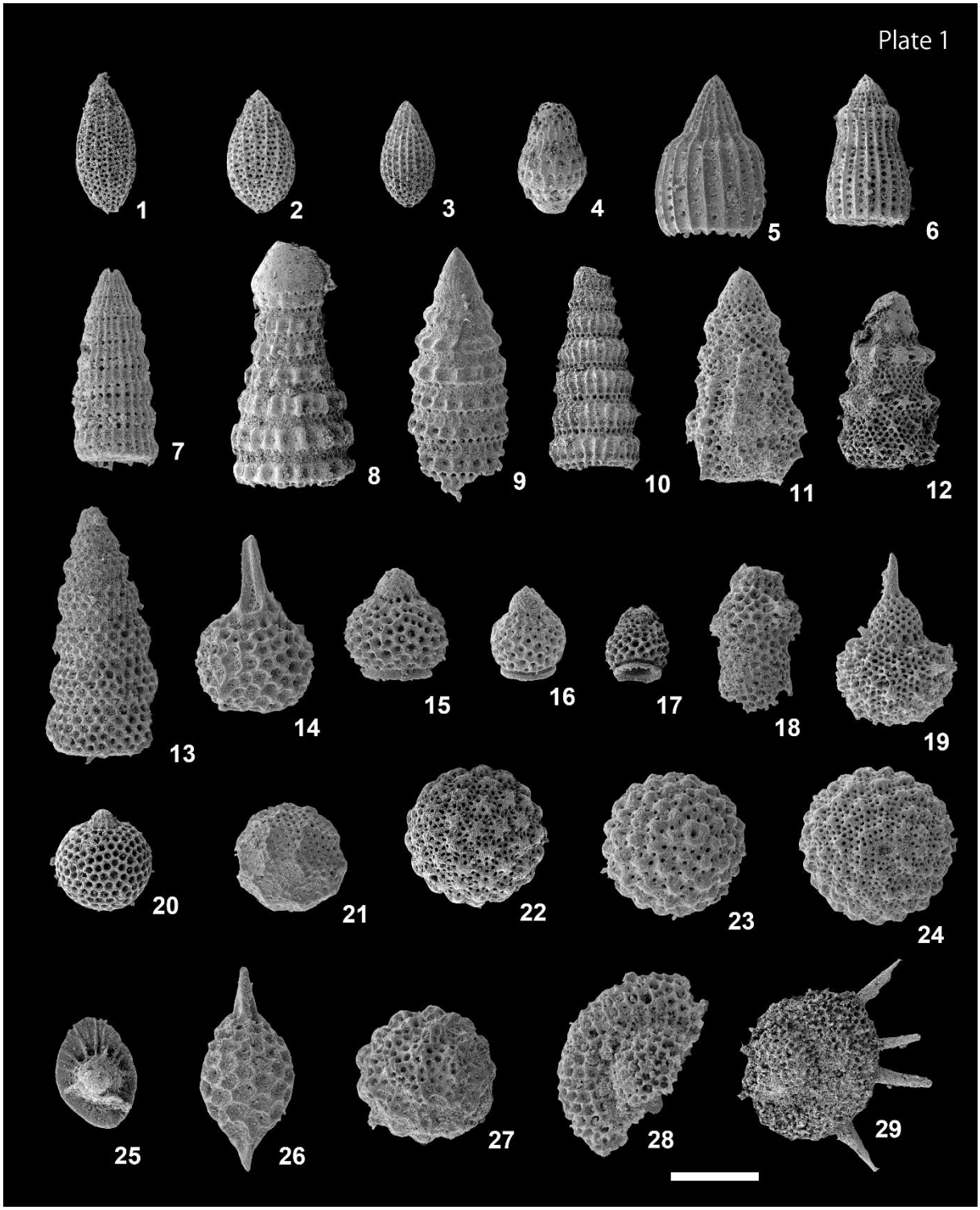
Plate 1
1
2
3
4
5
6
7
8
9
10
11
12
13
14
15
16
17
18
19
20
21
22
23
24
25
26
27
28
29

Explanation of Plate 2 (E0-210)

Scale=100 μm

1, *Guttacapsa gutta* (Squinabol)
2: *Guttacapsa biacuta* (Squinabol)
3: *Guttacapsa* sp. A
4: *Diacanthocapsa antiqua* (Squinabol)
5*: Theocampe praevandwrhoofi* (Bragina)
6: *Thanarla pulchra (Squinabol)*
7: *Thanarla vneta* (Squinabol)
8: *Dictyomitra multicostata* Zittel
9: *Pseudodictyomitra pseudomacrocephala* (Squinabol)
10: *Pseudodictyomitra tiara* (Holmes)
11: *Novixitus mclauglini* (Pessagno)
12: *Stichomitra communis* Squinabol
13: *Rhopalosyringium elegans* (Squinabol)
14: *Rhopalosyringium majuroense* Schaaf
15: *Rhopalosyringium hispidum* O'Dogherty
16: *Rhopalosyringium petilum* (Foreman)
17: *Sethocapsa bossoensis* Salvini and Passerini
18: *Squinabollum fossil*e (Squinabol)
19: *Cryptamphorella conara* (Foreman)
20: *Hemicryptocapsa prepolyhedra* Dumitrica
21: *Hemicryptocapsa tuberosa* Dumitrica
22: *Holocryptocanium geyserensis* Pessagno
23: *Holocryptocanium tuberculatum* Dumitrica
24: *Holocryptocanium barbui* Dumitrica
25: *Holocryptocanium* sp. A
26: *Gongylothorax prunum* Dumitrica
27: *Praeconocaryomma universa* Pessagno
28: *Dactyliosphaera silviae* Squinabol

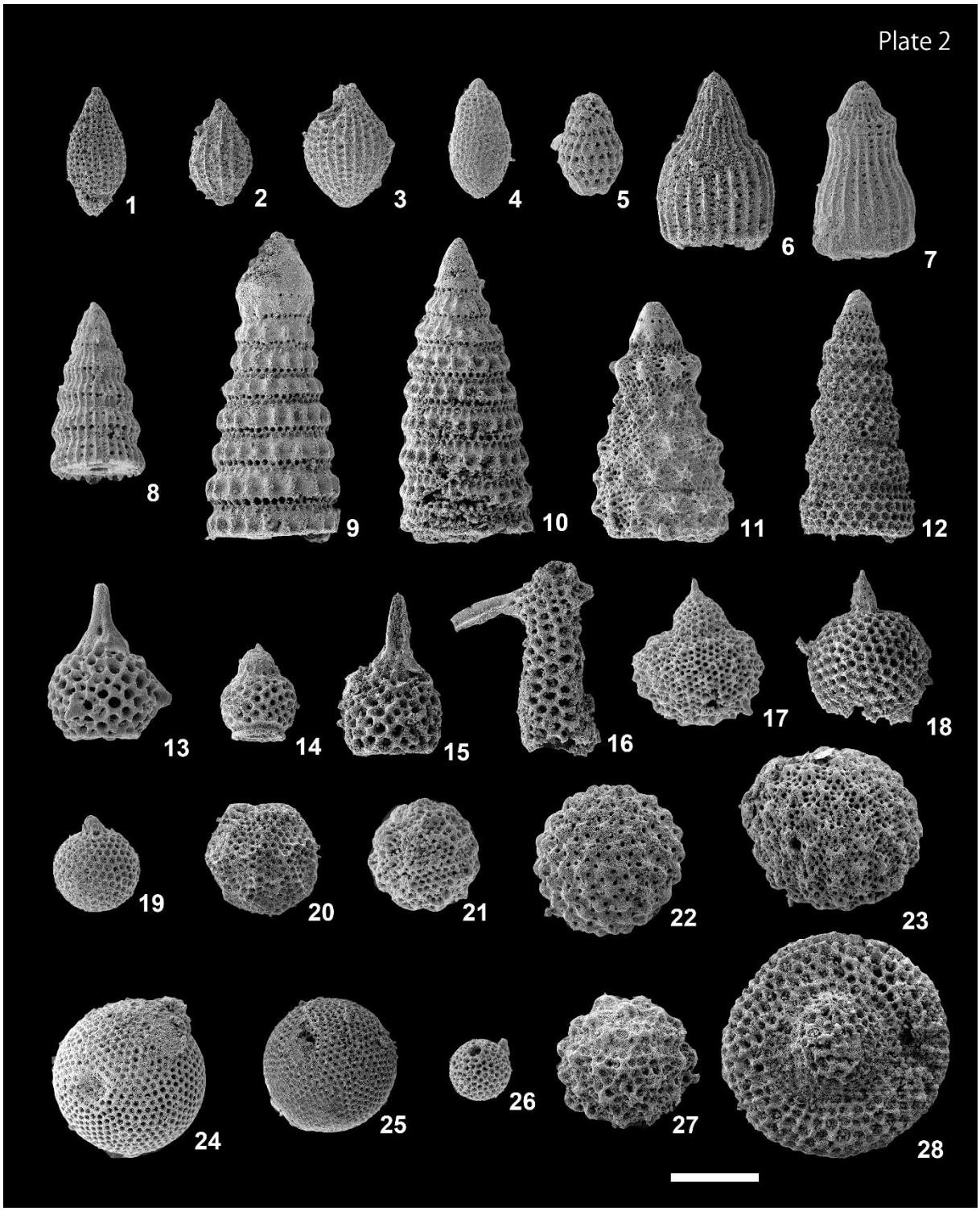
Plate 2
1
2
3
4
5
6
7
8
9
10
11
12
13
14
15
16
17
18
19
20
21
22
23
24
25
26
27
28

Explanation of Plate 3 (E0-40)

Scale=100 μm
Scale A: 1-27. Scale B: 28.

1: *Guttacapsa biacuta* (Squinabol)
2: *Theocampe praevandwrhoofi* (Bragina)
3: *Thanarla vneta* (Squinabol)
4: *Thanarla brouweri* (Tan)
5: *Dictyomitra formosa* (Squinabol)
6: *Dictyomitra multicostata* Zittel
7: *Pseudodictyomitra pseudomacrocephala* (Squinabol)
8: *Pseudodictyomitra tiara* (Holmes)
9: *Pseudodictyomitra quasilodogaensis* Pessagno
10: *Pseudodictyomitra pentacolaensis* Pessagno
11: *Xitus plenus* Pessagno
12: *Xitus picenus* Salvini and Passerini
13: *Novixitus mclauglini* (Pessagno)
14: *Stichomitra communis* Squinabol
15: *Rhopalosyringium elegans* (Squinabol)
16: *Rhopalosyringium majuroense* Schaaf
17: *Rhopalosyringium hispidum* O'Dogherty
18: *Rhopalosyringium petilum* (Foreman)
19: *Rhopalosyringium adriaticum* O'Doghert
20: *Myllocercion* sp. A
21: *Cryptamphorella conara* (Foreman)
22: *Hemicryptocapsa prepolyhedra* Dumitrica
23: *Hemicryptocapsa polyhedra* Dumitrica
24: *Holocryptocanium geyserensis Pessagno*
25: *Holocryptocanium barbui* Dumitrica
26: *Holocryptocanium tuberculatum* Dumitrica
27: *Becus horridus* (Squinabol)
28: *Dactyliosphaera silviae* Squinabol
29: *Alievium superbum* (Squinabol)

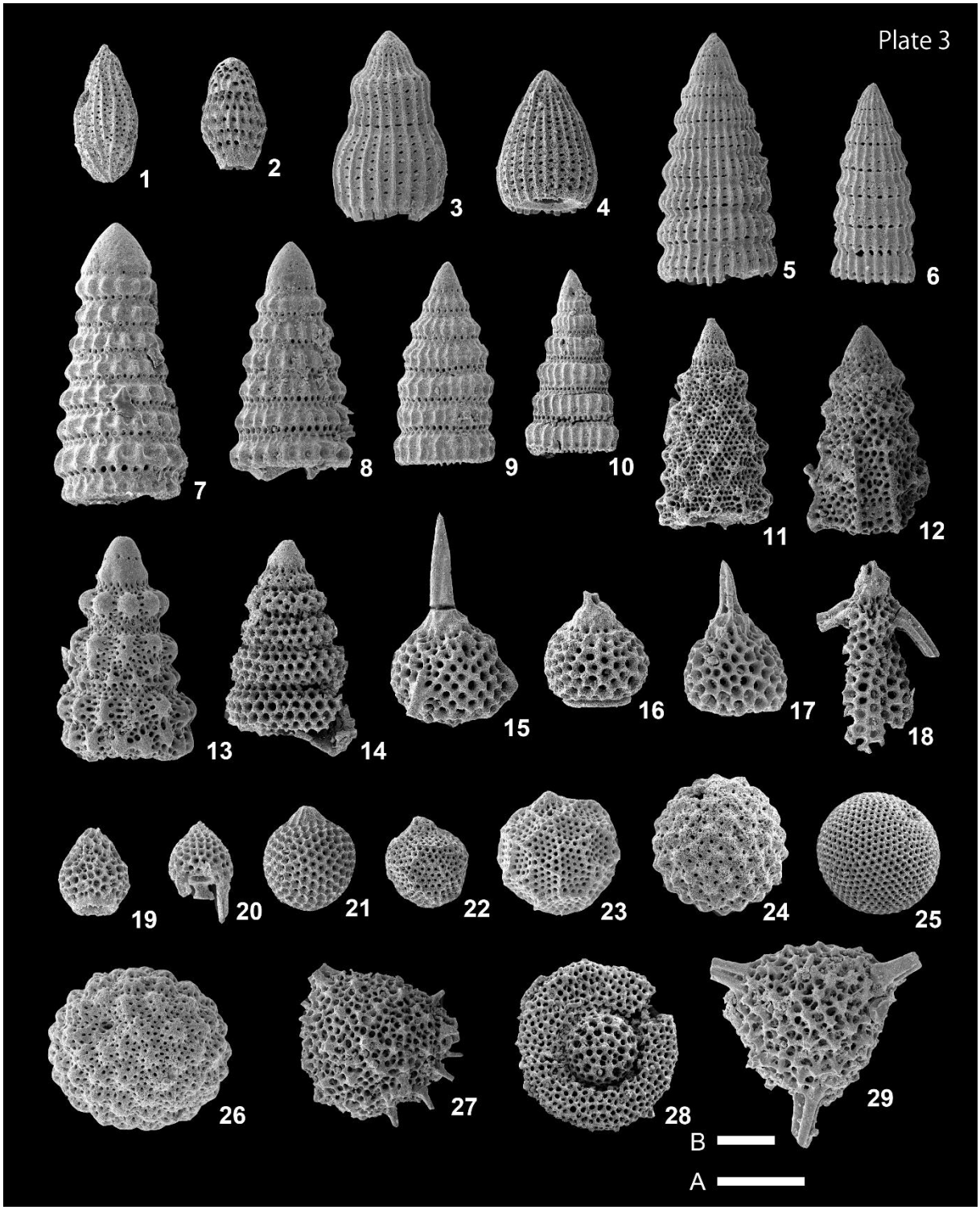
Plate 3
1
2
3
4
5
6
7
8
9
10
11
12
13
14
15
16
17
18
19
20
21
22
23
24
25
26
27
28
29
B
A

Explanation of Plate 4 (E-02)

Scale=100 μm

1: *Guttacapsa biacuta* (Squinabol)
2: *Guttacapsa gutta* (Squinabol)
3, 4: *Thanarla pulchra (Squinabol)*
5: *Dictyomitra montisserei* (Squinabol)
6: *Dictyomitra naparnsis Pessagno*
7: *Mita gracilis (Squinabol)*
8: *Pseudodictyomitra pentacolaensis* Pessagno
9: *Xitus plenus* Pessagno
10: *Stichomitra communis* Squinabol
11: *Stichomitra sroki* (Campbell and Clark)
12, 13: *Rhopalosyringium majuroense* Schaaf
14: *Rhopalosyringium elegans* (Squinabol)
15,16: *Rhopalosyringium* sp. A
17: *Rhopalosyringium petilum* (Foreman)
18: *Myllocercion* sp. A
19: *Sethocapsa bossoensis* Salvini and Passerini
20: *Cryptamphorella conara* (Foreman)
21: *Hemicryptocapsa tuberosa* Dumitrica
22: *Holocryptocanium tuberculatum* Dumitrica
23: *Alievium superbum* (Squinabol)

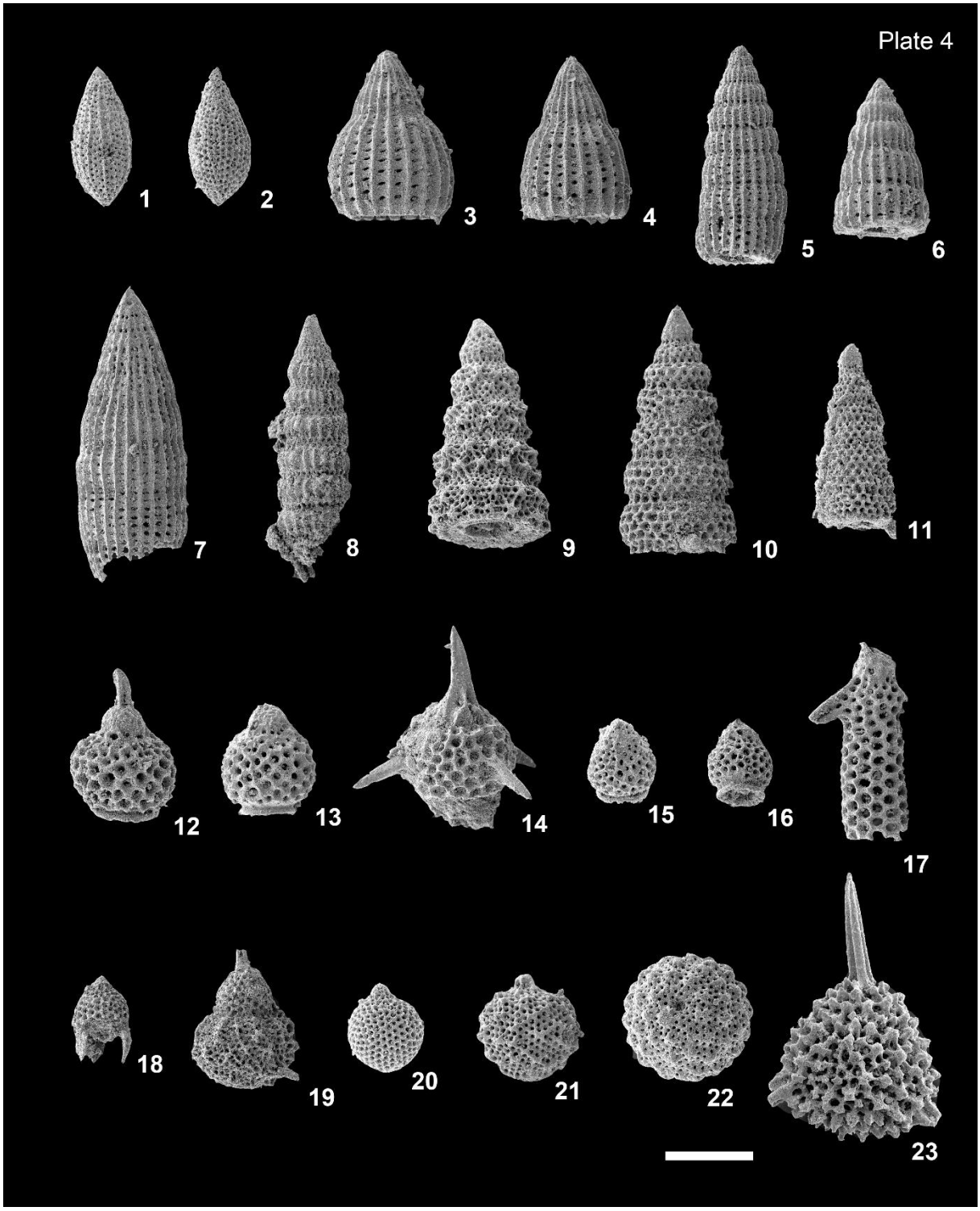
Plate 4
1
2
3
4
5
6
7
8
9
10
11
12
13
14
15
16
17
18
19
20
21
22
23

Explanation of Plate 5 (E-03)

Scale=100 μm

1, 2: *Guttacapsa biacuta* (Squinabol)
3: *Guttacapsa gutta* (Squinabol)
4: *Guttacapsa* sp. B
5: *Guttacapsa* sp. A
6: *Thanarla* sp. A
7: *Diacanthocapsa antiqua* (Squinabol)
8: *Theocampe ascalia* Foreman
9: *Pseudotheocampe* sp.
10: *Dictyomitra naparnsis Pessagno*
11: *Archaeodictyomitra simplex* Pessagno
12: *Xitus picenus* Salvini and Passerini
13: *Stichomitra communis* Squinabol
14, 15: *Rhopalosyringium majuroense* Schaaf
16, 17: *Rhopalosyringium petilum* (Foreman)
18: *Rhopalosyringium* sp. A
19: *Myllocercion* sp. A
20: *Cryptamphorella conara* (Foreman)
21: *Hemicryptocapsa tuberosa* Dumitrica
22: *Squinabollum fossil*e (Squinabol)
23: *Dicroa rara* (Squinabol)
24: *Acaeniotyle rebellis* O'dogherty
25: *Dactyliosphaera silviae* Squinabol
26: *Acanthocircus multidentatus* (Squinabol)

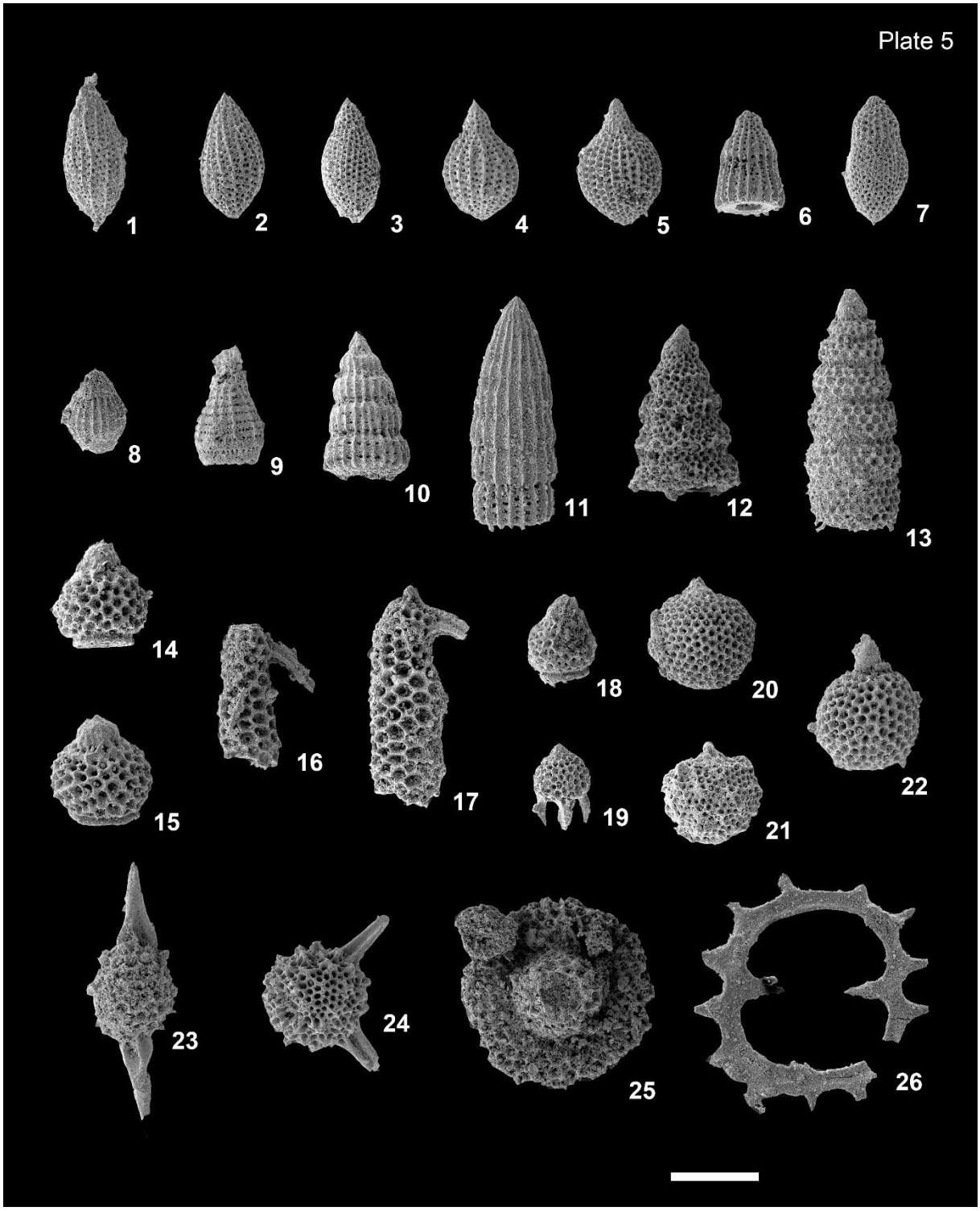
Plate 5
1
2
3
4
5
6
7
8
9
10
11
12
13
14
15
16
17
18
19
20
21
22
23
24
25
26

Explanation of Plate 6 (E-03.5b)

Scale=100 µm
Scale A: 1-26, 23. Scale B: 28. Scale C: 27.

1: *Guttacapsa gutta* (Squinabol)
2: *Guttacapsa* sp. A
3: *Diacanthocapsa antiqua* (Squinabol)
4: *Theocampe ascalia* Foreman
5: *Pseudodictyomitra pseudomacrocephala* (Squinabol)
6: *Xitus picenus* Salvini and Passerini
7: *Stichomitra communis* Squinabol
8: *Rhopalosyringium elegans* (Squinabol)
9, 10: *Rhopalosyringium* sp. A
11: *Rhopalosyringium hispidum* O'Dogherty
12, 13: *Rhopalosyringium adriaticum* O'Doghert
14: *Cryptamphorella conara* (Foreman)
15: *Hemicryptocapsa tuberosa* Dumitrica
16, 17: *Hemicryptocapsa prepolyhedra* Dumitrica
18, 19: *Hemicryptocapsa polyhedra* Dumitrica
20, 21: *Holocryptocanium astiensis* Pessagno
22: *Holocryptocanium* sp. A
23: *Archaeocenosphaera* ? *Mellifera* O'Dogherty
24: *Squinabollum fossil*e (Squinabol)
25: *Sciadiocapsa multiradiata* O'Dogherty
26: *Archaeospongoprunum hueyi* Pessagno
27: *Pessagnobrachia clavata* (Squinabol)
28: *Acanthocircus venetus* (Squinabol)

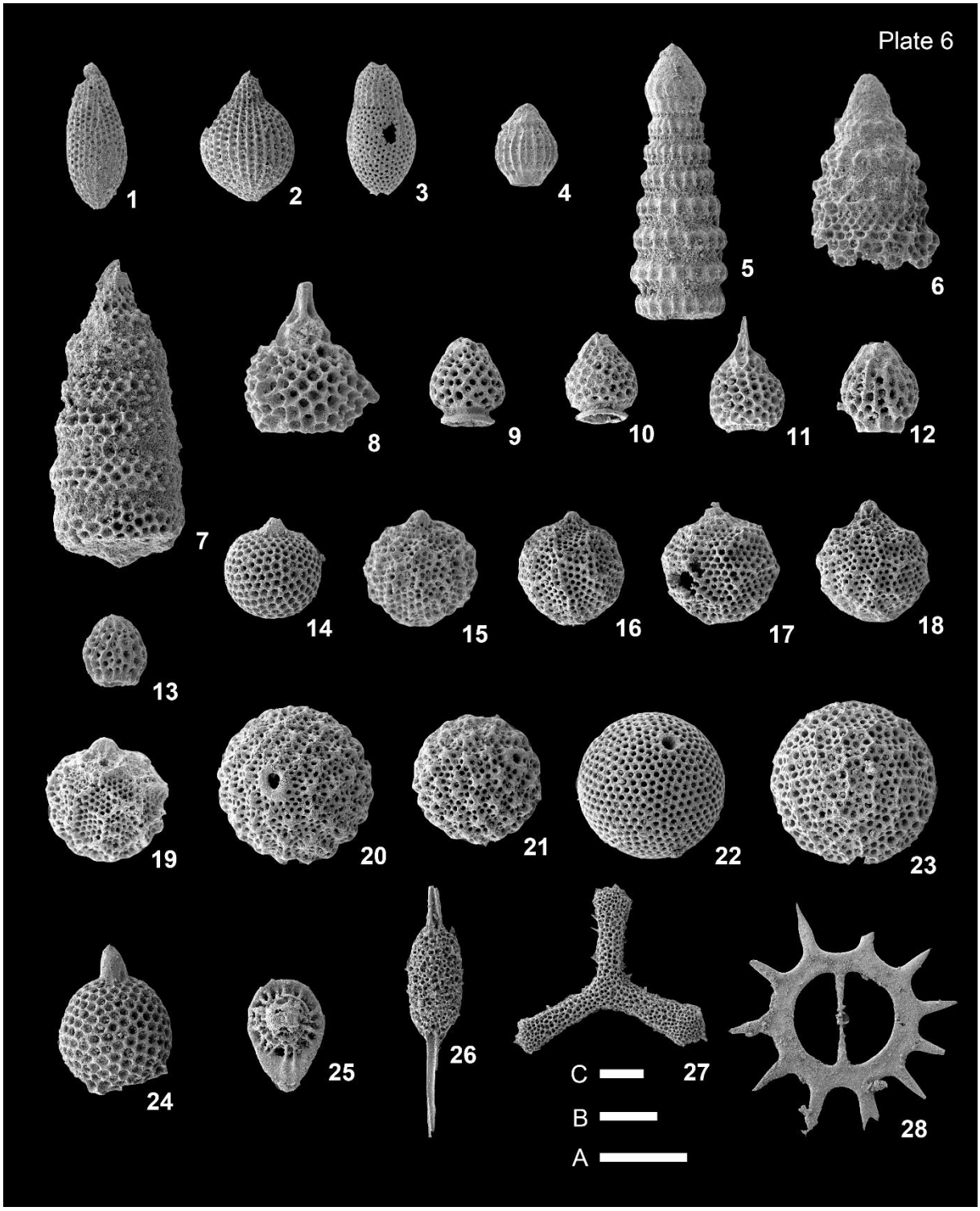
Plate 6
1
2
3
4
5
6
7
8
9
10
11
12
13
14
15
16
17
18
19
20
21
22
23
24
25
26
27
28
C
B
A

Explanation of Plate 7 (E-03.5c)

Scale=100 µm

1: *Guttacapsa gutta* (Squinabol)
2: *Guttacapsa* sp. A
3: *Diacanthocapsa antiqua* (Squinabol)
4: *Diacanthocapsa ancus* (Foreman)
4: *Theocampe ascalia* Foreman
6: *Dictyomitra densicostata* Pessagno
7: *Dictyomitra multicostata* Zittel
8: *Pseudodictyomitra tiara* (Holmes)
9: *Pseudodictyomitra pseudomacrocephala* (Squinabol)
10: *Novixitus mclauglini* (Pessagno)
11: *Xitus picenus* Salvini and Passerini
12: *Rhopalosyringium elegans* (Squinabol)
13: *Rhopalosyringium* sp. A
14: *Rhopalosyringium hispidum* O'Dogherty
15: *Rhopalosyringium adriaticum* O'Doghert
16: *Rhopalosyringium radiosum* O'Dogherty
17: *Cryptamphorella conara* (Foreman)
18: *Hemicryptocapsa tuberosa* Dumitrica
19, 20: *Hemicryptocapsa prepolyhedra* Dumitrica
21: *Hemicryptocapsa polyhedra* Dumitrica
22: *Holocryptocanium* sp. A
23: *Holocryptocanium tuberculatum* Dumitrica
24: *Holocryptocanium astiensis* Pessagno
25: *Sethocapsa bossoensis* Salvini and Passerini
26: *Archaeocenosphaera* ? *Mellifera* O'Dogherty
27: *Archaeospongoprunum hueyi* Pessagno
28: *Triactoma cellulosa* Foreman

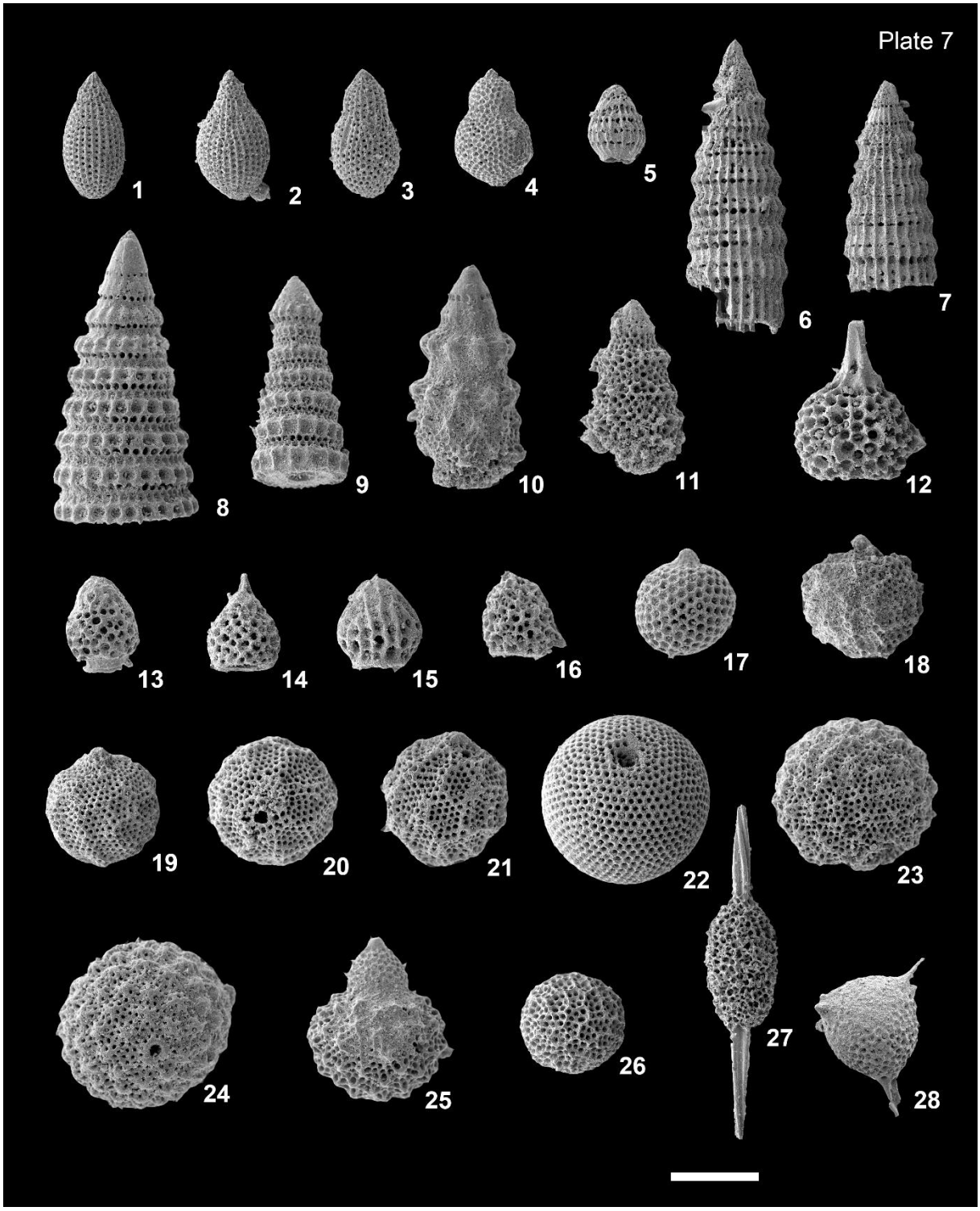
Plate 7
1
2
3
4
5
6
7
8
9
10
11
12
13
14
15
16
17
18
19
20
21
22
23
24
25
26
27
28

Explanation of Plate 8 (E-03.5d)

Scale=100 µm

1: *Guttacapsa gutta* (Squinabol)
2: *Guttacapsa* sp. A
3: *Diacanthocapsa antiqua* (Squinabol)
4: *Thanarla vneta* (Squinabol)
5: *Dictyomitra densicostata* Pessagno
6: *Dictyomitra multicostata* Zittel
7: *Archaeodictyomitra simplex* Pessagno
8: *Pseudodictyomitra pseudomacrocephala* (Squinabol)
9: *Pseudodictyomitra pentacolaensis* Pessagno
10: *Xitus picenus* Salvini and Passerini
11: *Rhopalosyringium elegans* (Squinabol)
12, 13: *Rhopalosyringium adriaticum* O'Doghert
14: *Rhopalosyringium radiosum* O'Dogherty
15, 16: *Rhopalosyringium* sp. A
17: *Sethocapsa bossoensis* Salvini and Passerini
18: *Cryptamphorella conara* (Foreman)
19, 20: *Hemicryptocapsa prepolyhedra* Dumitrica
21. 22: *Hemicryptocapsa polyhedra* Dumitrica
23, 24: *Holocryptocanium astiensis* Pessagno
25: *Holocryptocanium* sp. A
26: *Triactoma cellulosa* Foreman

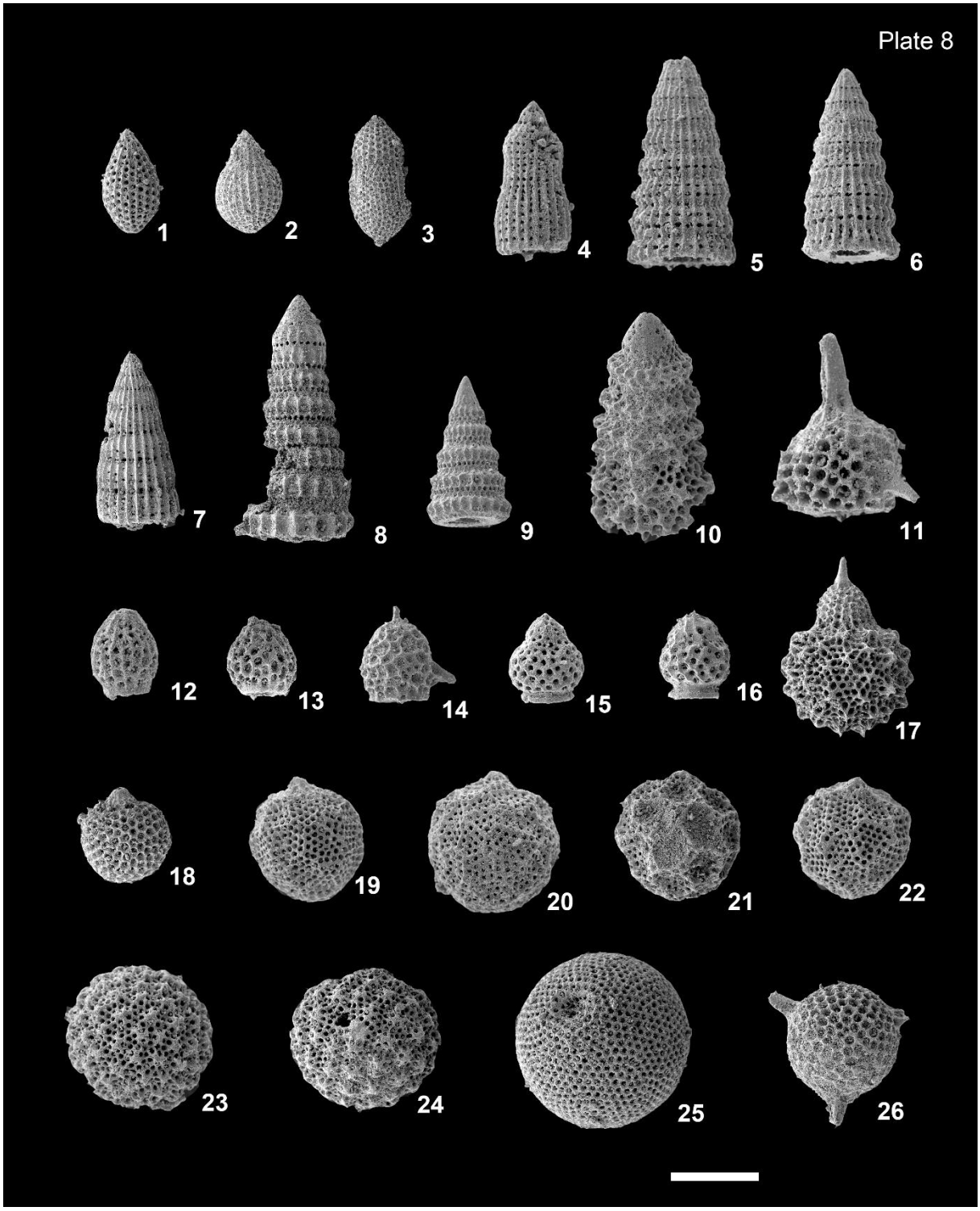
Plate 8
1
2
3
4
5
6
7
8
9
10
11
12
13
14
15
16
17
18
19
20
21
22
23
24
25
26

Explanation of Plate 9 (E-03.5e)

Scale=100 µm
Scale A: 1-20, 23. Scale B: 21, 22.

1, 2: *Dictyomitra densicostata* Pessagno
3: *Pseudodictyomitra pentacolaensis* Pessagno
4: *Sandovalella telum* (O'Dogherty)
5, 6, 7: *Rhopalosyringium scissum* O'Dogherty
8, 9: *Rhopalosyringium hispidum* O'Dogherty
10: *Rhopalosyringium radiosum* O'Dogherty
11: *Rhopalosyringium adriaticum* O'Doghert
12: *Cryptamphorella conara* (Foreman)
13: *Hemicryptocapsa simplex* Dumitrica
14: *Archaeocenosphaera* ? *Mellifera* O'Dogherty
15: *Cornutella cretacea* Taketani
16: *Sciadiocapsa radiata* (Squinabol)
17: *Sciadiocapsa multiradiata* O'Dogherty
18: *Praeconocaryomma californiaensis* Pessagno
19: *Acaeniotyle rebellis* O'dogherty
20: *Tetracanthellipsis gregalis* O'dogherty
21: *Archaeospongoprunum hueyi Pessagno*
22: *Acanthocircus hueyi* (Pessagno)
23: *Crucella euganea* (Squinabol)

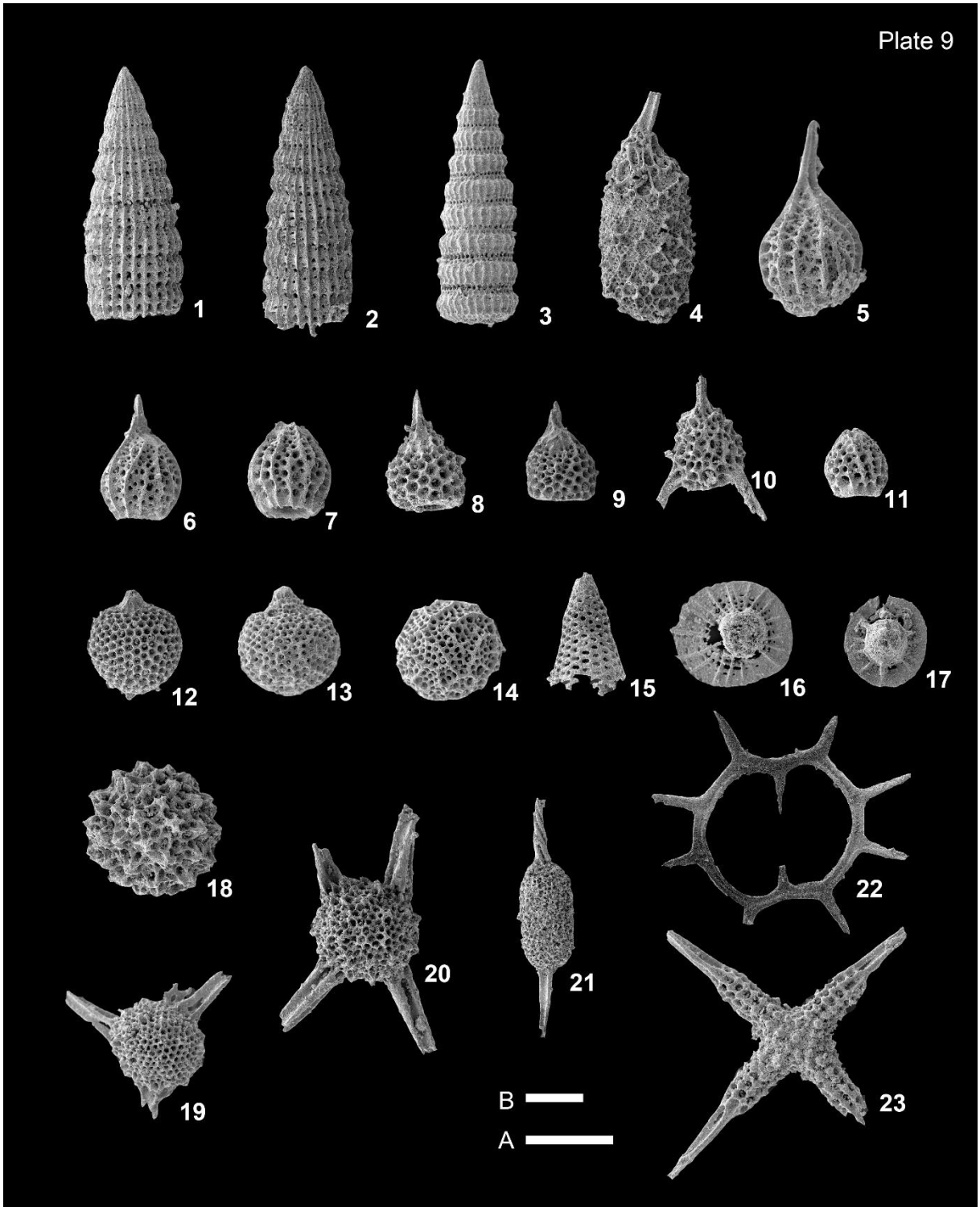
Plate 9
1
2
3
4
5
6
7
8
9
10
11
12
13
14
15
16
17
18
19
20
21
22
23
B
A

Explanation of Plate 10 (E-03.5f)

Scale=100 µm
Scale A: 1-20, 23. Scale B: 21, 22.

1: *Diacanthocapsa elongata* Bragina
2: *Diacanthocapsa ovoidea* Dumitrica
3: *Diacanthocapsa* sp.
4, 5: *Theocampe ascalia* Foreman
6, 7: *Dictyomitra densicostata* Pessagno
8: *Sandovalella hastatus* (O'Dogherty)
9, 10, 11: *Rhopalosyringium scissum* O'Dogherty
12, 13: *Rhopalosyringium hispidum* O'Dogherty
14: *Rhopalosyringium radiosum* O'Dogherty
15: *Rhopalosyringium adriaticum* O'Doghert
16: *Cryptamphorella conara* (Foreman)
13: *Hemicryptocapsa simplex* Dumitrica
14: *Archaeocenosphaera* ? *Mellifera* O'Dogherty
15: *Cornutella cretacea* Taketani
16: *Sciadiocapsa radiata* (Squinabol)
17: *Hemicryptocapsa tuberosa* Dumitrica
18: *Annikaella* sp. B
19: *Vitorfus morini* Empson-Morin
20: *Alievium superbum* (Squinabol)
21: *Acaeniotyle* sp. A
22: *Triactoma* sp. A
23: *Tetracanthellipsis gregalis O'dogherty*

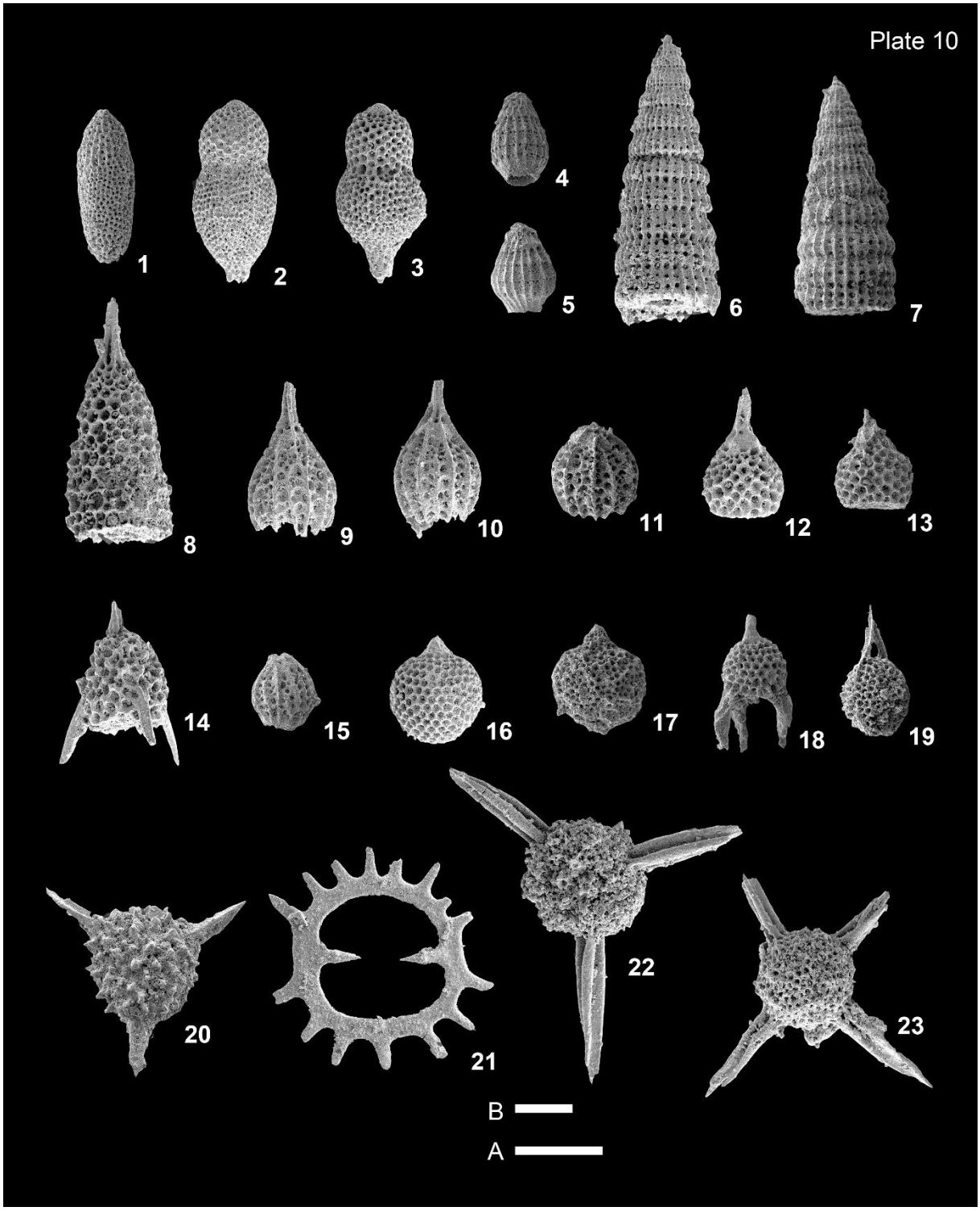
Plate 10
1
2
3
4
5
6
7
8
9
10
11
12
13
14
15
16
17
18
19
20
21
22
23
B
A

Explanation of Plate 11 (E-05)

Scale=100 μm
Scale A: 1-19, 21-24. Scale B: 20.

1, 2: *Dictyomitra densicostata* Pessagno
3, 4: *Sandovalella telum* (O'Dogherty)
5, 6: *Sandovalella hastatus* (O'Dogherty)
7: *Stichomitra communis* Squinabol
8, 9:*Rhopalosyringium scissum* O'Dogherty
10: *Rhopalosyringium hispidum* O'Dogherty
11: *Rhopalosyringium radiosum* O'Dogherty
12: *Rhopalosyringium adriaticum* O'Doghert
14, 15:*Pseudotheocampe tina* Foreman
16: *Cryptamphorella conara* (Foreman)
17: *Holocryptocanium barbui* Dumitrica
18: *Archaeocenosphaera* ? *Mellifera* O'Dogherty
19: *Quinquecapsularia pahacea* O'Dogherty
20: *Triactoma* sp. B
21: *Tetracanthellipsis gregalis O'dogherty*
22: *Crucella cachensis* Pessagno
23: *Crucella euganea* (Squinabol)
24: *Patellula verteroensis* Pessagno

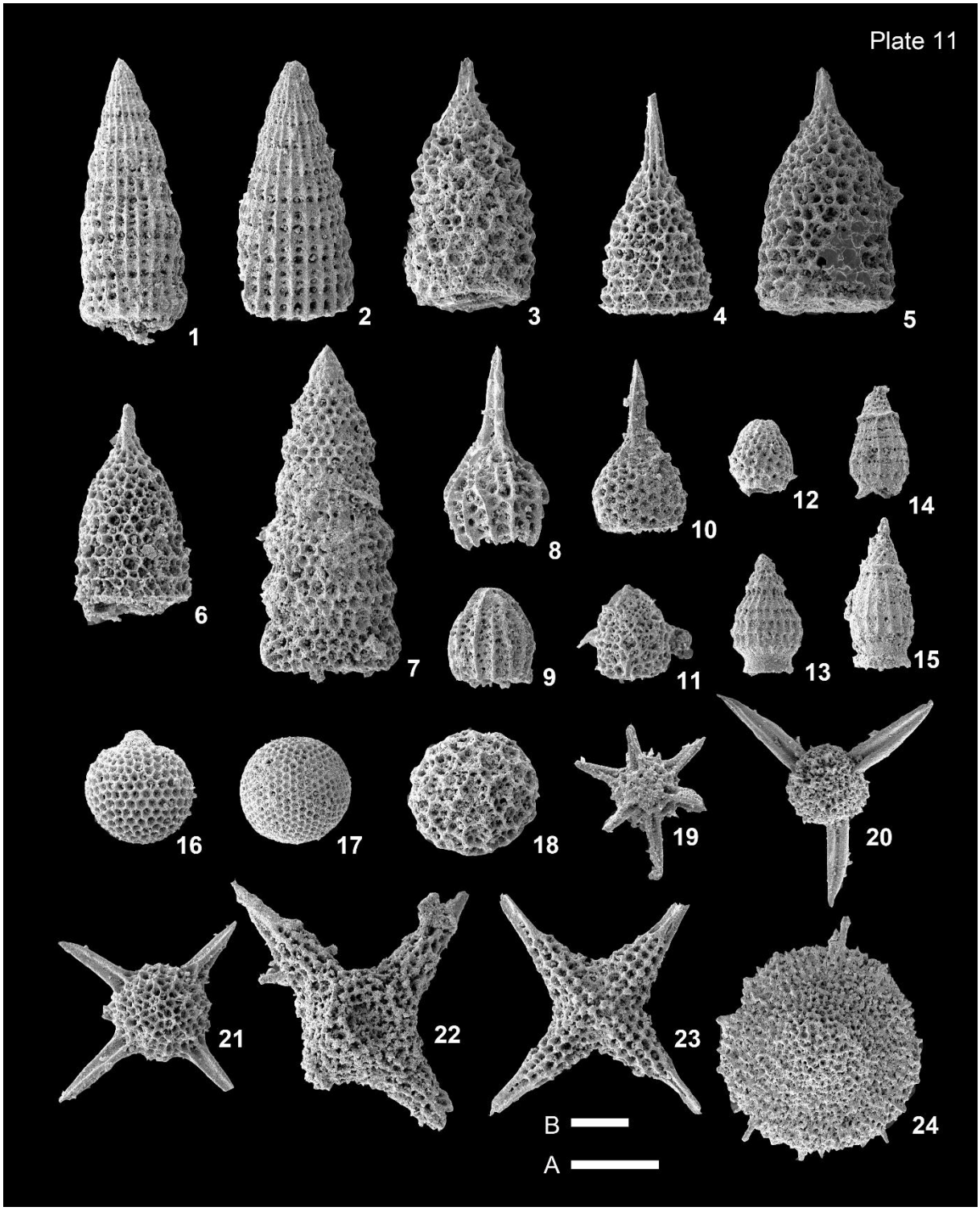
Plate 11
1
2
3
4
5
6
7
8
9
10
11
12
13
14
15
16
17
18
19
20
21
22
23
24
B
A

Explanation of Plate 12 (E-07)

Scale=100 µm
Scale A: 1-20. Scale B: 21.

1, 2: *Dictyomitra densicostata* Pessagno
3: *Stichomitra communis* Squinabol
4: *Xitus plenus* Pessagno
5, 6: *Eostichomitra* sp. A
7, 8:*Rhopalosyringium scissum* O'Dogherty
9, 10: *Rhopalosyringium hispidum* O'Dogherty
11: *Rhopalosyringium adriaticum* O'Doghert
12: *Rhopalosyringium* sp. B
13: *Rhopalosyringium elegans* (Squinabol)
14, 15:*Pseudotheocampe tina* Foreman
16: *Diacanthocapsa ovoidea* Dumitrica
17: *Hemicryptocapsa polyhedra* Dumitrica
18: *Holocryptocanium barbui* Dumitrica
18: *Archaeocenosphaera* ? *Mellifera* O'Dogherty
19: *Triactoma hexeris* O'Dogherty
20: *Praeconocaryomma californiaensis* Pessagno
21: *Acanthocircus hueyi* (Pessagno)

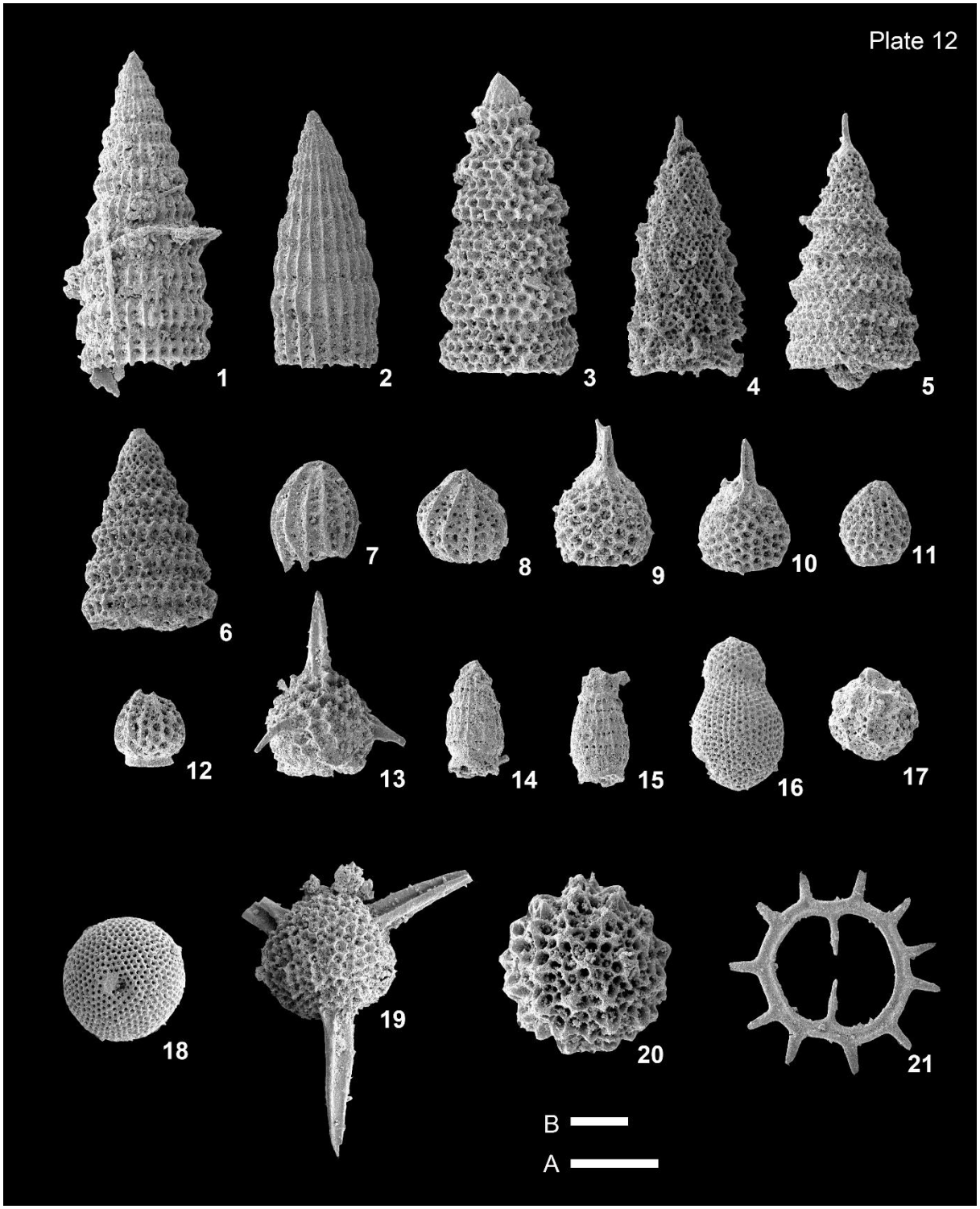
Plate 12
1
2
3
4
5
6
7
8
9
10
11
12
13
14
15
16
17
18
19
20
21
B
A

Explanation of Plate 13 (C-03)

Scale=100 μm

Scale A: 1-23, 25. Scale B: 26. Scale C: 24

1, 2: *Dictyomitra densicostata* Pessagno
3: *Dictyomitra formosa* (Squinabol)
4: *Stichomitra communis* Squinabol
5: *Pseudodictyomitra* sp. A
6: *Eostichomitra* sp. A
7, 8: *Stichomitra manifesta* Foreman
9, 10: *Rhopalosyringium hispidum* O'Dogherty
11, 12: *Rhopalosyringium scissum* O'Dogherty
13: *Rhopalosyringium adriaticum* O'Doghert
14: *Rhopalosyringium* sp. B
13: *Rhopalosyringium elegans* (Squinabol)
15, 16: *Pseudotheocampe tina* Foreman
16: *Diacanthocapsa ovoidea* Dumitrica
17: *Diacanthocapsa ancus* (Foreman)
18: *Diacanthocapsa ovoidea* Dumitrica
19: *Holocryptocanium barbui* Dumitrica
20, 21: *Sciadiocapsa multiradiata* O'Dogherty
22: *Cornutella cretacea* Taketani
23: *Hemicryptocapsa* sp. A
24: *Sciadiocapsa monticelloensis* (Pessagno)
25: *Praeconocaryomma universa* Pessagno
26: *Triactoma hexeris* O'Dogherty

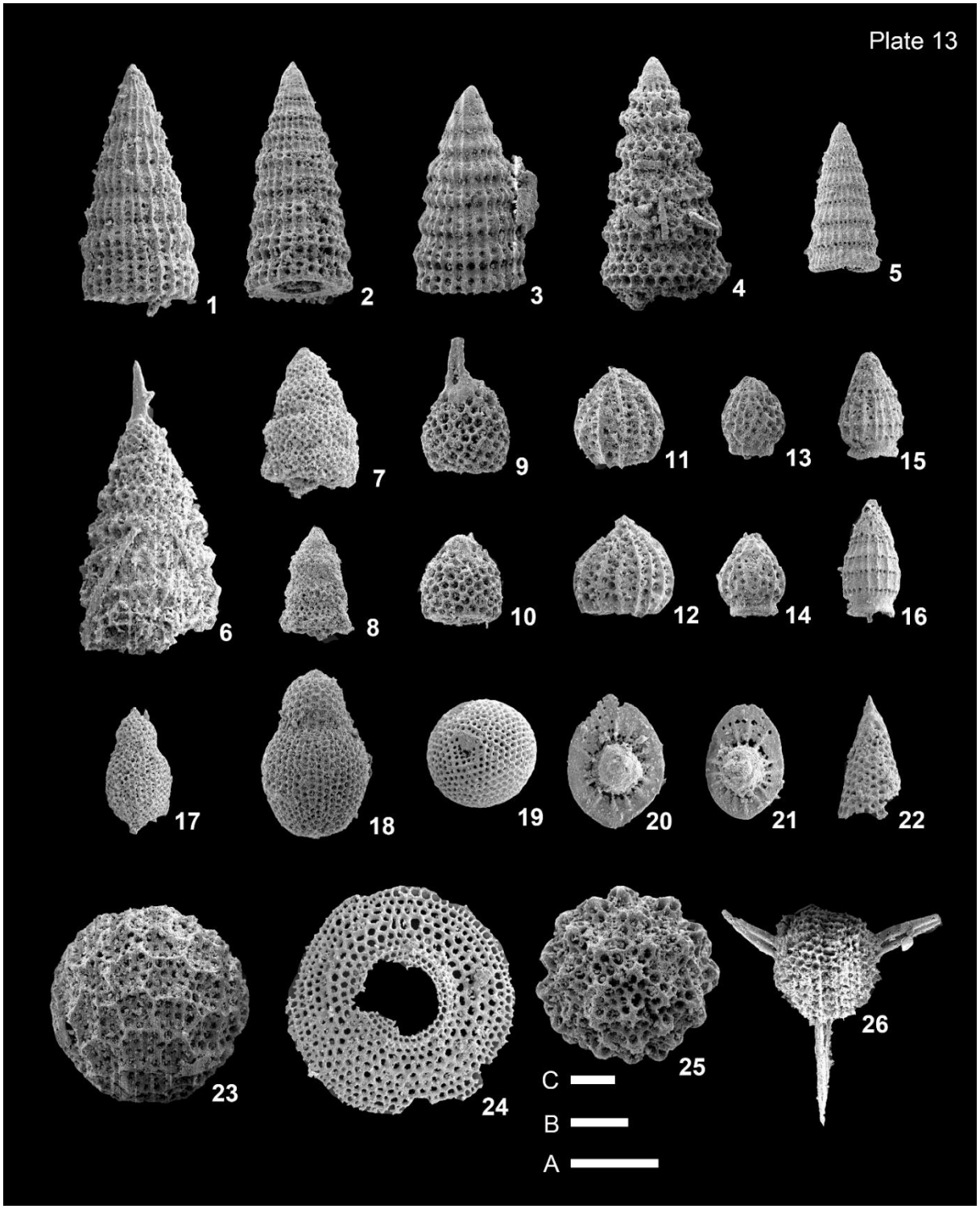
Plate 13
1
2
3
4
5
6
7
8
9
10
11
12
13
14
15
16
17
18
19
20
21
22
23
24
25
26
C
B
A

Explanation of Plate 14 (E-11)

Scale=100 μm
Scale A: 1-3, 5-20. Scale B: 4, 21.

1, 2: *Dictyomitra densicostata* Pessagno
3: *Archaeodictyomitra simplex* Pessagno
4: *Pseudodictyomitra tiara* (Holmes)
5, 6: *Stichomitra* sp. A
7: *Stichomitra manifesta* Foreman
8: *Eostichomitra* sp. A
9: *Xitus plenus* Pessagno
10: *Rhopalosyringium hispidum* O'Dogherty
11, 12: *Rhopalosyringium scissum* O'Dogherty
13: *Rhopalosyringium* sp. B
14: *Rhopalosyringium elegans* (Squinabol)
15, 16: *Pseudotheocampe tina* Foreman
16: *Diacanthocapsa ovoidea* Dumitrica
17: *Gongylothorax prunum* Dumitrica
18: *Archeocenosphaera euganea* (Squinabol)
19: *Praeconocaryomma californiaensis* Pessagno
20: *Archaeospongoprunum cortinaensis* Pessagno
21: *Alievium superbum* (Squinabol)

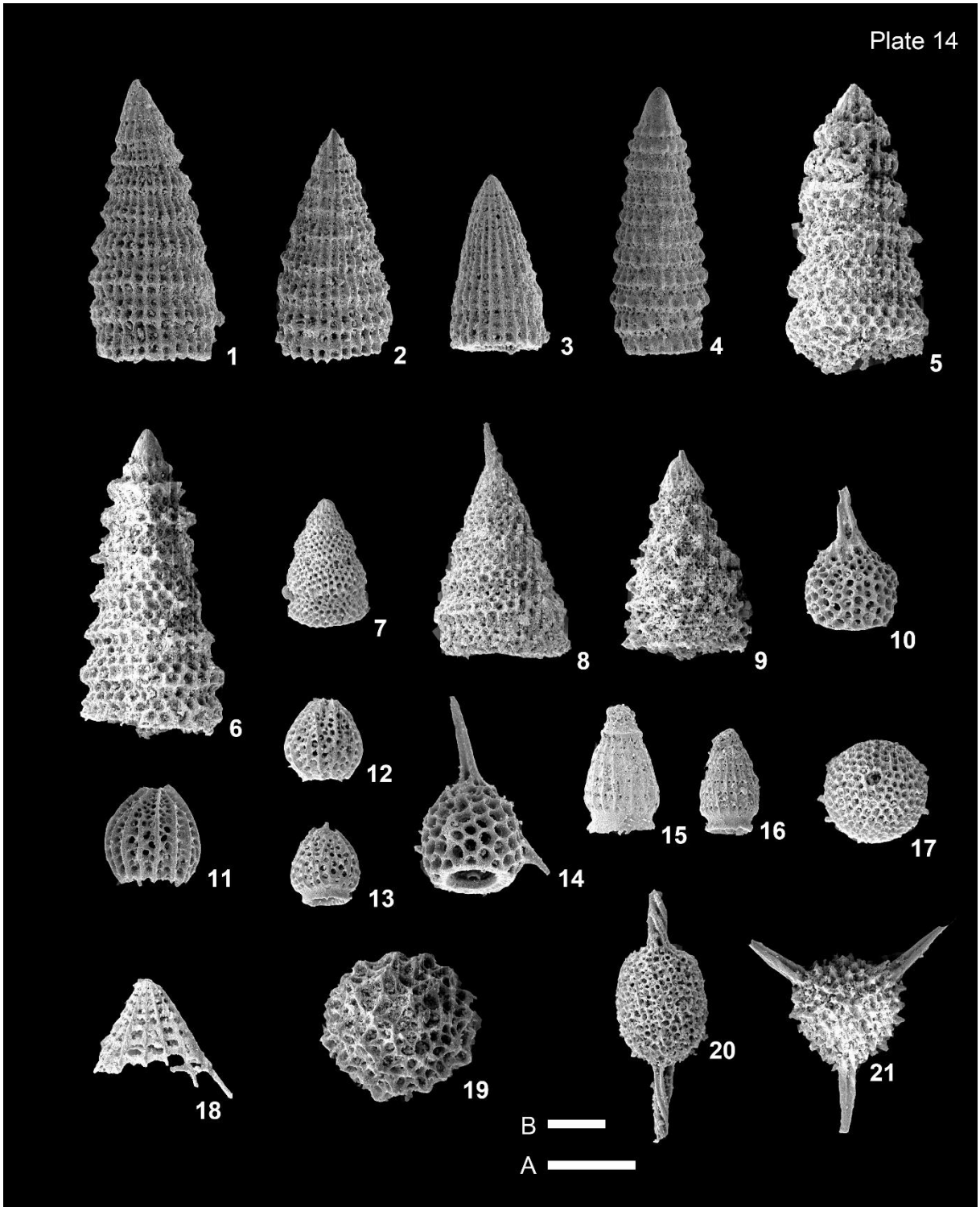
Plate 14
1
2
3
4
5
6
7
8
9
10
11
12
13
14
15
16
17
18
19
20
21
B
A

Explanation of Plate 15 (E-12)

Scale=100 µm
Scale A: 1, 2, 4-22, 24. Scale B: 3, 23.

1: *Dictyomitra formosa (Squinabol)*
2: *Dictyomitra multicostata* Zittel
3: *Pseudodictyomitra tiara* (Holmes)
4: *Stichomitra* sp. A
5: *Stichomitra manifesta* Foreman
6: *Foremanina schona* Empson-Morin
7: *Xitus plenus* Pessagno
9, 10: *Rhopalosyringium scissum* O'Dogherty
11: *Rhopalosyringium* sp. B
12: *Annikaella omanensis* De Wever, Bourdillon-de Grissac, and Beurrier
13: *Myllocercion valgus* (De Wever, Bourdillon-de Grissac, and Beurrier)
14: *Pseudotheocampe tina* Foreman
15: *Sciadiocapsa multiradiata* O'Dogherty
16: *Hemicryptocapsa polyhedra* Dumitrica
17: *Praeconocaryomma californiaensis* Pessagno
18: *Praeconocaryomma universa* Pessagno
19: *Praeconocaryomma lipmanae* Pessagno
20: *Acaeniotyle starka* Empson-Morin
21: *Archaeospongoprunum bipartitum* Pessagno
22: *Alievium superbum* (Squinabol)
23: *Patellula euessceei* Empson-Morin
24: *Patellula verteroensis* Pessagno

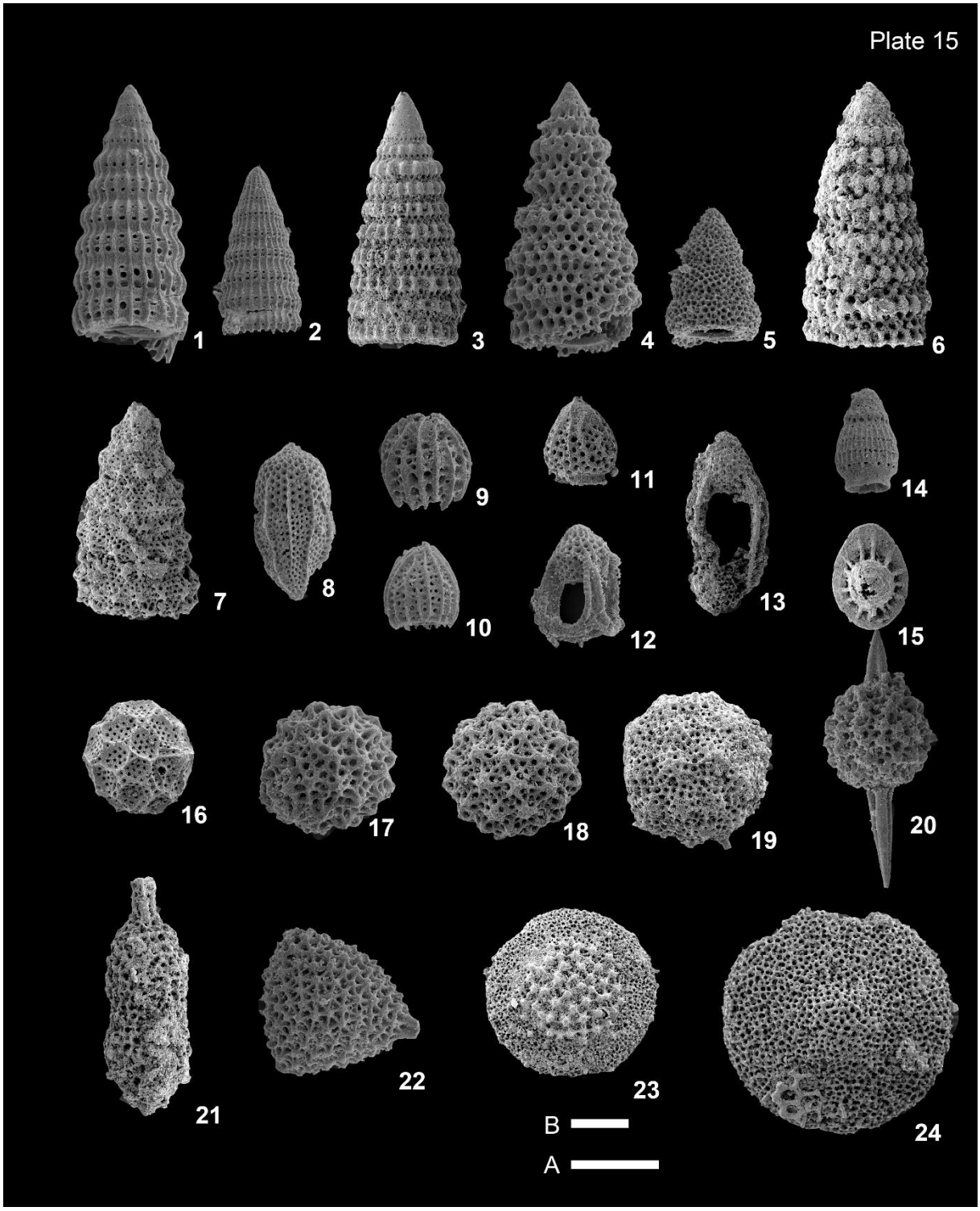
Plate 15
1
2
3
4
5
6
7
8
9
10
11
12
13
14
15
16
17
18
19
20
21
22
23
24
B
A

Explanation of Plate 16 (E-16)

Scale=100 μm
Scale A: 1-3, 5-22, 25. Scale B: 4, 23, 24

1: *Dictyomitra formosa (Squinabol)*
2: *Dictyomitra multicostata* Zittel
3: *Archaeodictyomitra* sp. A
4: *Pseudodictyomitra tiara* (Holmes)
5: *Pseudodictyomitra* sp. B
6: *Sandovalella telum* (O'Dogherty)
7, 8: *Foremanina schona* Empson-Morin
9: *Stichomitra manifesta* Foreman
10, 11: *Rhopalosyringium scissum* O'Dogherty
12: *Rhopalosyringium elegans* (Squinabol)
13, 14: *Pseudotheocampe urna* Foreman
15, 16: *Pseudotheocampe tina* Foreman
17, 18: *Annikaella omanensis* De Wever, Bourdillon-de Grissac, and Beurrier
19: *Holocryptocanium barbui* Dumitrica
20: *Hemicryptocapsa polyhedra* Dumitrica
21: *Praeconocaryomma universa* Pessagno
22: *Praeconocaryomma lipmanae* Pessagno
23: *Crucella cachensis* Pessagno
24: *Patellula euessceei* Empson-Morin
25: *Patellula verteroensis* Pessagno

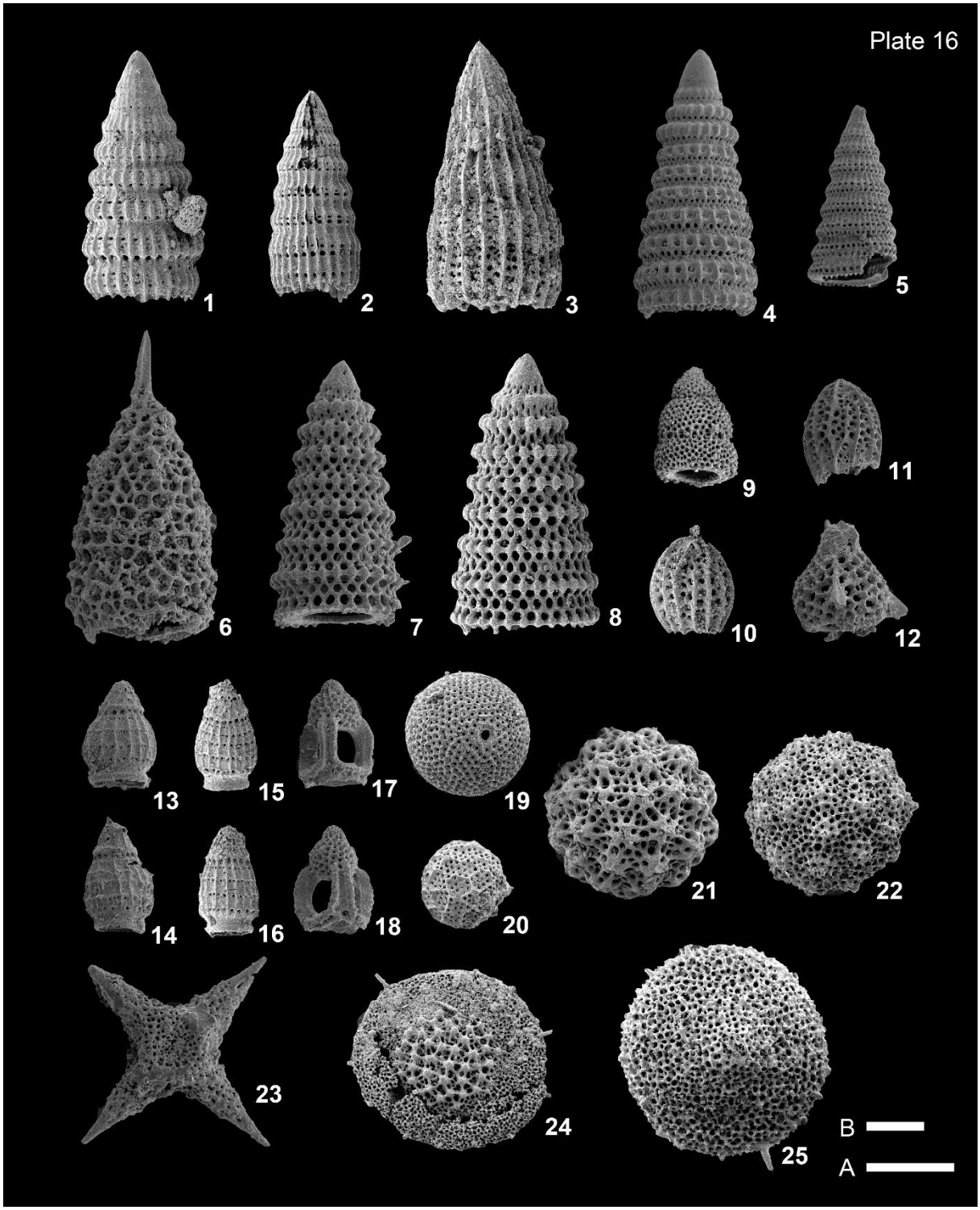
Plate 16
1
2
3
4
5
6
7
8
9
10
11
12
13
14
15
16
17
18
19
20
21
22
23
24
25
B
A

Explanation of Plate 17 (E-19)

Scale=100 µm
Scale A: 1-4, 6-22. Scale B: 5, 23, 24

1: *Dictyomitra formosa (Squinabol)*
2: *Dictyomitra multicostata* Zittel
3: *Archaeodictyomitra* sp. A
4: *Archaeodictyomitra* sp. B
5: *Pseudodictyomitra tiara* (Holmes)
6: *Sandovalella telum* (O'Dogherty)
7: *Foremanina schona* Empson-Morin
8, 9: *Rhopalosyringium scissum* O'Dogherty
10: *Rhopalosyringium adriaticum* O'Doghert
11: *Annikaella omanensis* De Wever, Bourdillon-de Grissac, and Beurrier
12, 13: *Myllocercion valgus* (De Wever, Bourdillon-de Grissac, and Beurrier)
14: *Hemicryptocapsa polyhedra* Dumitrica
15: *Hemicryptocapsa prepolyhedra* Dumitrica
16: *Pseudotheocampe urna* Foreman
17: *Diacanthocapsa* sp. A
18: *Praeconocaryomma lipmanae* Pessagno
19: *Acaeniotyle starka* Empson-Morin
20: *Archaeospongoprunum cortinaensis* Pessagno
21: *Triactoma hexeris* O'Dogherty
22: *Alievium praegallowayi* Pessgno
23: *Patellula verteroensis* Pessagno
24: *Pseudoaulophacus lenticulatus* (White)

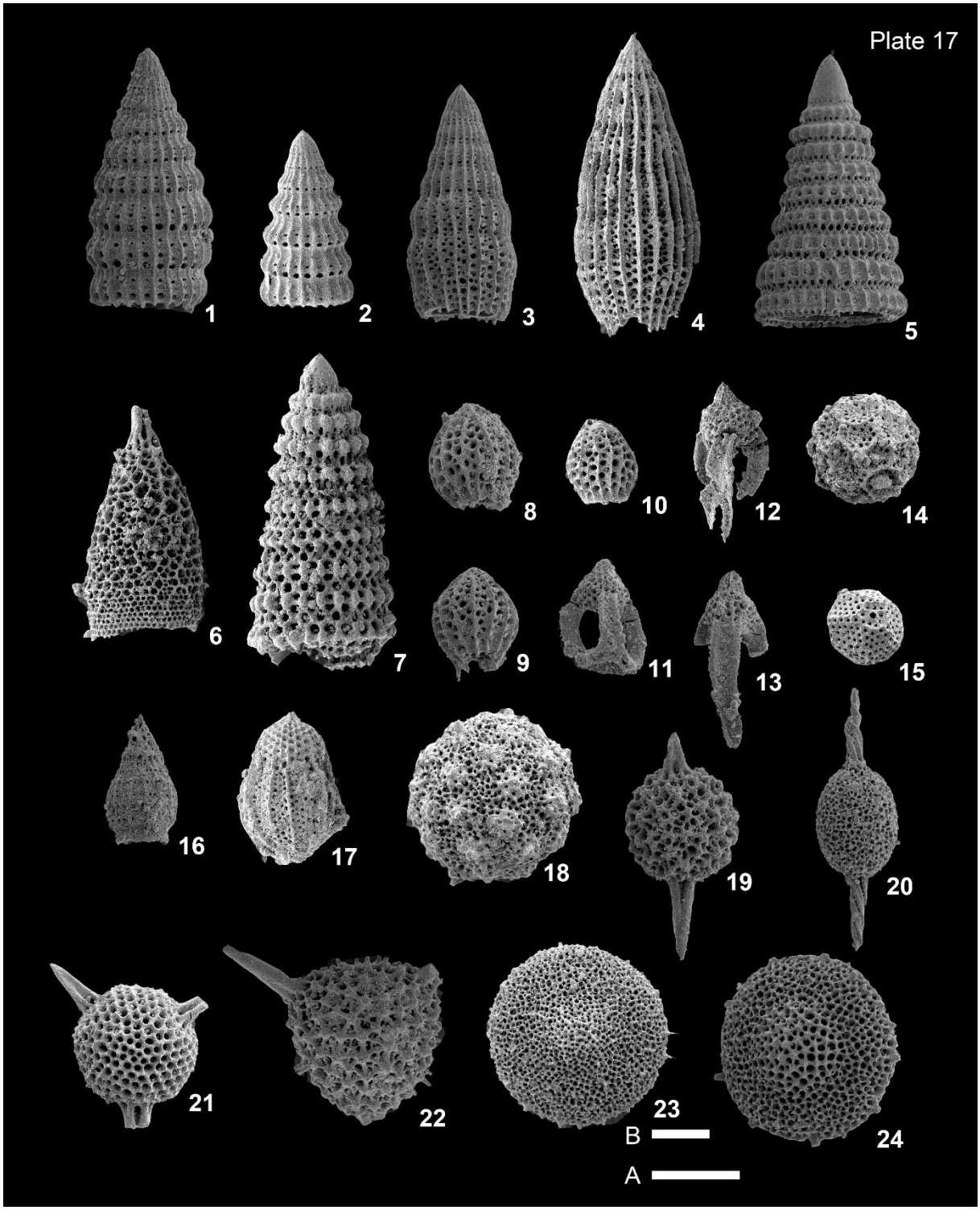
Plate 17
1
2
3
4
5
6
7
8
9
10
11
12
13
14
15
16
17
18
19
20
21
22
23
24
B
A